# Mid-Infrared Imaging of Two Circumstellar Disks: the cases of HD 179218 and Epsilon Eridani

INAUGURAL-DISSERTATION

zur

Erlangung des Doktorgrades
der Mathematisch-Naturwissenschaftlichen Fakultät
der Universität zu Köln

vorgelegt von

**Anas Salman Taha AL-Maothani**

aus Bagdad, Irak

Köln 2019

Berichterstatter:          Prof. Dr. Lucas Labadie

                           Prof. Dr. Andreas Eckart

Tag der letzten mündlichen Prüfung: Januar 2018

To Allah "Almighty"
To my father, my mother, my brothers and sisters. To my lovely and beloved wife "Shaymaa", my daughters "Qabas, Elaf", and my little son "Sadeem–(Nebula in Arabic)".

.

# Zusammenfassung

Seit Kurzem erlauben uns große erdgebundene Teleskope und die neue Generation von astronomischen Instrumenten die Umgebung von jungen Sternen mit hoher räumlicher Auflösung zu untersuchen. Detektoren im mittleren Infrarot (MIR) (7.5 - 25 Mikrometer) an Teleskopen mit Spiegeldurchmessern in der Größenordnung von 10m wurden ausgiebig genutzt, um die Eigenschaften protoplanetarer und Trümmerscheiben durch ihre vom Staub erzeugte thermische Emission zu untersuchen.

Diese Instrumente können die benötigten Auflösungen unter einer Bogensekunde mit einem ausreichenden Gesichtsfeld erreichen, um die Scheibenstrukturen auf unterschiedlichen Skalen von wenigen bis zu einigen zehn astronomischen Einheiten (AE) zu untersuchen.

Solche Beobachtungen werden benutzt, um die Entwicklung der zirkumstellaren Scheiben zu untersuchen, die Existenz von Lücken in protoplanetaren Scheiben um Herbig Sterne zu bestätigen und den evolutionären Zusammenhang zwischen flachen und sich aufgeweiteten Scheiben zu studieren. Darüber hinaus können sie uns mit mehr Details über die Geometrie der Scheibe, Staubeigenschaften und die Entstehung von Planeten versorgen. Auch können diese Beobachtungen dazu verwendet werden, die Trümmerscheiben um Hauptreihensterne zu analysieren und den Ursprung der Staubemission in Trümmerscheiben zu lokalisieren, um die Beziehung zwischen dieser Emission und Planeten zu klären.

Diese Dissertation besteht aus den folgenden zwei Teilbereichen:

**Erstes Projekt**: Das Hauptziel dieses Projektes ist es, die Eigenschaften der Polycyclic Aromatic Hydrocarbons (PAH) Emission und die physikalische Struktur der Scheibe um den Herbig Stern HD 179218 zu untersuchen. Ich habe hierzu MIR Bilder im PAH1(8.6 $\mu m$), PAH2(11.3 $\mu m$), and Si6(12.5 $\mu m$) Filter sowie niedrig aufgelöste spektroskopische Daten im N-Band von HD 179218 benutzt, die mit dem CanariCam Instrument am 10.4 m grossen Gran Telescopio Canarias (GTC) aufgenommen worden sind.

Die FWHM der Bilder wurde in jedem der drei Filter gemessen. Durch gute Beobachtungsbedingungen während der Datennahme konnten stabile Messungen mit durchschnittlichen FWHM Werten von $0.232''$, $0.280''$, und $0.93''$ in den PAH1, PAH2 beziehungsweise Si6 Filtern erhalten werden. Diese Daten zeigen, dass die Emission der Scheibe in den PAH Filtern räumlich aufgelöst ist, während sie im Si6 Filter nicht

aufgelöst werden konnte. Ich habe ein unteres Limit für den Durchmesser der Emission im Si6 Band von 100 mas (oder 40 AE) berechnet indem ich eine quadratische Subtraktion der PSF für das Objekt und den Kalibrator durchgeführt habe.

Die photometrischen Messungen sind mit bereits veröffentlichten Flussdichten auch ohne große Variabilität bei den Unsicherheiten konsistent. Darüber hinaus ist die Form des Spektrums mit niedriger Auflösung, außer in dem Bereich des Ozonbandes der Erde, vergleichbar mit den vorheriger Beobachtungen der Spitzer und ISO Weltraumteleskope.

Zusätzlich habe ich ein 3D Strahlungstransportmodell der Kontinuumsemission der protoplanetaren Scheibe mit Hilfe des Codes RADMC3D erstellt. Das Modell basiert auf einer Scheibe mit einer Lücke, um die spektrale Energieverteilung und das radiale Helligkeitsprofil von HD 179218 bei 12.5 Mikrometern zu reproduzieren. Die physikalischen Eigenschaften wie Masse, Größe und chemische Zusammensetzung der Vor-Übergangsscheibe wurden aus diesem Modell erhalten. Dies ist das erste Mal dass HD 179218 in einem PAH Filter beobachtet und räumlich aufgelöst wurde.

Schließlich diskutiere ich den Ursprung der PAH Emission in der protoplanetaren Scheibe von HD 179218, indem ich die Bilder und spektroskopischen Daten mit IRS 48 und HD 97048 vergleiche. Die wahrscheinlichste Erklärung ist, dass die PAH Emission aus einem äußeren Radius der aufgeweiteten Scheibe stammt, welches sich aufgrund der starken UV-Strahlung des Zentralsterns (180 L⊙) zumeist in einem ionisierten Zustand befindet.

**Zweites Projekt**: Der Hauptzweck dieses Projekts is die Untersuchung des warmen Staubs in der Trümmerscheibe und dem exozdiokalen Staub um den Hauptreihenstern Epsilon Erdiani.

Hochauflösende Bilder im Q-Band wurden mit dem GTC/CanariCam aufgenommen. Um die Unterscheidung zwischen Stern und Scheibe zu verstärken und Beugungslimitierte Beobachtungen zu erhalten haben wir den Q4 Filter (20.5 Mikrometer) gewählt. Die MIR Bilder von Epsilon Eridani wurden mit einem Kalibratorstern (Gamma Eridani) verglichen. Wegen schlechter Seeing Bedingungen (> 1″) ist die FWHM sehr unsicher.

Daraus folgend sind mehr als die Hälfte der FWHM Messungen des Sterns unterhalb des Beugungslimits des Teleskops im Q4 Filter. Ich habe daher verschiedene Techniken benutzt um die Qualität der Frames zu begutachten.

Die erste Technik ist der Vergleich der FWHM jedes "Savesets" des Kalibrationssterns

mit den $1\sigma$, $2\sigma$, und $3\sigma$ Leveln. Das Resultat dieser Technik ist, dass die auseinandergezogene Emission um Epsilon Erdiani eine Größe von 200 mas innerhalb einer $3\sigma$ Unsicherheit besitzt. Anschließend habe ich eine visuelle Selektionstechnik verwendet, um gute und schlechte "Nodsets" zu unterscheiden und damit die Auswahl elongierter Punktspreizfunktion (PSF) zu vermeiden. Mit dieser Technik bestätigen sich die mit den anderen Techniken erzielten Resultate: die ausgedehnte Emission der Trümmerscheibe von Epsilon Erdiani ist mit $\sim$ 180 mas mit einer Unsicherheit von $3\sigma$ berechnet. Ein Temperaturgradientenmodell wurde kreirt, um ein synthetisches Bild von Epsilon Erdiani zu erzeugen, es mit dem Kalibrationsbild zu falten und es schließlich mit dem radialen Helligkeitsprofil des wissenschaftlichen Bildes zu vergleichen.

Nach der Durchfhrung photometrischer Berechnungen erhilte ich einen Flusswert von 2.5 Jy im Q4 Filter, welcher mit Literaturwerten vergleichbar ist. Die Resultate der Beobachtungen lassen vermuten, dass die radiale Position des Staubs vergleichbar mit dem Planetenorbit ist und dass die Staubverteilung durch die Interaktion mit dem Planeten entscheidend beeinflusst wird.

# Abstract

Recently, large ground-based telescopes and the new generation of astronomical instrumentation have allowed us to examine the environments of young stellar objects with high angular resolution. Mid-infrared (MIR) (7.5 - 25 micron) detectors mounted on 10 m class telescopes have been used extensively to study the properties of protoplanetary and debris disks through their thermal emission that comes from the dust.

These instruments can achieve sub-arcsec resolution with a suitable field-of-view for investigating the disk structures on different scales from few to tens of astronomical units (AU).

Such observations are used to study the evolution of the circumstellar disk, confirm the presence of gaps in the protoplanetary disks, and investigate the evolutionary connection between flared and flat disks. Moreover, they can provide us with more details about the geometry of the disk, dust properties, and how planets form. These observations can also be used to analyze the debris disk around main sequence stars and trace the origin of the dust emission to clarify the relation between the dust emission and planets in debris disks.

There are two main projects in this dissertation:

**First project**: The main goal of this project is to investigate in the MIR the properties of the Polycyclic Aromatic Hydrocarbons (PAH) emission and the physical structure of the disk of the Herbig star HD 179218. I used MIR images in the PAH1(8.6 $\mu m$), PAH2(11.3 $\mu m$), and Si6(12.5 $\mu m$) filters, and N-band low-resolution spectra of HD 179218, using the Canari-Cam instrument on the 10.4 m Grand Telescopio Canarias (GTC).

The FWHM of the images was measured in each of the three filters. Good observing conditions led to very stable measurements during the observation with average FWHM values of 0.232″, 0.280″, and 0.293″ in filters

PAH1, PAH2, and Si6, respectively. The data show that the disk emission is spatially resolved in the both PAH filters, while unresolved in the Si6 filter. I have extracted a lower limit for the angular diameter of the emission in the PAH band of $\sim$ 100 mas, (or 40 AU) by applying a quadratic subtraction of the PSF for the science and calibrator.

The photometric measurements are consistent with published flux densities and without noticeable variability in the uncertainty. Besides that, the low-resolution spectrum result is comparable with the shape of the previous result using Spitzer and ISO space telescopes, except in the region of the Earth ozone band.

Additionally, I built a 3-D radiative transfer model of the continuum emission of the protoplanetary disk using the code RADMC3D. The model is based on a disk with a gap to fit the observational spectral energy distribution and the radial brightness profile of HD 179218 at 12.5 $\mu m$. The physical properties such as the mass, size and chemical composition of the pre-transitional disk were derived from the model. This is the first time that HD 179218 is observed in the PAH filter and is spatially resolved.

Finally, I discuss the origin of the PAH emission in the protoplanetary disk of HD 179218 by comparing the images and spectroscopic data with IRS 48 and HD 97048. The most likely explanation is that the PAH emission originates in the outer radius of the flared disk surface, and is mostly in an ionized charged state due to the strong UV radiation of the central star (180 L$\odot$).

**Second project**: The main purpose of this project is to investigate the origin of the warm dust in the debris disk and of the exozodiacal dust around the main-sequence star Epsilon Eridani.

High-resolution direct imaging in the Q-band using GTC / CanariCam instrument was performed to enhance the star-to-disk distinction and obtain diffraction limited observations, we select the Q4 filter (20.5 $\mu m$). The MIR images of Epsilon Eridani were compared with a calibration star (Gamma Eridani). Due to poor seeing condition ($> 1''$) the FWHM is very unstable.

Consequently, more than half of the FWHM measurements of the science star were less than the diffraction limit of the telescope in the Q4 filter. Therefore, I used different techniques to examine the quality of good frames.

The first technique is to compare the FWHM of each saveset of the calibration star and science star to the $1\sigma$, $2\sigma$, and $3\sigma$ levels. The result of this technique shows that the extended emission around Epsilon Eridani measures 200 mas with $3\sigma$ uncertainty. The second technique is to compare the FWHM measurements of each nodset (instead of the saveset) for the science star with a limit of $1\sigma$, which shows a resolved disk emission with a diameter of 120 mas with $3\sigma$ uncertainty. Then, I used a visual selection technique to separate the good and bad nodsets to avoid electing elongated point-spread function with this technique and other two techniques are confirmed the results of found extend emission around Epsilon Eridani. The extended emission is estimated to be $\sim 180$ mas with $3\sigma$ uncertainty. A temperature gradient model has been built to create a synthetic image of Epsilon Eridani, convolve it with the calibration image and then fit it with a radial brightness profile of the science image.

Photometric calculations were performed and I obtain a flux value comparable to literature value in the Q4 filter of $\sim 2.5$ Jy. The observational result suggests that the radial position of the dust is comparable with the planetary orbit and that the dust distribution is significantly shaped by the interaction with the planet.

# Contents

# CONTENTS

# List of Figures

# LIST OF FIGURES

# List of Tables

# Acronyms

**GMC**  Giant Molecular Clouds

**SFR**  Star Forming Regions

**HST**  Hubble Space Telescope

**ZAMS**  Zero-Age Main Sequence

**YSOs**  Young Stellar Objects

**SED**  Spectral Energy Distribution

**IR**  Infrared

**NIR**  Near-Infrared

**MIR**  Mid-Infrared

**FIR**  Far-Infrared

**CTTs**  Classical T-Tauri Stars

**WTTs**  Weak T-Tauri Stars

**PMS**  Pre-Main Sequence

**PAH**  Polycyclic Aromatic Hydrocarbons

**ISM**  Interstellar Medium

**VLT**  Very Large Telescope

**VISIR**  VLT Imager and Spectrometer for mid Infrared

## Acronyms

**STIS**  Space Telescope Imaging Spectrograph

**COMICS**  Cooled Mid-Infrared Camera and Spectrometer

**T-ReCS**  Thermal-Region Camera Spectrograph

**EKB**  Edgeworth-Kuiper Belt

**IRAS**  Infrared Astronomical Satellite

**WISE**  Wide-field Infrared Survey Explorer

**FEPS**  Formation and Evolution of Planetary Systems

**DEBRIS**  Disk Emission via a Bias Free Reconnaissance in the Infrared/Sub-millimeter

**DUNES**  DUst around NEarby Stars

**APEX**  Atacama Pathfinder Experiment

**SONS**  SCUBA-2 Observation of Nearby Stars

**JCMT**  James Clerk Maxwell Telescope

**CHARA**  Center for High Angular Resolution Astronomy

**PWV**  Precipitable Water Vapor

**GPS**  Global Positioning System

**ORM**  Observatorio del Roque de los Muchachos

**GTC**  Gran Telescope Canarias

**PSF**  Point Spread Function

**OSIRIS**  Optical System for Imaging and low-Intermediate-Resolution Integrated Spectroscopy

**CIRCE**  Canarias InfraRed Camera Experiment

**EMIR**  Especrografo Multiobjecto Infra-Rojo

**IBC**  Impurity Band Conduction

**BIB**  Blocked Impurity Band

**FPA**  Focal Plan Array

**FWHM**  Full Width Half Maximum

**HWP**  half-wave plate

**FITS**  Flexible Image Transport System

**IDL**  Interactive Data Language

**HR**  Hertzsprung-Russell

**ISO**  Infrared Space Observatory

**MIPS**  Multi-Band Imaging Photometer for Spitzer

**SCUBA**  Submillimeter Common-User Bolometer Array

**VLTI**  Very Large Telescope Interferometer

**DIMM**  Differential Image Motion Monitor

**MATISSE**  Multi AperTure mid-Infrared SpectroScopic Experiment

**ALMA**  Atacama Large Millimeter Array

**ELT**  Extremely Large Telescope

**TMT**  Thirty Meter Telescope

**JWST**  James Webb Space Telescope

**SPICA**  Space Infrared Telescope for Cosmology and Astrophysics

**LBT**  Large Binocular Telescope

# Acronyms

# 1

# Motivations and structure of the thesis

At the time of writing, more than 3000 confirmed exoplanets[1] have been detected around stars using a variety of direct and indirect methods such as the radial velocities technique, planetary transits or direct imaging. The interested reader may refer to the thorough review of Wright and Gaudi (2013) for an overview of such techniques. Every year, the number of detected planetary companions is increased due to the refinement and improved accuracy of these techniques, which allows astronomers to reach more robustly the range of Earth-mass planets: a spectacular result has been obtained in this direction by Anglada-Escudé *et al.* (2016) with the detection of Proxima b  a possibly terrestrial planet in a temperate orbit around the nearby red dwarf Proxima Centauri located at 1.3 pc.

Interestingly, the relatively large sample available to date points out a strong diversity in the exoplanetary systems in terms of size, mass, density, separation, composition (Rauer, 2013) and questions in a profound way the supposed unicity of our Solar System as a standard model. Since the first detection of 51-Peg-b by Mayor and Queloz (1995) more than twenty years ago, the field of exoplanets has now become a new and vigorous area of research in modern astrophysics. New questions arise on the statistically relevant physical and chemical properties of these new worlds. On the long-term, the spectroscopic characterization at optical and infrared wavelengths of planetary companions remains a major goal for the next decade (Madhusudhan *et al.*, 2014).

---

[1]www.exoplanet.eu/catalog/

# 1. MOTIVATIONS AND STRUCTURE OF THE THESIS

Considering the diversity of the aforementioned population of exoplanets, an important question regards their mechanism of formation and evolution across the stellar lifetime. The current models of planet and star formation suggest that a better understanding of these processes require to focus on the *circumstellar disk* around pre-main sequence and main-sequence stars, which the focus of this thesis. Circumstellar disks produce a noticeable infrared excess, which is seen in the spectral energy distribution of the object (see Chapter 2). However, the morphological complexity of the spatial structure of the disk can be ideally traced employing high-angular resolution techniques that make use of large telescopes and interferometer Absil and Mawet (2010). In many cases, an estimate of the characteristic size of the disk allows to derive the circumstellar region where the bulk of the infrared excess emission is concentrated. In this thesis, I have used spatially resolved mid-infrared imaging for this purpose. The objective of this thesis is to study with Mid-Infrared (MIR) direct imaging the circumstellar disk around stars at two different evolutionary stages, namely in the *pre-main sequence phase* and in the *main-sequence phase*. The thesis is organized as follows:

In chapter 2, I introduce the context of star and planet formation and the observational diagnostic tracers that can be investigated in the study of circumstellar material. In chapter 3, It inculdes the information about the atmosphere transparency, water vapour and emissivity for the {MIR observation. Then I have explained What is the diffraction limit and the relation between the diffraction and the seeing?. The GTC telescope properties, CanariCam instrument details, How the observation and data reduction works? all those subjects are aslo descibed in the chapter 3. In chapter 4, I present in detail the science case of HD 179218, a A-type pre-main sequence object, the emission of which I investigated in the Polycyclic Aromatic Hydrocarbons (PAH) bands in the MIR spectral range, between 8 and 13 microns. I focus on determining the spatial extent of the disk emission in the PAH bands and in the continuum, and attempt to correlate it with the charge state of the PAH molecules as derived from the spectrum of the object.

In chapter 5, I concentrate on the challenging case of the direct imaging of the debris disk around Epsilon Eridani, one of the famous object exhibiting the Vega phenomenon and hosting at the same time a possible Jupiter-like planet Hatzes *et al.* (2000). The flux contrast between the central star and the fainter exozodiacal emission makes the observation difficult from the ground, although not impossible if sufficient collecting area is used. The conclusions and the prospects are presented in chapter 6.

# 2

# Introduction and Background

## 2.1    Introduction to Star Formation

Circumstellar disks are a well-known byproduct of star formation. I shortly review hereafter some important aspects of the field. Star formation takes place in molecular clouds. These are very dense regions of gas and dust where stars form through accretion processes.

The nearest molecular clouds to our solar system are *Orion, Ophiuchus, Taurus-Auriga, Chamaeleon, and Serpens*. Those molecular clouds have been studied for extensively as they are known to be rich and nearby forming region star, and therefore ideal laboratories for observational studies. Hydrogen is the most abundant element in a molecular cloud (75%). Helium is the second most abundant element with an abundance of (25%), which is then followed by fewer heavier elements such as carbon, nitrogen, oxygen, calcium, and sodium (Seeds and Backman, 2011). Molecular clouds are classified according to different constituting properties:

1. **Diffuse Molecular Clouds** or (**Translucent Molecular Cloud**): Diffuse molecular clouds are low dense clouds with number densities ranging from $5\times10^8$ - $5\times10^9$ m$^{-3}$, with temperature of 50 K and masses up to 50 M$_\odot$. A good example of such a diffuse molecular cloud is *Ophiuchus*. It lies at a distance of approximately 140 pc from our solar system with a size of about 6 pc in diameter and a mass of circa $10^4$ M$_\odot$. Star formation rates in such clouds are relatively low, which mainly results the in formation of low-mass stars.

## 2. INTRODUCTION AND BACKGROUND

2. **Giant Molecular Clouds (GMC):** These are more dense clouds and exhibit a rich variety of dust and gas. They have number densities in the range of $1 \times 10^8 - 3 \times 10^8$ m$^{-3}$ and temperature of approximately 15 K. The size of the cloud is in the range of 50 pc in diameter and masses of the clouds are between $10^5$ and $10^6$ M$_\odot$. *Orion* is one of the most interesting giant molecular cloud. It lies at a distance of 400 pc with a diamtere of nearly 60 pc. The mass of the cloud is about $10^6$ M$_\odot$. It contains massive O-type stars at its center which affects the nearly low mass star formation, as illustrated in Figure 2.1.

3. **Dark Clouds:** Dark clouds exhibit very high densities. They are divided into two types: complex and individual clouds. Complex clouds have a density of $5 \times 10^8$ m$^{-3}$ and a temperature of around 10 K. The size of complex clouds is about 10 pc in diameter with a mass of $10^4$ M$_\odot$. *Taurus-Auriga* belongs to the complexes dark cloud at a distance of 140 pc. Individual dark clouds are denser and smaller than complex dark cloud with densities around $10^9$ m$^{-3}$ and with typical sizes of about 2 pc in diameter. The temperature of the cloud is about 10 K with a mass of circa 50 M$_\odot$. The B1 cloud is an example for such an individual dark cloud.

4. **Dense Core Clouds:** Dense core clouds are small clouds in the galaxy with diameter 0.1 pc. The mass of such clouds is 10 M$_\odot$ with a temperature of about 10 K. They have densities of circa $10^{10}$ m$^{-3}$ as found in the archetypical object *TMC-1/B335* (Stahler and Palla, 2008).

5. **Hot Core Clouds:** Hot core clouds are the smallest clouds in the galaxy with diameter in the range of 0.05 - 0.1 pc. They are denser than other molecular clouds with densities between $10^{13}$ - $10^{15}$ m$^{-3}$ and also exhibit higher temperatures and larger masses in comparison to other two molecular clouds (Drak clouds and Dense clouds) (T ~ 100 - 300 K, M ~ 10 - 3000 M$_\odot$).

6. **Bok Globules Cloud**: The center of the cloud is the place for low mass stars formation and hosts a very dense core. Bok globules have a roughly spherical shape and a temperature of circa 10 K. The density of such a cloud is larger than $10^{10}$ m$^{-3}$ and its size is smaller than 1 pc in diameter. The mass of bok globules is in the range of 1 - 1000 M$_\odot$. A well-known Bok Globule is *Barnard 68*. The regions in molecular clouds where the conditions are suitable to form stars are called *Star Forming Regions (SFR)* (Carroll and Ostlie, 2007; Stahler and Palla, 2008).

**Figure 2.1:** Orion nebula was captured by Hubble Space Telescope HST in 2009. As noticed from the image, Orion consists of gas and dust, many of stars born surrounded by materials. Image credit: NASA, ESA, M. Robberto (Space Telescope Science Institute/ESA), the Hubble Space Telescope Orion Treasury Project Team and L. Ricci (ESO)"
https://www.spacetelescope.org/images/heic0917ab/.

The collapse of the molecular cloud is initiated when the mass of the cloud exceeds the Jeans criterion, or Jean's mass. This criterion was proposed by *Sir James Jeans* in 1902. When the gravitational pull overtakes the radiative gas pressure, then the molecular cloud starts to collapse inwardly. The Jeans mass is calculated following Carroll and Ostlie (2007) according to:

$$M_J \simeq \left(\frac{5kT}{G\mu m_H}\right)^{3/2} \left(\frac{3}{4\pi\rho_0}\right)^{1/2} \tag{2.1}$$

where $k$ is the *Boltzmann's Constant* ($k = 1.38 \times 10^{-8}$ J k$^{-1}$), $T$ is the temperature of the cloud and $G$ is the *Gravitational Constant* ($G = 6.674 \times 10^{-11}$ m$^3$ kg$^{-1}$ s$^{-2}$), $\mu$ is the mean molecular weight, $m_H$ is the mass of the hydrogen atom ($m_H = 1.6735 \times 10^{-27}$ kg), $\rho$ is the density of the cloud in unit (kg/m$^3$).

There are two scenarios of collapse in a giant molecular cloud. The homologous collapse is a scenario where the uniform density across the molecular cloud makes the different regions of the cloud to collapse in about the same amount of time. The

## 2. INTRODUCTION AND BACKGROUND

inside-out collapse describes a scenario where, if the cloud center is denser than the outer regions, the time of collapse in the center will be shorter.

That means the material which is close to the center will require a shorter time to collapse than the material which is far from the center. The time of cloud collapse is called *Free-Fall* time-scale and can be determined by (Carroll and Ostlie, 2007):

$$t_{ff} = \left( \frac{3\pi}{32 G \rho_0} \right)^{1/2} \tag{2.2}$$

For example, let's assume the density of the cloud was ($\rho_0 = 3 \times 10^{-17}$ kg $m^{-3}$) then the free fall time is ($t_{ff} = 3.8 \times 10^5$) yr.

The consequence of the collapse of the molecular cloud is to increase the density during the free fall. The Jeans mass decreases, whereas the temperature of the cloud is not changing throughout the collapse. This means the cloud collapse is isothermal. After that, any inhomogeneities in the density of the cloud will be the reason for producing smaller features of clouds from the large cloud. This sequences of the collapse is called *fragmentation* and tends to form group of stars.

This fragmentation can not be continuous until infinity, it will stop at a specific point. What does make this fragmentation process to stop? It depends on the assumption that the collapse of the cloud is isothermal. The gravitational collapse produces energy increase of the optical depth and this energy is sustained in the cloud, then the temperature must increase. This increase in temperature will convert the state of collapse cloud from isothermal to adiabatic (relation between temperature and density). Eventually, the core of the cloud becomes quasi-static equilibrium.

The inner dense core in the center of the collapsed cloud is called protostar. The cloud has non-zero angular momentum, hence any initial rotation of the cloud will cause the in-falling material to build up a disc around the protostar.

The phase when the nuclear reactions start inside the core of the star is known as *Zero-Age Main Sequence (ZAMS)* star phase. The time scale for this duration called *Kelvin-Helmholtz* time scale and can be estimated through this formula (Bodenheimer, 2011):

$$t_{kh} \approx \frac{GM^2}{RL} \tag{2.3}$$

where $R$ is the radius of the protostar and $L$ is the average luminosity. The time scale ($t_{kh}$) for one solar masses is ($\approx 4 \times 10^7$ yr).
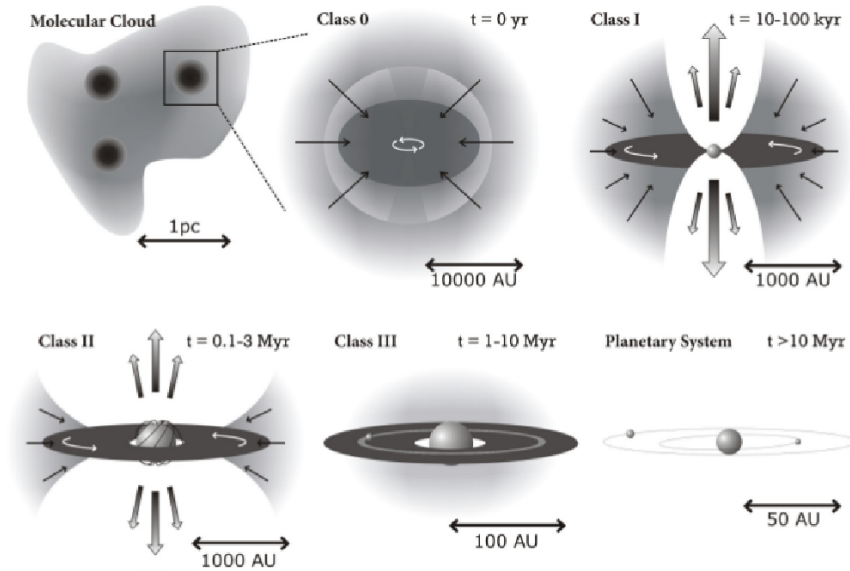
**Figure 2.2:** Diagram of star formation process through time. It starts from the molecular cloud collapse in the center which is represented by Class 0. As a result of this collapse, the protostar form in the center of the collapse and surrounded by massive protoplanetary disk Class I. Protoplantery disk begins to dissipate material by forming planets Class II. After that, all the material which has been dissipated will form solar system with planets in Class III (Ward-Thompson and Whitworth, 2011).

*Young Stellar Objects (YSOs)* in the pre-main sequence phase are classified into four classes by Lada (1987) and modified by Andre *et al.* (1993) who added the Class 0 to the classification. This classification based on the Spectral Energy Distribution (SED) shape. SEDs were found to have different shapes classification association with YSOs evolution. The origin of SED emission of the YSOs comes from two components. The first component is the protostar which emits as a black body radiation in the SED and the second component is the thermal emission comes mainly from the dust in the protoplanetary disk. For more clarification, the material closest to the protostar can be emitted in the Near-Infrared (NIR) wavelengths range (0.7 $\mu m$ - 5 $\mu m$), material a little farther would emit in the MIR wavelengths range between (5 $\mu m$ - 20 $\mu m$) and for material more farther distance from the protostar are colder and emit in the Far-Infrared (FIR) wavelengths range (20 $\mu m$ - 1 mm), sub-millimetre wavelengths.

## 2. INTRODUCTION AND BACKGROUND

The classifications can be extracted from the slope of the SED by using this formula (Stahler and Palla, 2008):

$$\alpha \approx \frac{dlog(\lambda F_\lambda)}{dlog\lambda} \tag{2.4}$$

Where $\lambda$ is the wavelength and $F_\lambda$ is the observed flux.

**Class 0:** It represents the earlier stage of young stellar objects formation. It was not found in the first classification from Lada (1987), but it was added later by Andre *et al.* (1993). In this class, protostar forming is embedded by accreting an envelope and has a very strong emission in the sub-millimetre wavelength and it is not visible in the optical. Some objects can be observed in the MIR and FIR.

**Class I** ($\alpha > 0$)**:** When the value of the slope is positive. Young stellar objects are forming a star with very strong outflows or called (bipolar jets) and surrounded by the potoplanetary disk. The envelope in this stage starts to dissipate and a star becomes partially observed in the optical. The SED has a rising in the MIR emission which mostly comes from the protoplanetary disk.

**Class II** ($-1.5 < \alpha < 0$)**:** The star in this class is called Pre-Main sequence star. Where most of the materials in the envelope have been dissipated and the star becomes observed completely in the optical wavelength. The SED of Class II has combined emission from the star and the disk has a very less strong Infrared (IR)-emission from Class 0 and I. This emission comes from the dust and the gas in the protoplanetary disk. The protostars in this class can be divided into three types according to their masses. Pre-Main-Sequence stars with masses less than 2 $M_\odot$ are called Low Mass Stars. Low Mass Stars are classified to Classical T-Tauri Stars (CTTs) and Weak T-Tauri Stars (WTTs) which has weaker IR emission than CTTs. The protostar has mass larger than 2 $M_\odot$ or in the range (2 $M_\odot$ - 8 $M_\odot$) known as Intermediate Mass Stars "*Herbig Ae/Be stars*", as shown in Figure 2.3.

*Massive stars* protostars which have masses greater than (8 $M_\odot$ - 10 $M_\odot$) are called "Massive stars". The massive stars can not be observed during Class II because they are evolved much quicker than low mass stars.

**Class III** ($\alpha < 0$)**:** The young stellar object reaches to the stage of the main sequence stars and the disk around the star is called "Debris Disk". The SED of the Class III stage has less IR emission and the debris disk is optically thin. The reason behind the IR emission of the SED in Class III is less than Class II due to use of all dust and gas in the protoplanetary disk to form planets. This small IR emission originates

from the collision of the giant planets with residual small grains, comets, planetesimals Williams and Cieza (2011). The sketch below show the young stellar object evolution through four Classes with time.
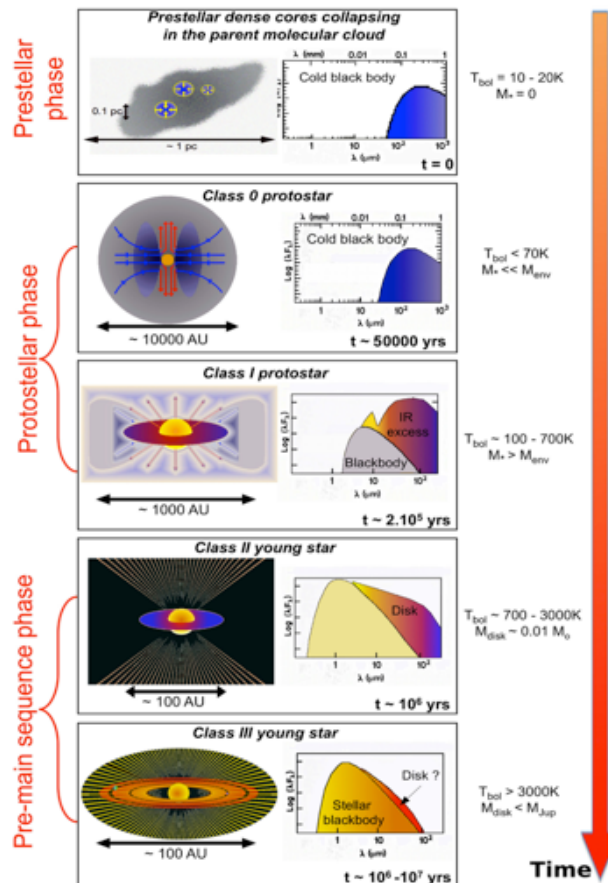


**Figure 2.3:** Scheme to show Infrared emission in spectral energy distribution changes with young stellar objects evolution http://irfu.cea.fr/Pisp/anaelle.maury/Research.html.

This classification can be fitted for most of young stellar objects. But, not necessary all of them. There are different factors that works on the shape of the SED as the dust grains size and edge-on protoplanetary disk. In this thesis, I have studied both cases protoplanetary disk where the Exo-planet form then the debris disk where the Exoplanet spends the rest of the time after being formed.

## 2.2   Protoplanetary Disk

Protoplanetary disks are large reservoirs of dust and gas. There are evidenced to be the birthplace of exoplanets, which form out of the disk material. This primordial disk, which is a byproduct of star formation, is typically detected in the Class II phase, more rarely in the Class I phase (see Figure 2.3).

For low- and intermediate-mass pre-main sequence stars, this is in part due to the fact that the object spends a longer lifetime ($10^6 - 10^7$ yr) in the Class II phase than in the Class I phase ($10^5$ yr).

Protoplanetary disks are observed around Pre-Main Sequence (PMS) stars, before the ignition of the nuclear reactions in the stellar core. Based on their mass, PMS stars are classified as T-Tauri stars ($< 2$ M$_\odot$) and Herbig stars (between 2 and 10 M$_\odot$). Disks have also been observed around brown-dwarfs (Riaz *et al.*, 2009) and even around planetary-mass objects (Zapatero Osorio *et al.*, 2007).

While the model of formation of high-mass stars theorized the low-probability of disk survival around stars more massive than 10 M$_\odot$ on time scales longer than $10^5$ years, observational evidence of this transient phase was revealed by high-angular resolution observations (Chini *et al.*, 2004; Kraus *et al.*, 2010).

The highly complex structure of a protoplanetary disk results from different physical properties in different regions of the disk. One of the first and powerful method to study pre-main sequence objects is through the analysis of the SED, as illustrated in Figure 2.3. Global properties of the disk, such as for instance the level of infrared to millimeter excess, can be derived from the SED of the disk. But this method may lead also to degenerated results as in the case of binary stars, where a low-mass cool companion may mimic the blackbody-like spectrum of the circumstellar disk (Dutrey *et al.*, 2004).

Protoplanetary disks are mostly formed of molecular hydrogen gas (circa 99 % of the disk's mass) and of dust particles (circa 1 % of the disk's mass). The dust contributes significantly to the overall emission budget. On a first approximation, dust grains behave as black body emitters and therefore have a temperature-dependent emission peak. However, actual grains have a wavelength-dependent emissivity and can be better described by a modified blackbody. A good approximation of the grain emissivity is that $\epsilon \sim a / \lambda$, where $a$ is the grain radius. This means that small grains are poor radiators at long wavelengths, which influences the overall SED shape.

Sub-millimeter observations of the dust will essentially probe the larger mm-size grains. Finally, dust emission will depend on the opacity law of the grains, which is determined by the intrinsic physico-chemical properties of the matter.

Considering the dependence of the grains emission with temperature, different observing wavelengths will probe different regions of the disk: at optical / NIR wavelengths, the observer mainly senses the stellar light scattered by dust grains at the surface of the disk; in the range of distances (0.1 AU - 1 AU) from the star, warm dust continuum can be better studied at NIR wavelengths; longer MIR wavelengths are ideal to explore the 10 AU regions of protoplanetary disks where dust has a temperature of ~300 K; moving towards lower temperatures at larger distances (~100 AU from the central star), FIR and millimeter emission originates from colder (~50 K) and larger (mm- to cm-size) grains in the outer regions of the protoplanetary disk, as shown in Figure 2.4.
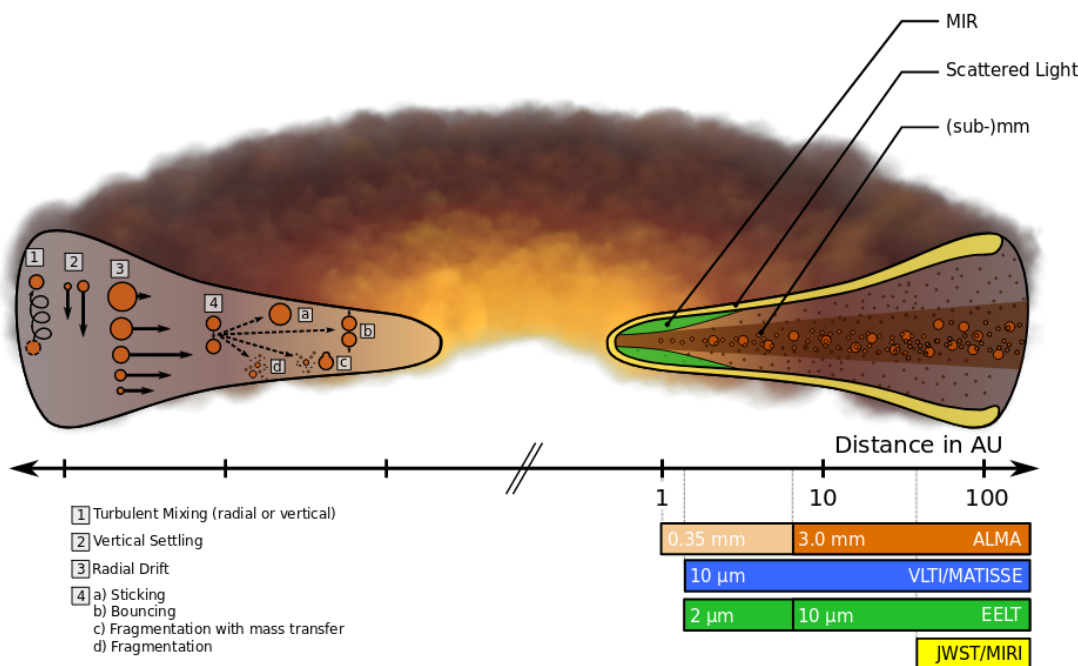


**Figure 2.4:** This scheme illustrates the protoplanetary disk structure, dust grain evolution and observation. The right side shows which observation technique is suitable with different parts of the disk. The left side shows different mechanisms of dust grain with different positions in the disk (Testi *et al.*, 2014).

## 2. INTRODUCTION AND BACKGROUND

Noteworthy, if the gas in the disk is in Keplerian rotation (e.g. in the case of HD 34282, Piétu *et al.* (2003)), the collision velocity increases from the outer to the inner regions, therefore the dynamical timescale is shorter for the inner disk in comparison to the outer disk (Williams and Cieza, 2011). Two types of model are typically foreseen for protoplanetary disks: the passively irradiated disk (Dullemond *et al.*, 2001) absorbs the stellar photons of the central star and re-emits the light at infrared wavelengths, depending on the opacity of the disk's dust. On the other hand, active accretion disks produce a significant fraction of their emission budget via viscous dissipation (i.e. friction between the gas molecules of the disk).

Most spectral energy distributions in Herbig stars exhibit a NIR "emission bump" in the (2 *μm* to 4 *μm*) region, which has been initially difficult to model (Natta *et al.*, 2001). This emission is proposed to originate close to the dust sublimation radius, where dust grains are being sublimated at around 1500 K. In Dullemond *et al.* (2001), the authors suggest a "puffed-up" structure of the inner disk with a locally increased vertical scale height. This results into a larger vertical surface being directly irradiated by the central star, hence producing higher flux in (2 *μm* - 3 *μm*) peak region of a 1500 K blackbody. The puffed-up structure, when optically thick, may also induce shadowing of the disk region immediately behind it.

Different mechanisms can be invoked to explain the dispersal of the circumstellar material in protoplanetary disks (Armitage, 2010): photo-evaporation results, for instance, onto the formation of a gap that separates the inner and outer disk regions. The direct irradiation of the gas by UV photons results in an increase of the gas temperature, and consequently in an increase of the thermal velocity ($v_{th}$) of the gas ($v_{th} \propto \sqrt{T}$). At the radius $r_g$ where the thermal velocity of the gas is larger than its Keplerian velocity, the gas becomes unbounded and is expelled in the form of a wind. The formation of planets is a second scenario classically invoked to explain the disk dispersal. Rapid grain growth and gas accretion onto the forming planetesimals can disperse the disk in few Myr. This timescale also depends on different factors such as the stellar mass and the grain opacity (Mason, 2008).

In multiple systems where the dynamical influence of the companion can be strong, the disk can be further truncated and sees its lifetime typically reduced with respect to the single star system (McCabe *et al.*, 2006). Disk evolution in multiple systems is still poorly understood (Duchêne and Kraus, 2013), despite rapid progress on the side of hydrodynamical simulations (Thebault and Haghighipour, 2014).

A first classification of intermediate-mass Herbig stars was proposed by Waelkens *et al.* (1994) and collaborators in 1994 based on the shape of the spectral energy distribution of the system. The classification is based on the observation of a double-peaked versus single-peaked SED as shown in Figure 2.5. This was interpreted as the presence of a large dust gap in the disk possibly resulting from the process of planet formation.
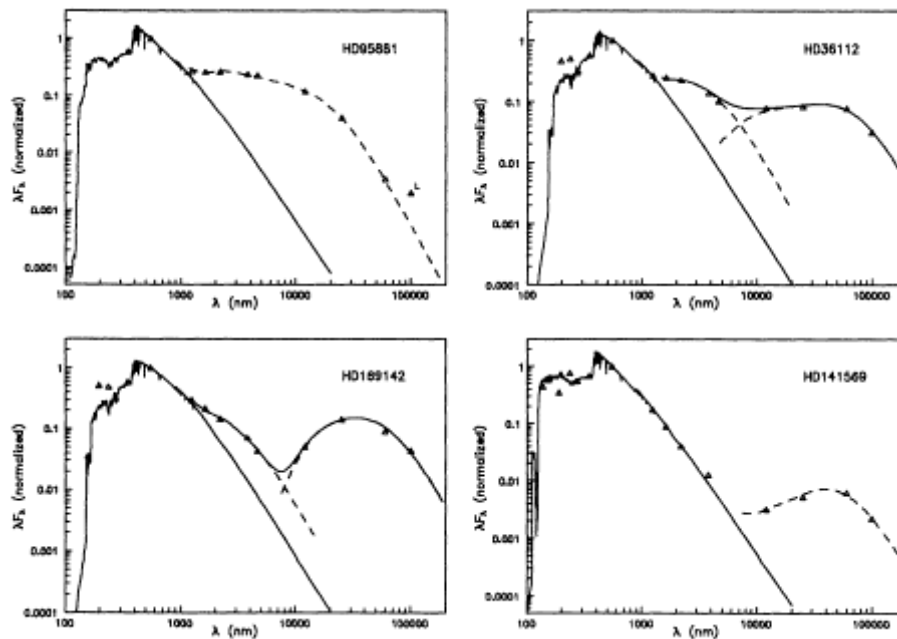


**Figure 2.5:** Four spectral energy distribution of the Herbig stars with Infrared emission which extracted from IRAS data (Waelkens *et al.*, 1994).

In Meeus *et al.* (2001), the authors proposed a more sophisticated classification among Herbig's disks. Still based on the analysis of the SED, the classification makes essentially the difference between flared and flat geometries. Meeus *et al.* (2001) identifies two populations of so-called Group I and Group II disks. In Group I disks, the MIR excess is prominent and can be modeled by a blackbody function. In Group II source the MIR excess is flatter and can only be modeled with a power-law function. The classification interprets Group I disks as flared structure capable of intercepting a wider fraction of the flux coming from the central star. In thermodynamic equilibrium, a larger surface of the disk re-emits the absorbed radiation at mid- and far-infrared wavelengths. At the contrary, Group II disks are essentially geometrically flat – with a flaring index equal to zero – resulting in partial of total self-shadowing of the disk.

## 2. INTRODUCTION AND BACKGROUND

A scenario proposed by Dullemond and Dominik (2004a) to explain the differences between Groups I and II is the phenomenon of grain growth: during the disk's lifetime, sub-micrometer dust grains coagulate in larger and heavier particles that will tend to settle towards the midplane under the effect of gravitation. Larger grains also have a smaller emissivity at infrared wavelengths than at sub-millimeter wavelengths. Being inefficient emitters in the $10\,\mu m$ range, the disk brightness is reduced in this wavelength range. In this scenario Group I protoplanetary disks are therefore the progenitors of Group II disks.

Concluding that most Group I disks are gapped disks, Maaskant *et al.* (2013) later suggested that Group I (gapped) disks and Group II disks represent two distinct rather than subsequent evolutionary stages from a common flared primordial disk. However, establishing a firm evolutionary connection between the different disks groups still remains speculative: in the light of recent interferometric results, Menu *et al.* (2015) actually proposes the hypothesis that Group II disks evolve in Group I disks with flared geometries.

An important feature observed in circumstellar disks is the presence of PAHs. They are considered to be very tiny dust grains or large molecular and can be detected in the spectrum of many astronomical objects: they are found in the Interstellar Medium (ISM), HII regions, reflection nebulae, young stellar objects, cometary material, protoplanetary disk, planetary nebulae and nuclei of galaxies. The PAHs can be easily ionized by a UV radiation field and are suggested to largely contribute to the heating of the disks gas - hence influencing the structure of the disk itself - via the photoelectric heating (Habart *et al.*, 2001; Weingartner and Draine, 2001).

A small size of the PAHs molecular is making them able to widespread in the protoplanetary disk and escape from the settling as the dust grains in the mid-plane. Therefore, PAH emission can be a good sign for the relation between the strength of the stellar radiation and the size of the PAH. According to some studies, the analysis of the MIR emission for 12 sources using Spitzer space telescope has proved that there is a relation between the size of the PAH and strength of the stellar radiation stronger emission. The very small PAHs is survived when the radiation from the stellar radiation is strong (Berné *et al.*, 2009; Visser *et al.*, 2007).

In the last few years, Lagage *et al.* (2006) and Doucet *et al.* (2006) imaging of the HD 97048 using Very Large Telescope (VLT) telescope / VLT Imager and Spectrometer for mid Infrared (VISIR) in the PAH filter. They found that the PAH emission comes from the surface of the outer disk. This result supports the idea that the PAH is being gas more than being dust grains. The left Figure 2.6 shows the PAH emission from the surface of the HD 97048 and right Figure 2.6 shows two IR spectrums of the PAH emission from two different positions in the Iris nebula.
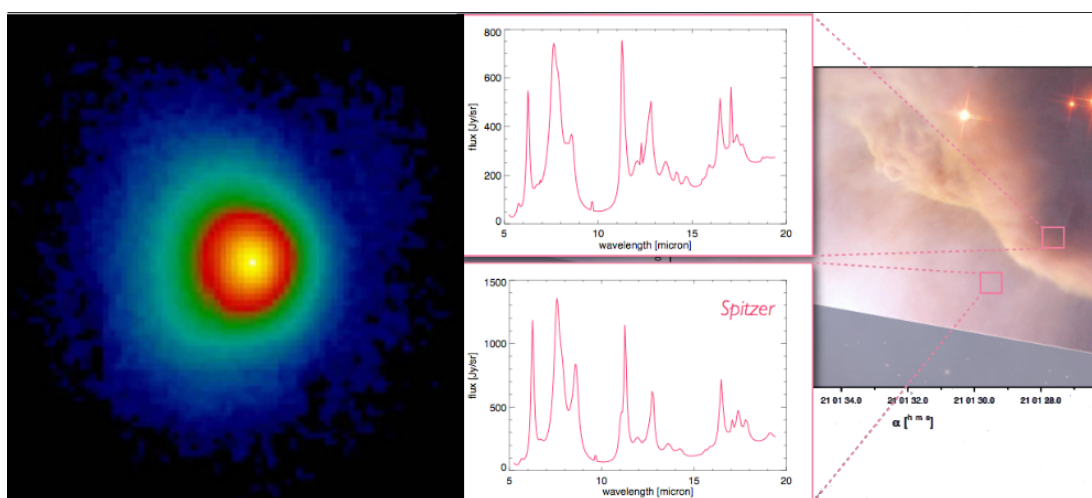


**Figure 2.6:** Left-figure: Image of HD 97048 in the PAH filter using VLT / VISIR and shows the PAH surface emission in the MIR wavelength (Lagage *et al.*, 2006). Right-figure: IR spectrum of the PAH molecular from a different position in the Iris nebula (Laboratory, 8 24)

(Geers *et al.*, 2007) observed one of the Herbig stars which is IRS 48 (A dwarf) in different wavelength 8.6, 9, 11.3, 11.9 and 18.7 $\mu m$ filters. The image of the protoplanetary disk around IRS 48 shows a gap with the size of 30 AU in the 18.7 $\mu m$ filter. So, this object could be observed in the phase of the transitional disk. Another example for tracing PAH in the protoplanetary disk are 14 Herbig stars that are observed using Space Telescope Imaging Spectrograph (STIS) coronagraphic imaging by Grady *et al.* (2005). They found that the visibility of the object is related to the strength of PAH emission at 6.2 $\mu m$ and those small grains have to be photoed.

Most recently, Maaskant *et al.* (2013) has traced the PAH and silicate emission in the surface of the four of Herbig stars Group Ib HD 79048, HD 169142, HD 135344B, and IRS 48 by using Subaru / Cooled Mid-Infrared Camera and Spectrometer (COMICS),

## 2. INTRODUCTION AND BACKGROUND

Gemini South / Thermal-Region Camera Spectrograph (T-ReCS) and VLT / VISIR telescopes at N and Q bands to compare the observations with radiative transfer model and to get more details a bout the geometry of disks. From the continuum emission and Polycyclic Aromatic Hydrocarbons Emission had managed to know the geometry of the disk. When emission from the PAH dominate in the protoplantery disk than the silicate, that means the emission comes from the surface of the outer disk. On the other hand, when the PAH emission comes from the inner region of disk, means the PAH emission is equal or less than silicate emission.

Other studies have been done by Maaskant *et al.* (2014) for the same targets by tracing the PAH ionization in the disk to tell more about the size of the gap. The base of this study is to measure the maximum of the ratio ($I_{6.2}$ / $I_{11.3}$) for PAHs features. Where the neutral PAHs has stronger emission in the 11.3 *μm* and ionized PAHs has less emission. While the inverse situation at 6.2 *μm*, ionized PAHs has stronger emission than the neutral emission. The neutral PAH emission comes from the region of the disk where it is optically thick, electron density higher and UV radiation is low. The ionization PAH emission originates from the region in the disk where it is optically thin, electron density is low and UV radiation is high. In chapter (4), there are more details and a practical case about how the PAH emission can be used to obtain the physical properties and to describe of the protoplanetary disk around HD 179218.

## 2.3   Debris Disk

Debris disks correspond to an evolutionary phase of the circumstellar material that follows the gas-rich protoplanetary disk, during which the quasi-entirety of the primordial dust and gas is being accreted in a few million years into the star and into the forming planets - at least in the core accretion model of planet formation (Hayashi *et al.*, 1985), (Pollack *et al.*, 1996)- or being photo-evaporated. At the end of this phase, main sequence stars older than few tens of millions year may lost such gas-poor "remnant" disks. Debris disks dust is also present in our own Solar System, which influence is observed through the phenomenon of the Zodiacal light.

It is established that debris disks consist of second-generation, i.e. not primordial, dust that does not come from the protoplanetary-disk phase (Lagrange *et al.*, 2000). This can be explained by the fact that the lifetime for the dust grains to be removed via radiation pressure and Poynting-Robertson drag is much shorter than the age of the system (Dutrey *et al.*, 2004). Therefore, exozodiacal dust must then be regenerated in-situ by mechanisms such as collisions between planetesimals or cometary activity. These second generation "debris" disks result in a modest but detectable infrared excess, which level declines with increasing age of the system (Rieke *et al.*, 2005).

Most main sequence stars are found to be surrounded by those debris disks. Two noticeable debris disk components in our solar system are the asteroid belt in the terrestrial planet region between 2 AU and 3.5 AU, and the Edgeworth-Kuiper Belt (EKB) which contains the coldest dust at distances larger than 30 AU from the Sun (Matthews *et al.*, 2014), as shown in Figure 2.7.
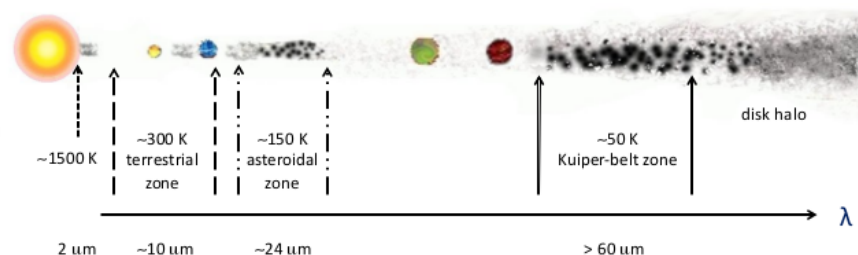


**Figure 2.7:** Dust emission on the debris disks with different wavelengths with typical temperature and regions from the star (Matthews *et al.*, 2014).

## 2. INTRODUCTION AND BACKGROUND

The clearest evidence of the presence of cold circumstellar material around main sequence stars comes from the detection of an infrared excess, which intensity peaks in different regions of the infrared and submillimetre spectrum, depending on the temperature of the grain population.

Observationally, the first evidence of debris disks was obtained by Aumann *et al.* (1984) using the Infrared Astronomical Satellite (IRAS) [1]. Aumann *et al.* (1984) detected a strong infrared excess at 25 *μm*, 60 *μm* and 100 *μm* almost ten times larger than the photospheric flux, which they attributed to cold and solid material orbiting the star. This discovery led to the expression of "Vega phenomenon" to describe debris disk-like observational properties. Further work by the IRAS investigators team led to the identification and confirmation of four debris disk stars, namely Vega (also known as Alpha Lyr), Fomalhaut, Beta Pictoris and Epsilon Eridani, as shown in Figure 2.8.
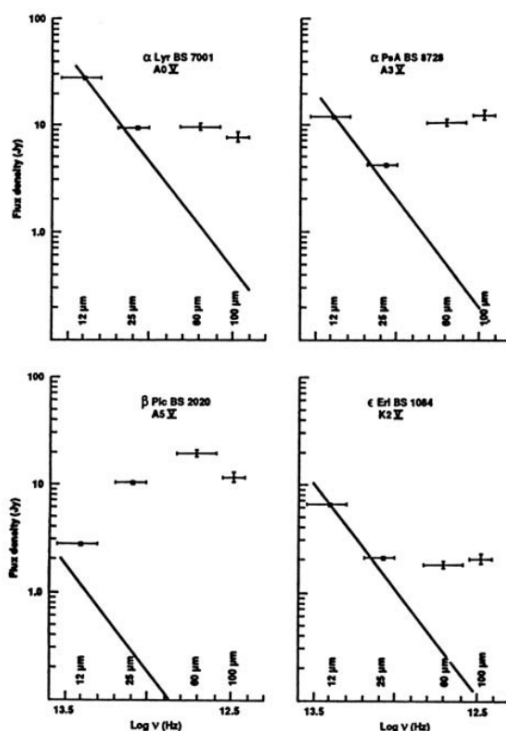


**Figure 2.8:** The Spectral Energy Distribution for Vega, Fomalhaut, Beta Pictoris and Epsilon Eridani from IRAS data (Backman, 2004).

---

[1] Infrared Astronomical Satellite-It is space telescope with diamtere 60 cm built by the United States, the United Kingdom, and the Netherlands to map the sky at infrared wavelengths of 12, 25, 60, and 100 micrometres.

In Figure 2.8 is shown the original plot by F. Gillett, co-discover of the Vega phenomenon, of the spectral energy distribution of these four objects. It is noticeable to observe that the excess at 60 $\mu m$ for Beta Pictoris is about 400 times larger than the photospheric contribution (Backman, 2004).

Few months later, the first scattered light image of the disk around Beta Pictoris was obtained with a ground-based telescope by Smith and Terrile (1984). Note that, although classified as a debris disk, the case of Beta Pictoris is somehow peculiar: the young age system ($\sim$ 8 - 10 Myr) and its large fractional excess (see below) could qualify this system as a transitional disk (Calvet *et al.*, 2002) between a young, classical protoplanetary disk and a Vega-like debris disk, as shown in Figure 2.9.
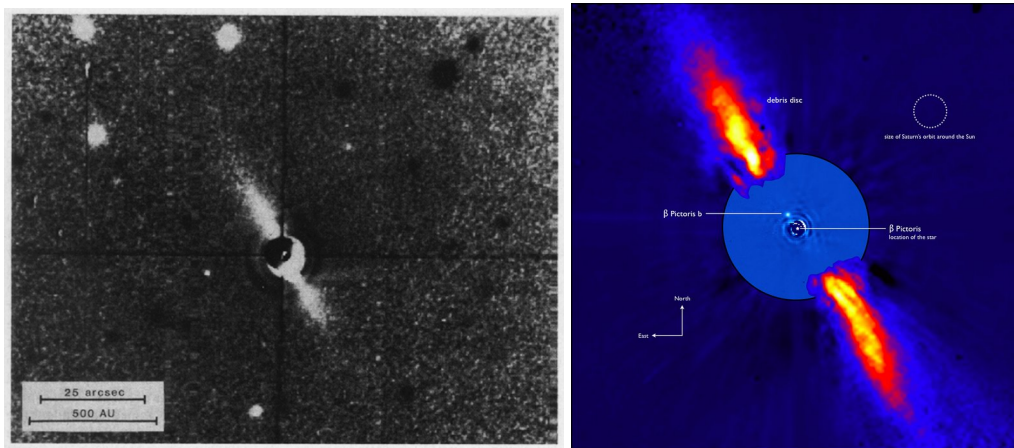


**Figure 2.9:** The left image is taken 1984 using optical telescope for Beta Pictoris star with debris disk (Smith and Terrile, 1984). The right image is for the same source as seen at 3.6 $\mu m$ with NACO on the Very Large Telescope in 1996. Image credit: ESO/A.-M. Lagrange et al. `https://www.eso.org/public/images/eso0842b/`.

Consisting of regenerated second-generation dust, debris disks are significantly less massive than PMS protoplanetary disks. Being optically thin at practically all wavelengths, their total mass can be directly and reliably estimated in the infrared spectral range. The trend of decrease in mass with increasing age of the system is visible in Figure 2.10.
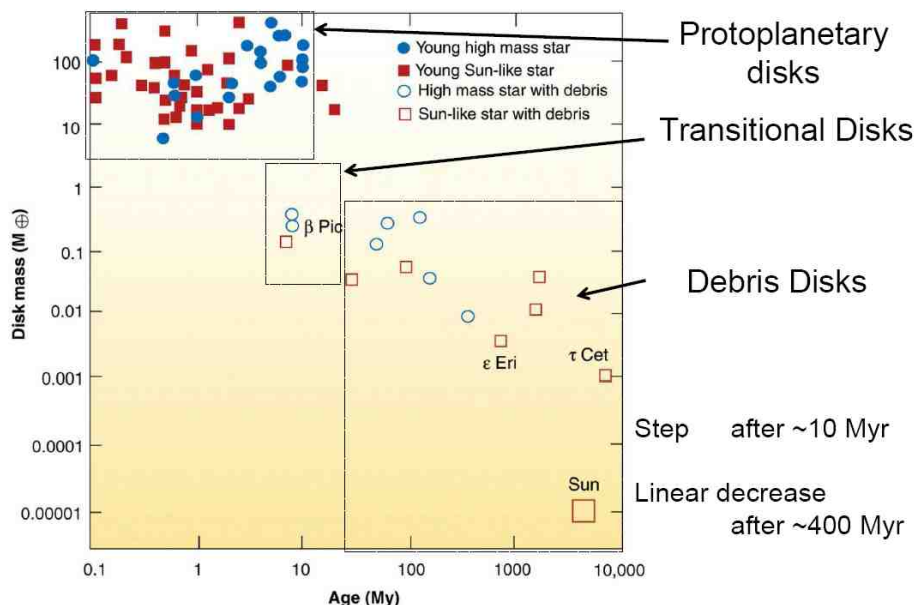
**Figure 2.10:** The plot shows the relation between the mass of the debris disk and the age of the system. The disk mass decreases linearly with increasing the age of host stars (Robson *et al.*, 2017).

Two parameters are essential to characterise the evolution of debris disks with stellar age. These are the dust temperature T and the fractional luminosity f. As a rule of thumb, these two parameters can be estimated from the wavelength and the flux of the maxima of the emission spectra of the disk and of the star through (Wyatt, 2008):

$$T = \frac{5100}{\lambda_{disk,max}} \tag{2.5}$$

$$f = \left(\frac{F_{\lambda disk,max}}{F_{\lambda*,max}}\right)\left(\frac{\lambda_{*,max}}{\lambda_{disk,max}}\right) \tag{2.6}$$

An example on how the fractional luminosity is estimated is presented in Figure 2.11. The concept of fractional luminosity can be used for a quantitative evaluation of the nature of the circumstellar emission. Debris disks will typically exhibit fractional luminosities $f < 10^{-2}....10^{-3}$, whereas protoplanetary disks present fractional luminosities $f > 10^{-2}$. With this criterion, we better understand why Beta Pictoris, with a fractional excess $f > 1$ has a controversial debris disk nature.
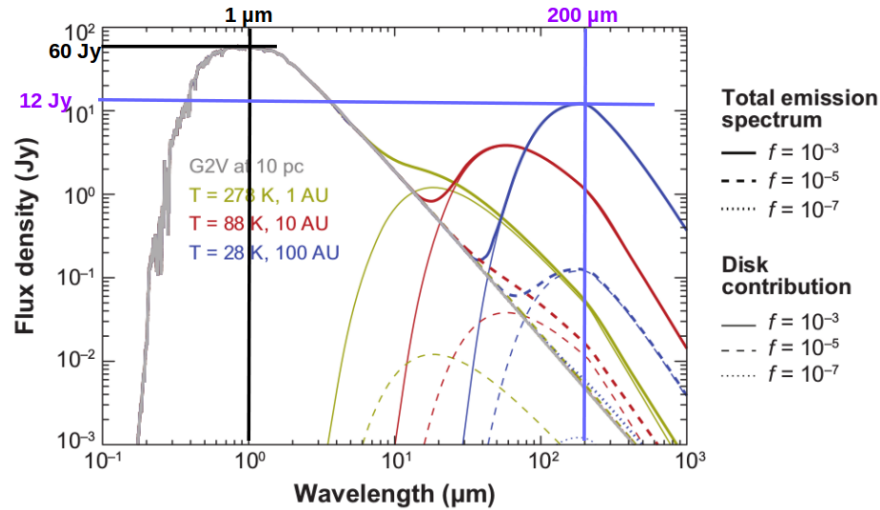
**Figure 2.11:** The figure represents the spectrum of the star type G2V at distance 10 pc and it has a debris disk. The disk consists of the dust at temperatures 278 k, 88 k, 28 k as shown in the yellow, red and blue. These temperatures correspond to the distance 1 AU, 10 AU and 100 AU. The fraction luminosity of the disk is $10^{-3}$ after extracting the maximum values of the flux and wavelengths for the star and the disk from the plot then substituted in the equation 2.6 (Wyatt, 2008).

Statistical studies of the infrared excess in debris disks, primarily with the Spitzer telescope, have been conducted to characterize the time evolution of debris disk excess around A-type stars for ages spanning between 5 and 850 Myr. These observations have been conducted at 24 $\mu m$ and 70 $\mu m$ wavelengths by Rieke *et al.* (2005) and Su *et al.* (2005), respectively. In line with the disk evolutionary scenario, the authors find that younger stars have stronger infrared excess and higher fractional luminosity than older main-seqance stars, with a decay of the fractional luminosity proportional to $\frac{t}{t_0}$, with $t_0 \sim 10$ Myr. Analog studies have been conducted around Sun-like stars of spectral type F, G, K by Carpenter *et al.* (2009). It is found that about 15 % of the stars younger than 300 Myr exhibit an infrared excess at 24 $\mu m$ whereas the rate falls to 2.7 % for older ages.

As most of the stars in the galaxy are of spectral type M, it is interesting to consider the Vega phenomenon in this stellar population. The general trend is that the rate of M dwarfs with debris disks is lower in comparison to the earlier spectral types.

## 2. INTRODUCTION AND BACKGROUND

Rhee *et al.* (2007) cross-correlated the IRAS and Hipparcos catalog to photometrically search for MIR to FIR excess around main-sequence stars with identified spectral type. They only detect one M star with infrared excess out of the ~ 900 M dwarfs of the Hipparcos catalog, namely the 10 Myr star AU Mic, which edge-on debris disk has been revealed by Liu *et al.* (2004) using the Keck adaptive optics system.

The small-size Keck MIR (10 microns) survey of Plavchan *et al.* (2005) for M dwarfs older than 10 Myr did not report any detection. Further surveys using the Spitzer space telescope has shown no detection of infrared excess for a sample of 62 M dwarfs (Gautier III *et al.*, 2007). At sub-millimeter wavelengths where cold dust is detectable and the stellar photosphere almost undetectable, Lestrade *et al.* (2006) reported a new detection of excess in the M dwarf GJ842.2 in addition to the already known excess in the young AU Mic. This result allowed the authors to derive a first estimate of 13 % detection rate in M dwarf in the age range of 20 to 200 Myr, which is comparable to the detection rate derived for A- to K-type stars (10 - 20 %). It remains unclear if the scarcity of debris disks around M dwarfs is an intrinsic property of these under-luminous dwarfs population or rather a sensitivity bias. However, the fact that the process of removal of the small grains is very fast around M-dwarf could explain in part this situation.

In his Spitzer study of the young open cluster NGC2547, (Forbrich *et al.*, 2008) detect debris disk emission at 24 microns around eleven M-type stars with ages 30 - 50 Myr. Finally. no excess emission was found for M-type stars older than 300 Myr as evidenced by Heng and Malik (2013) in their MIR Wide-field Infrared Survey Explorer (WISE) survey. Similarly to the earlier type stars, the age of the system plays an important role in the strength of an infrared excess in M dwarfs: three young stars among 18 M stars have debris disk emission around them at the age of 8 Myr at 24 $\mu m$ (Low *et al.*, 2005; Matthews *et al.*, 2007).

In order to observe debris disk dust with temperatures lower than 100 K, it is advisable to operate at longer wavelengths than 60 $\mu m$. Most detections at FIR and sub-millimetre wavelength were based on observations from IRAS and Spitzer space telescopes (Matthews *et al.*, 2014). In this way, Aumann *et al.* (1984) detected debris disk around 15 % of main sequence stars. Recent studies based on observations from Spitzer and Herschel telescopes found a higher detection rate of 20 % of debris disk around main sequence stars of spectral type A to M (Eiroa *et al.*, 2013; Matthews *et al.*, 2014; Meyer *et al.*, 2008; Rhee *et al.*, 2007). Main sequence stars of spectral type A

exhibit larger rates of debris disk detection of 33 % and 25 % at wavelength 70 $\mu m$ and 100 $\mu m$, respectively (Su *et al.*, 2006; Thureau *et al.*, 2014).

According to the Formation and Evolution of Planetary Systems (FEPS) survey and Disk Emission via a Bias Free Reconnaissance in the Infrared/Sub-millimeter (DEBRIS) surveys, the detection rate of debris disks is about 10 to 17 % for stars with spectral type F, G, K (Matthews *et al.*, 2014).

However, the DUst around NEarby Stars (DUNES) survey detected a higher rate of circa 20 % of debris disks around F-, G-, and K-type stars (Eiroa *et al.*, 2013). In the sub-millimeter Atacama Pathfinder Experiment (APEX) survey of 22 stars by Nilsson *et al.* (2010) with an age span from 5 Myr to 3 Gyr – i.e. including also younger systems such as HD 141569 or HD 152404 – reliable detections of cold dust is obtained around 10 stars (∼50 %) but, again, with a bias towards the younger objects. The SCUBA-2 Observation of Nearby Stars (SONS) survey using the James Clerk Maxwell Telescope (JCMT) at 850 $\mu m$ obtained a detection rate of the cold dust of ∼ 40 %, with new candidates not previously detected at sub-millimetre wavelengths (Thureau *et al.*, 2014). With respect to the age, one exception is found with the nearby solar-type star eta Corvi of ∼ 1 Gyr age, for which both (Wyatt *et al.*, 2005) in the sub-millimeter and (Mennesson *et al.*, 2014) at MIR wavelengths detect a strong excess indicative of the presence of a large warm dust disk at a distance of 1 - 2 AU from the central star. Considering the scarcity of strong excess detections in systems as old as 1 Gyr suggest that a transient Late-Heavy Bombardment phenomenon could be at work in eta Corvi.

| Wavelengths [$\mu m$] | Rate of Detection [%] |
|:---:|:---:|
| 8.5 - 12 | 1 |
| 24 | 4 |
| 30-34 | 11.8 |
| 70 | 16 |

**Table 2.1:** The rate of the debris disk detection against wavelengths.

## 2. INTRODUCTION AND BACKGROUND

From a spectroscopic point of view, debris disk spectra may appear featureless as in the case of HR 4796, or show advanced signposts of dust processing with the evidence of strong crystallization of the silicate grains. A spectacular example of comet-like debris disk dust is seen in HD 69830 (Beichman *et al.*, 2005), and 2 Gyr old K-type star observed at a MIR wavelength with Spitzer.

This raises also the question of tracing second-generation dust in the inner regions of a debris disk, where smaller rocky planets may have formed. In addition to the problematic of the attainable angular resolution to probe these regions, the faintness of the debris disk emission with respect to the parent star makes the question of the dynamical range a central point. Long-baseline interferometry operating in the H (1.65 microns) and K (2.2 microns) bands has been successful in tracing the location of the hot dust in the disk, i.e grains with a temperature of circa 1000 K (Absil *et al.*, 2006; Ertel *et al.*, 2014). As these high temperatures only occur in the very inner regions of the disk, interferometric observations remain as a major requirement. Recently, a study conducted with the Center for High Angular Resolution Astronomy (CHARA) interferometer was able to detect warm dust around A-type stars with higher frequency than around F-, G-, K-type stars for the 42 closest stars to our system (Absil *et al.*, 2013).

## 2.4   Planet Formation

Planet formation starts in the circumstellar disk during the pre-main sequence phase of the young star. Two competing models are proposed to explain the formation of giant planets in disks: the "core-accretion model", Pollack *et al.* (1996) suggests that a protoplanet core forms out from solid elements, which then triggers a second phase where gas from the disk is rapidly accreted by the rocky core; in the "disk instability model", Boss (2006) proposes that marginally stable disks may actually fragment into dense clumps that would become giant planets.

Laboratory models for dust and gas species have permitted to improve our understanding of possible mechanisms of planet formation. Such models must be able to explain the obvious fact that in our Solar System two groups of planets can be distinguished: the inner small-radius rocky planets and the outer giant gaseous planets. The difference between two groups of planets is in their chemical composition, where the inner planets are composed primarily by refractory materials such as Silicon, Magnesium or Aluminium, whereas the outer planets contain a significant fraction of volatile materials such as ices and thick Hydrogen- and Helium-rich atmosphere from the primordial Nebula. The radial gradient of temperature across the primordial disk may explain why the inner planets are made primarily of rocks, as opposed to the outer planets the mass of which is dominated by gas and, in particular, by ices: the inner regions closer to the central star sustain a temperature that is too high for the volatile material like ices to condense. For the inner rocky planets, their formation follows successive stages capable of growing micron-size dust particles into large rocky planetary cores. These stages are summarised in the next paragraphs.

Two questions are of particular interest in understanding the formation of planetesimals: (i) How dust particles can stick together and grow into larger planetesimals? (ii) What is the interaction process between the dust particles and the gas in the disk?

A possible answer to the first question is extracted from computer simulations and laboratory evidence of such processes. The Van Der Waals forces act to stack the dust particles gradually with each other and to form clumps of crowded particles. The answer to the second question must consider two processes in the disk. One process leads the gas and the solid particles to slowly split up from each other(Youdin and Kenyon, 2013). As a result, the gas remains in hydrostatic equilibrium whereas the solid particles begin to grow and sink toward the midplane due to the vertical gravity

component. The sinking speed of the dust grain under the influence of gravity is limited by two factors: the viscosity of the gas and the size of the grain. The possibility of collision with other grains is increased, leading to a corresponding increase in size of the grains and an increasingly faster fall towards the midplane, similar to "a snowball rolling down from the iceberg" (Eales, 2009).

The second process involved considers the differential velocity between the gas and the dust grains in rotation around the central star, which leads to a partial decoupling between these two constituents. Several scenarios of planetesimal evolution are under study, which depend on the amplitude of the mutual gravitational forces between them and cause continuous collisions (Armitage, 2010; Eales, 2009).

1. Two planetesimals may encounter and bounce back.

2. Two planetesimals may merge and form a larger planetesimal.

3. One or two planetesimals might be chopped into smaller corpses.

The sequence of collisions between small and large planetesimals mostly result in merging. As small planetesimals are not able to escape the gravitational field of larger ones, the mass of the larger object continuously increases, with a rate proportional to their mass. This results in the presence of one single planetesimal growing up to a planetary embryo at a given orbit (Youdin and Kenyon, 2013).

A planetary embryo in the inner region of a protoplanetary disk will stop growing when most dust particles have been accreted. At a distance of about 1 AU, such planetary embryos stop growing once they have reached a mass of about six times the mass of the Moon (Eales, 2009). The complex gravitational field involved in such an N-body problem affects continuously the embryos orbit and may lead either to the ejection of some of them from the Solar System, or to further merging in larger planets as seen today in the terrestrial regions. For the giant outer planets, the formation scenario first involved the formation of a ~10 $M_\oplus$ core, which then quickly accretes the surrounding gas in the protoplanetary disk. This scenario is referred to as the core-accretion model. A second model involves the sudden gravitational collapse of the dynamically unstable protoplanetary disk. The formation of numerous moons is then a consequence of this theory.

# 3

# Observation and Data Reduction

## 3.1 Atmospheric Transparency

For ground-based telescopes, Earth atmosphere also blocks most of the light at MIR wavelengths. MIR observations using ground-based telescopes are possible only through two atmospheric windows around 10 *μm* (N band) and 20 *μm* (Q band), where the transmission of the atmosphere is high due to lack of carbon dioxide or water molecules. There are two drop downs in the transmission of the sky in the MIR. The first dip is between 9.3 *μm* and 9.7 *μm*. It is due to of the ozone absorption and other kinds of molecules like water, carbon dioxide, and methane. The second big dip is caused by carbon dioxide at ∼ 15 *μm* where is high absorption for MIR wavelength in the atmosphere as shown in Figure 3.1. The transmission of the atmosphere spectra for N and Q filters is computed by the ATRAN model (CanariCam, 2014; Charles M. Telesco *et al.*, 2009; Lord, 1992).

This model is made for Cerro Pachon (Gemini South Telescope, 2722 m) at the airmass of 1.5 for three different values of Precipitable Water Vapor (PWV). The red line represents the atmospheric transmission for a PWV of 2.3 mm, the blue line represents the atmospheric transmission for a PWV of 4.3 mm and the green line represents the atmospheric transmission for a PWV of 10 mm (CanariCam, 2014).
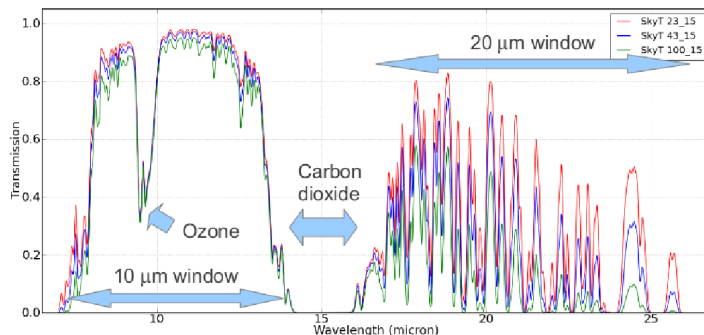
**Figure 3.1:** The figure shows the sky transmission model for the MIR wavelengths with different values of the water vapour 2.3, 4.3 and 10 mm (Iglesias, 2014).

## 3.2 Precipitable Water Vapour

Beside ozone and carbon dioxide, there is another source of absorption at MIR wavelengths which is water vapour. The PWV is changing at the top of the telescope site and affects the sky transmission for MIR and reduce it. Moreover, the sky thermal background emission changes with the changing PWV as shown by curves for 1.0 and 3.0 mm of ($H_2O$) in Figure 3.2.
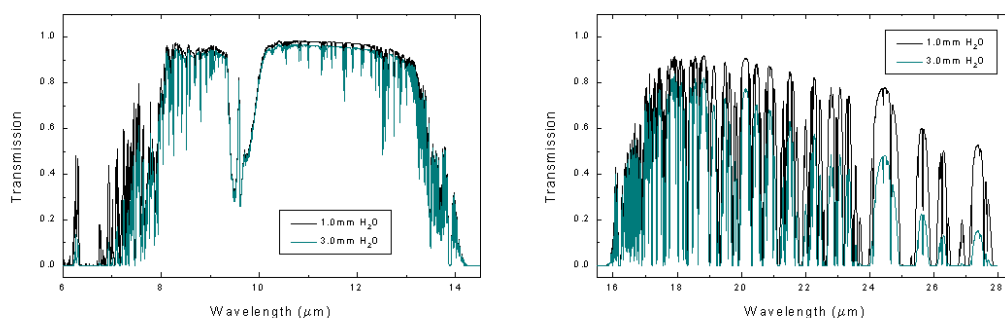


**Figure 3.2:** Figures show the effect of an increase in the water vapour above the site which generally causes an overall reduction of transmission, and consequently the sky background increases for the MIR in N band (Left) and Q band (Right) (Gemini, 2016).

In addition to that, the N and Q band windows do not have the same percentages of transmission for MIR. The water molecules dominate the atmospheric absorption in the Q band and it is greater than that in the N band.

The Q window has a maximum transmission at about 18 $\mu m$ and this transmission is declining gradually with wavelength. N band observations are much less sensitive to PWV than Q band observations. If the value of the PWV is between 5 and 10 mm that indicates a good observation for N band and critical observation for Q band. The observations are considered to be perfect for both bands N and Q, if the PWV value is < 5mm (CanariCam, 2014; Gemini, 2016).

The Global Positioning System (GPS) has frequently monitored the PWV at the Observatorio del Roque de los Muchachos (ORM), where the Gran Telescope Canarias (GTC) is based. The PWV statistical analysis provides that PWV changes seasonally. The best seasons are in winter and spring (February, March, April) when 60% of the nights have less than 3 mm of PWV. On the other hand, the worst season is August and September where 10% of nights have greater than 3 mm of PWV (García-Lorenzo *et al.*, 2010).

## 3.3   Sky and Telescope Emission

Sky emission and telescope emission represent the two main contributions to be thermal background in the IR. The thermal background also is variable with time and space. The information about the sky emission in the MIR is not available above GTC observatory at ORM site. But, is available for Gemini observatory at the Cerro Pachon site where the MIR sky emission curves are calculated using ATRAN models by Lord (1992) and simulated for the conditions at the Cerro Pachon site. As shown in Figure 3.3 we can see the relation between PWV and sky emission. When the PWV increases from 2.3 to 10 mm, the sky emission in the N band window increases by 5% and in the Q band the sky emission increases by 30%. The GTC telescope emission was measured at 10° and 20° Celsius in the CanariCam wavelength operating range on April 2013. There are different ways used to reduce the telescope emission such as (CanariCam, 2014):

1. The size of the secondary mirror of GTC is reduced and a small portion of the primary mirror is vignetted to prevent thermal emission from structures outside the primary mirror to enter the CanariCam.

2. Inserting a mask between the secondary mirror and the support spider to prevent the thermal emission from spider to reach the detector.

3. The physical separation between segments mirrors in the primary mirror is kept below 3 mm.

4. Regular cleaning of the GTC mirrors using CO2 snow to avoid accumulation of the dust on the mirrors, especially during the summer.
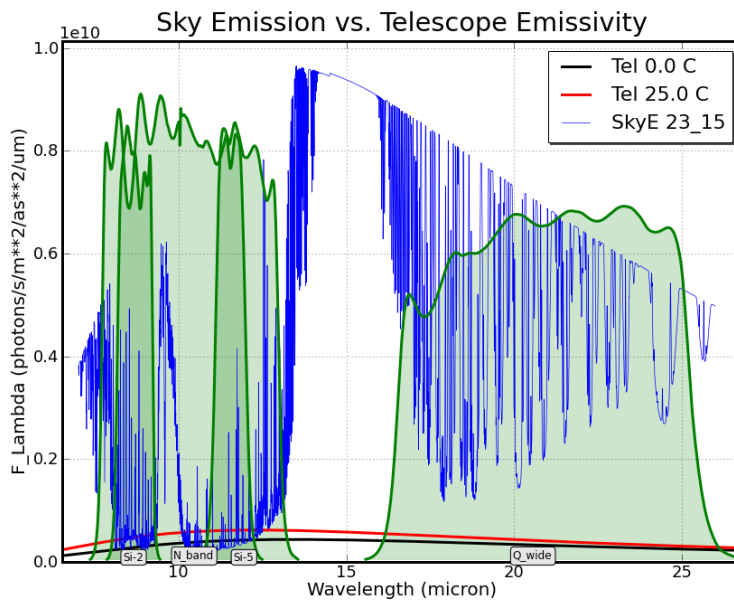


**Figure 3.3:** Sky emission for PWV=2.3 mm and airmass=1.5 in blue thin line, and telescope emission at temperature 10 C° in black line and 25 C° in red line with emissivity 5%. The green shadow area represents the CanariCam bands(CanariCam, 2014).

## 3.4 Point Spread Function

The Point Spread Function (PSF) represents the distribution of light from a point source at the detector. According to the Huygens principle, light travels as a wave at the same speed in all directions inside an isolated and homogeneous medium, this wave can be described in terms of the wavefront where each point in this wave front has the same properties of the source (Schroeder, 2000). This is shown in Figure 3.4.
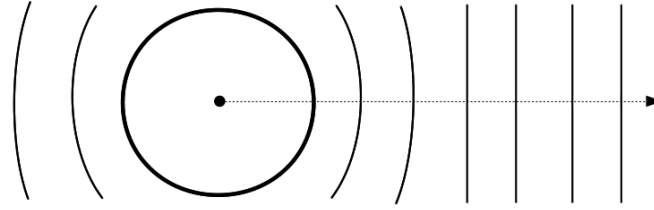


**Figure 3.4:** The progression of a wavefront from a point source.

The point spread function is defined as the instrumental response of the telescope aperture. When a plane wavefront from a distant point source passes through a circular aperture (telescope), the corresponding image of the source observed through the aperture will have a Bessel function. This is known as the PSF of the telescope.

The output image I(x,y) is formed from the source of the light $S(x_0, y_0)$ and has dimension $N \times N$. This output image can be express mathematically (Saha, 2010):

$$I(x, y) = \sum_{x_0=1}^{N} \sum_{y_0=1}^{N} S(x_0, y_0) \times P(x_0, x, y_0, y) \tag{3.1}$$

Where $P(x_0, x, y_0, y)$ is the point spread function and show how much the input value at position ($x_0$, $y_0$) has effects on the output value at the position $(x, y)$. In case the point spread function depends only on the position of the affecting and affected pixels, then we have to shift the point spread function:

$$P(x_0, x, y_0, y) \equiv P(x_0 - x, y_0 - y) \tag{3.2}$$

Then the output image $I(x, y)$ can be written as:

$$I(x, y) = \sum_{x_0=1}^{N} \sum_{y_0=1}^{N} S(x_0, y_0) \times P(x_0 - x, y_0 - y) \tag{3.3}$$

Also, it is known as a convolution image. The general expression of the output image can be achieved by taking the integral of the brightness of the source times the PSF:

$$I(x, y) = \int \int S(x_0, y_0) \times P(x_0 - x, y_0 - y) dx dy \tag{3.4}$$

The equation above is convolution. Let's assume, we have a perfect optical system (P) to observe a point source (S) without any atmosphere turbulence (seeing effect). The out image (I) from this optical system will be the same as of the PSF of (P)(Petrou and Petrou, 2010).

## 3.5 High Angular Resolution

The resolution of the telescope is the ability of the telescope to resolve two sources that are very close from each other. The angular resolution ($\theta$) of the telescope in radians is given by (Schroeder, 2000):

$$\theta = \lambda/D \tag{3.5}$$

where $\lambda$ is the wavelength and D is the diameter of the telescope.

The formula of the diffraction limit of the telescope is derived from the single-slit diffraction limit. By considering, the waves plate of the light are coherent and passing through the circular aperture of the telescope instead of single-slit. When wave plate passes through the circular aperture, the diffraction pattern (Fraunhofer diffraction) can be observed on the detector as the output image. The diffraction pattern is appeared as concentric dark and bright rings known as an Airy Disk (Allen and Triantaphillidou, 2012). For source observed from very far distance is formed the Airy pattern with maximum intensity circle in the center and gradual decrease in the intensity with increasing in the distance from the source. The first center bright circle is surrounded by much fainter concentric circular dark and bright rings. This central bright circle of the diffraction pattern is known as the Airy disk. The intensity distribution of the Airy disk can be described mathematically by using this formula (Schroeder, 2000)

$$I(\theta) = I_0 \left(\frac{2J_1(x)}{x}\right)^2 \tag{3.6}$$

This equation represents the intensity distribution on the detector, where $I_0$ is the maximum intensity distribution in the first circle of the Airy pattern.

$J_1$ is the first order of Bessel function and x = kDsin$\theta$, where D is the aperture of the telescope and k is the wave number. Here $\theta$ is the angle between the optical axis and axis from the center of the telescope aperture to the first minimum ring in the screen. By approximating equation 3.6 to the first order, the first minimum is achieved at $x_0$ = 3.8317 or 1.22$\pi$. Substituting this value into $J_1$, we get:

$$\sin(\theta) \approx \theta = 1.22\frac{\lambda}{D} \tag{3.7}$$

This is known as the Rayleigh criterion for the diffraction limit of the telescope. The figure below shows the Rayleigh criterion (Allen and Triantaphillidou, 2012):
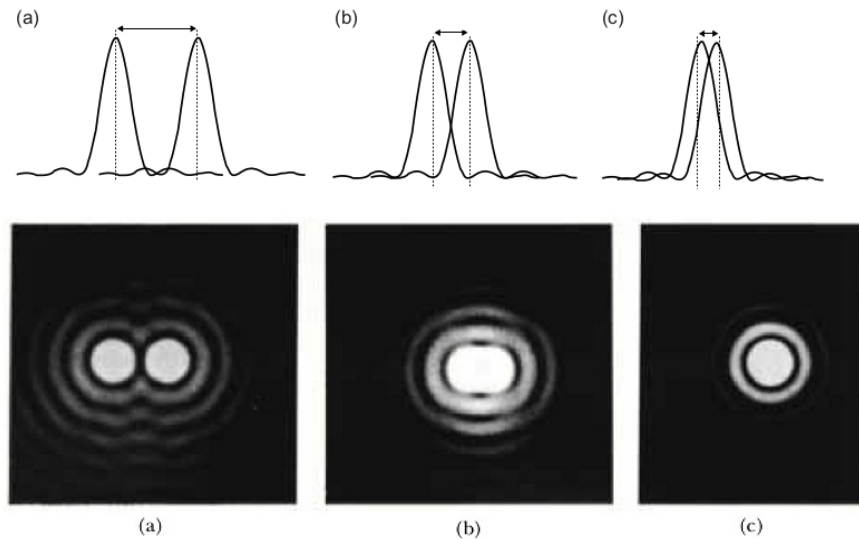


**Figure 3.5:** The figure shows two profiles for two sources. The first row is intensity profile in 1D and second row in 2D: (a) completely resolved. (b) partially resolved. (c) unresolved.

## 3.6 Diffraction and Seeing Limit

The resolution of the observation using ground-based telescopes is also affected by the turbulence of the atmosphere, which refers to the blurring and twinkling of images. Due to the distortions caused by atmospheric turbulence, the resolution of the ground-based observations is given by:

$$\theta = D/r_0 \tag{3.8}$$

where $r_0$ is the Fried parameter, the size of the largest aperture which is diffraction limited and not affected by the atmospheric turbulence. Tatarski (1961) found that for a Kolmogorov model of the atmospheric turbulence, the Fried parameter $r_0$ scales with wavelength as (Saha, 2010):

$$\alpha_{seeing} = (\lambda/r_0) = \lambda^{-1/5} \tag{3.9}$$

According to above relation, with an 8 meter telescope and a good observing site, where seeing in the optical is $\sim 1''$, one can expect diffraction-limited observations at 20 $\mu m$. The seeing disk in the optical can be as small as 0.4'' - 0.5'' under the best conditions. Therefore, 8-to-10m diameter telescope at a good site is thought to be the best combination for high-angular resolution observations in the MIR (Charles M. Telesco *et al.*, 2009; Gemini, 2016).

## 3.7 Ground-Based Telescope

The Gran Telescopio CANARIAS / The Great Canary Telescope (GTC) is considered one of the largest and most advanced ground-based telescopes for optical and infrared wavelengths in the world. The telescope is located at the ORM on La Palma at an altitude of 2400 m (above the sea level) on the Canary Island of Spain at a latitude of 28° 45′ north and a longitude of 17 ° 53′ west. The ORM observatory site represents one of the best observatory sites in the world due to its stable and good climate conditions for astronomical observations. For instance, the diffraction limit of the Spitzer space telescope at wavelength 20 $\mu m$ is 5.5'', while for GTC ground-based telescope at wavelength 20 $\mu m$ is 0.5''. This means that the resolution of the GTC is ten times better than that of the Spitzer telescope but the sensitivity limit of the latter one is higher due to

the lack of the absorbing atmosphere. The GTC telescope is composed of primary and secondary mirrors. The primary mirror consist of 36 individual hexagonal segments making up the total diameter of 10.4 m. The secondary mirror has a diameter of 1.2 m (CanariCam, 2014; Charles M. Telesco *et al.*, 2009).



**Figure 3.6:** The Gran Telescopio Canarias or GTC, La Palma,Spain. Image credit: GTC http://www.gtc.iac.es/.

There are eight instruments which can be used with the GTC telescope. Some of them are available now and others in the future. Here is the list of the available instruments[1]:

1. Optical System for Imaging and low-Intermediate-Resolution Integrated Spectroscopy (OSIRIS): is an imager and spectrograph for the optical wavelengths (0.365 $\mu m$ - 1.05 $\mu m$).

2. CanariCam: is a MIR imager (7.5 $\mu m$ - 25 $\mu m$) with additional capabilities such as a Spectroscopic, Coronagraphic, and Polarimetric.

3. Canarias InfraRed Camera Experiment (CIRCE): is a NIR camera working in the wavelength range between (1 $\mu m$ - 2.5 $\mu m$) (JHKs filters).

4. Especrografo Multiobjecto Infra-Rojo (EMIR): is the second-generation GTC instrument and it is a NIR (0.9 $\mu m$ - 2.5 $\mu m$) wide-field imager, medium-resolution multi-object spectrograph.

---

[1]http://www.gtc.iac.es/instruments/instrumentation.php

### 3.7.1 The CanariCam Instrument

The CanariCam is a MIR imager with different modes or capabilities: spectroscopic, coronagraphic, and polarimetric. It covers a wide range of MIR wavelength from (7.5 $\mu m$ - 26 $\mu m$). It was built by the University of Florida and the first light was received in 2013. The CanariCam was installed on the Nasmyth-A platform at the GTC telescope from 2014 until 2016. Now, CanariCam has been moved to a folded Cassegrain focus platform. The CanariCam optics is designed to reach the diffraction limit at 8 $\mu m$ (Nyquist sampling).

The detector of the CanariCam uses a Raytheon CRC-774 Si:As, Impurity Band Conduction (IBC) or Blocked Impurity Band (BIB), high - background infrared Focal Plan Array (FPA) with an 320×240 array. The detector has a field of view of 26″ × 19″ and plate scale 0.08 arcsec/pixel (CanariCam, 2014). The whole system, which consistes of CanariCam optics and the detector put together in a hexagonally shaped dewar, is shown in Figure 3.7.

For cooling the detector and making it work with temperature of 9 K a He cryo-cooler system has been installed. The two layers of radiation shields are installed to protect the dewar from thermal background emission and also, to keep the low temperatures 28 K inside the dewar. The optical system of CanariCam has three powered mirrors, six folded mirrors and two additional mirrors which are added when need be. Mirrors are reflective to reduce achromatic and stray light scattering (Packham *et al.*, 2005).

All mirrors are gold-coated, diamond-turned and made of aluminum as the optical bench and mounts, so that it makes all optical system homologous and cool down at the same time. There are three entrance windows installed in a window turret: ZnSe, KBr and KRS-5 to add more options for observing conditions. Each window has a different diameter, thickness, transmission, and emissivity.

The first window (ZnSe window) has 50 mm diameter, 6.0 mm thickness and 0.4% emissivity. The transmission of the ZnSe is 94 % at wavelength 10 $\mu m$ (N band) which is perfect for observing, but is opaque in the Q band.

The second window (KBr window) has 50 mm diameter, 10 mm thickness with a slightly lower transmission compared to the ZnSe window. The KBr window is good for the two MIR windows 10 and 20 $\mu m$ (N and Q band) and is weak for water (soluble), so it cannot be used under higher-humidity condition.
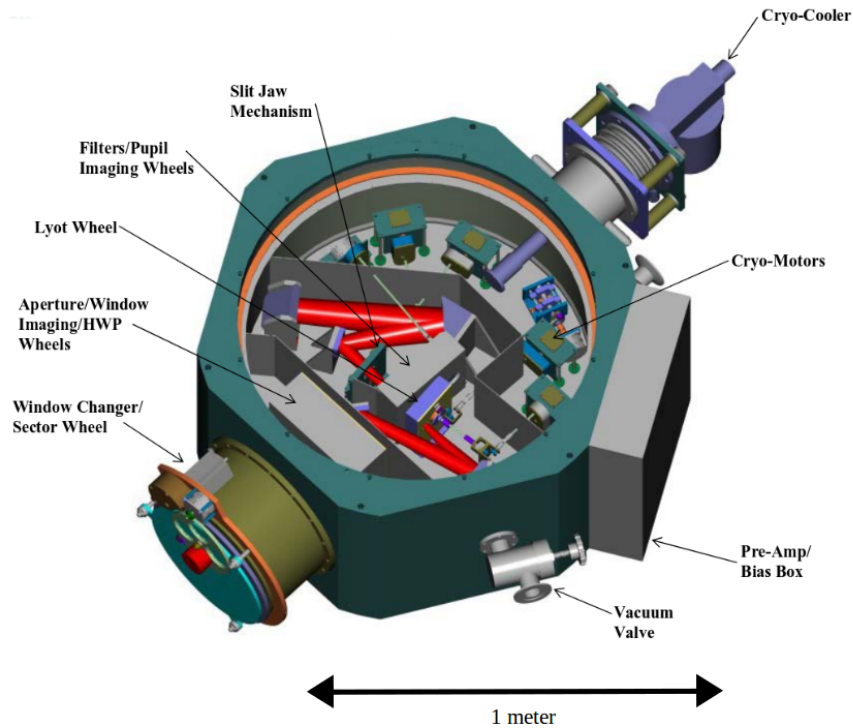
**Figure 3.7:** The CanariCam dewar, illustrating its overall shape and accessories including the coldhead, optical bench and window turret. The CanariCam optics and mechanisms are distributed on both sides of the optical bench and relayed by two fold mirrors (Jeffrey A. Julian, 2014).

The third window (KRS-5) has a diameter of 48 mm, thickness of 6 mm with emissivity 0.3 %. The transmission of the KRS-5 is greater than 70 % for the wavelength range 2 - 35 $\mu m$ and can be used when the humidity is high (Charles M. Telesco *et al.*, 2009).

## 3.7.2 Observing Modes of the Telescope

The telescope can be operated in different modes: Imaging mode, Spectroscopy mode, Polarimetry mode, and Coronagraph mode.

### 3.7.2.1 Imaging Mode

The optical system as I mentioned previously, has three power mirrors laid in the optical path. The first powered mirror, called transfer mirror (M1), re-images the telescope

focal plane after forming an image of the telescope entrance pupil. The second powered mirror, called collimator (M2), has to collimate the beam forming a second image of the pupil. The third powered mirror, called camera mirror (M3), has the last important duty by forming the image onto the detector. Other flat mirrors can be inserted near the final pupil image (p2) for imaging or spectroscopy. Figure 3.8 shows the optical system layout for CanariCam (CanariCam, 2014).
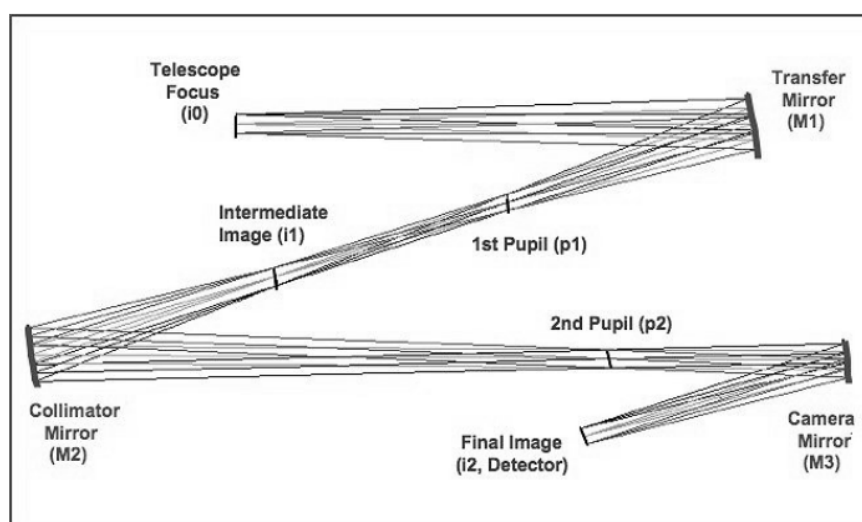


**Figure 3.8:** Optical system for CanariCam in the imaging mode. Image credit: GTC http://www.gtc.iac.es/instruments/canaricam/canaricam.php.

The primary mode of CanariCam is the imaging mode. Other modes, can be done by inserting additional flat mirrors at appropriate positions in front of the light path. The detector QE (Quality Efficiency) has the ability to break off wavelength when reaching the red end near 25 $\mu m$. CanariCam has a double filter wheel at the first pupil image (p1), supplied with up to 26 different filters to select according to the scientific aim. Table 3.1 shows the filters in the CanariCam instrument (Charles M. Telesco *et al.*, 2009). The imaging sensitivity for all CanariCam filters has been obtained on $29^{th}$ of January 2013 using the MIR standard HD 3712 for average background conditions at the ORM (PWV = 7 mm). The sensitivity is calculated in mJy and corresponding to $5\sigma$ detection in 30 minutes on-source as shown in Table 3.2 along with Full Width Half Maximum (FWHM) of the PSF for each filter (CanariCam, 2014).

| No. | Filter | $\lambda$ ($\mu m$) | $\Delta\lambda$ ($\mu m$) | FWHM (Arcsec) | Sensitivity (mJy) | Sky Transmission |
|---|---|---|---|---|---|---|
| 1 | Si1 | 7.8 | 1.1 | 0.17″ | 4.11 | > 60% |
| 2 | PAH1 | 8.60 | 0.43 | 0.19″ | 1.70 | > 70% |
| 3 | Si2 | 8.7 | 1.1 | 0.19″ | 0.82 | > 60% |
| 4 | ArIII | 8.99 | 0.13 | 0.20″ | 3.83 | > 70% |
| 5 | Si3 | 9.8 | 1.0 | 0.21″ | 2.75 | > 60% |
| 6 | Si4 | 10.3 | 0.9 | 0.22″ | 1.69 | > 60% |
| 7 | N (*) | 10.36 | 5.2 | 0.23″ | 2.02 | > 80% |
| 8 | SIV | 10.5 | 0.16 | 0.23″ | 4.04 | > 70% |
| 9 | PAH2 | 11.3 | 0.60 | 0.25″ | 2.01 | > 70% |
| 10 | Si5 | 11.6 | 0.9 | 0.25″ | 1.22 | > 60% |
| 11 | SiC (*) | 11.75 | 2.5 | 0.26 ″ | 1.94 | > 80% |
| 12 | Si6 | 12.5 | 0.7 | 0.27″ | 2.98 | > 60% |
| 13 | NeII | 12.81 | 0.2 | 0.28″ | 6.98 | > 60% |
| 14 | NeII | 13.10 | 0.2 | 0.29″ | 5.92 | > 70% |
| 15 | QH2 | 17.0 | 0.4 | 0.37″ | 32.80 | > 60% |
| 16 | Q1 | 17.65 | 0.9 | 0.38″ | 10.84 | > 70% |
| 17 | Q4 | 20.5 | 1.0 | 0.45″ | 8.58 | > 70% |
| 18 | Qw (*) | 20.9 | 8.8 | 0.45″ | 13.32 | > 60% |
| 19 | Q8 | 24.5 | 0.8 | 0.53″ | 27.58 | > 60% |

**Table 3.1:** Theoretical of the diffraction limit of GTC in each filter FWHM. (*) star mark represents the filters that should not be used when observation are in the high background conditions (PWV > 3 mm for N and Qw band, and PWV > 5 mm for SiC), otherwise detector will saturate with the minimum frame time available in the CanariCam readout mode (CanariCam, 2014).

### 3.7.2.2 Spectroscopy Mode

To operate in spectroscopy mode a slit should be inserted at the focus (I0) in Figure 3.8, and a grating at the second pupil image (p2). Spectroscopy mode can achieve two types of spectral resolutions (Low Resolution and High Resolution) for each filter (N and Q band) by installing four plane gratings on a small rotatable turret at p2. The low resolution mode (Low-Res. mode) can capture a spectrum of the source in the entire

## 3. OBSERVATION AND DATA REDUCTION

| Filter | FWHM (Arcsec) | FWHM (Pixel) | Sensitivity (mJy,5-$\sigma$ in 30min on-source) | PWV (mm) |
|---|---|---|---|---|
| Si1-7.8 | 0.24 | 3 | 6.94 | 7.2 |
| Si2-8.7 | 0.25 | 3.12 | 2.15 | 7.2 |
| Si3-9.8 | 0.25 | 3.12 | 3.00 | 7.6 |
| Si4-10.3 | 0.28 | 3.5 | 2.69 | 7.6 |
| Si5-11.6 | 0.30 | 3.8 | 3.02 | 7.6 |
| Si6-12.5 | 0.34 | 4.25 | 6.43 | 7.6 |
| Q1-17.65 | 0.44 | 5.5 | 22.81 | 6.8 |
| PAH1-8.6 | 0.25 | 3.12 | 2.03 | 7.6 |
| ArIII-8.99 | 0.26 | 3.25 | 5.29 | 6.6 |
| SIV-10.5 | 0.29 | 3.62 | 5.02 | 6.6 |
| PAH2-11.3 | 0.33 | 4.13 | 3.38 | 6.6 |
| SiC-11.75 | 0.32 | 4 | 3.57 | 7.6 |
| NeII-12.8 | 0.33 | 4.13 | 8.46 | 7.2 |
| NeII-ref2-13.1 | 0.34 | 4.25 | 8.73 | 7.2 |
| QH2-17.0 | 0.44 | 5.5 | 50.10 | 6.8 |
| Q4-20.5 | 0.50 | 6.3 | 33.32 | 7.6 |
| Q8-24.5 | 0.59 | 7.38 | 95.62 | 7.6 |

**Table 3.2:** CanariCam filters with value of FWHM for HD 3712 (CanariCam, 2014).

N band (spanning 7.4 - 13.5 $\mu m$) or in the Q band (spanning 15.7 - 25.3 $\mu m$). The high resolution mode (Hi-Res. mode) is set up by adjusting the grating to the center of the detector for any wavelength in N or Q band. To scan the whole atmospheric window, we need to have multiple settings of the grating.

Nine slits are available for offering flexibility to be used to match the wavelength, resolution and observing conditions. The slit width is ranging between 0.17″ to 1.04″ to cover a range of the wavelength from shortest wavelength in the N band to the Q band. (See Table 3.3).

The resolving power ($\lambda/\Delta\lambda$) for the low resolution spectrum and high resolution spectrum is measured in two bands N and Q. The resolving power values for Low-Res. are approximately 160 at 10.3 $\mu m$ and 130 at 17.5 $\mu m$, and resolving power values for the Hi-Res. are 1300 at 10.5 $\mu m$ and 730 at 20.5 $\mu m$.

| Slit Width [arcsec] | Slit Width [Pixel] | 10 $\mu m$ Diffraction Limited Central $\lambda$ [$\mu m$] |
|---|---|---|
| 0.17 | 2.15 | 7.0 |
| 0.20 | 2.5 | 8.3 |
| 0.23 | 2.88 | 9.5 |
| 0.26 | 3.25 | 10.7 |
| 0.36 | 4.5 | 14.9 |
| 0.41 | 5.13 | 16.9 |
| 0.45 | 5.62 | 18.6 |
| 0.52 | 6.5 | 21.5 |
| 1.04 | 13 | Seeing limited |

**Table 3.3:** Slit width and wavelength for CanariCam (Charles M. Telesco *et al.*, 2009).

In general, the sensitivity measurements in the low resolution for N band have a range from 50 mJy to 150 mJy, and for Q band from 300 mJy to 800 mJy ($5\sigma$, 30 minutes integration time on the source). These values change according to different factors like the airmass, seeing condition and PWV (Charles M. Telesco *et al.*, 2009).

### 3.7.2.3 Polarimetry Mode (Dual-beam polarimetry)

Dual-beam polarimetry is considered the first time available at MIR wavelengths by CanariCam, currently only for N band spectral region. This mode needs three other components to be added into the beam :

1. A cooled, rotatable CdSe half-wave plate (HWP) within the cryostat located just in front of the telescope focal plane. The HWP is rotating sequentially to four (detent-determined) orientations (0, 22.5, 45, and 67.5 degrees), with images being taken at each HWP orientation. At each orientation, O ray and E ray (ordinary and extraordinary ray) images are recorded simultaneously by the detector.

2. A focal plane mask at the telescope focal plane which is used to prevent overlap between images of the two beams (O ray and E ray).

3. A wollaston prism (Analyzer) located just up-stream from the grating turret. The prism is inserted into the beam on a slide, and produces an angular separa-

tion ($\sim$ 2.8 measured on the detector plane) between the orthogonally polarized states, hence producing two beams the so-called O and E rays.

| Filter | Polarization Efficiency(%) |
|---|---|
| Si1-7.8 | 72.1 |
| Si2-8.7 | 90.0 |
| Si3-9.8 | 97.3 |
| Si4-10.3 | 99.2 |
| Si5-11.6 | 95.5 |
| Si6-12.5 | 88.3 |

**Table 3.4:** Polarization efficiency for Silicate filters.

The benefit of having four orientation angles is to minimize the influence of changes in atmospheric transparency, the seeing, and to increase observational efficiency (Packham *et al.*, 2005). The polarization efficiency was measured during the commissioning run in 2012 and the results are given in Table 3.4 for N band.

### 3.7.2.4  Coronagraph Mode

This mode is used to block the emission in the PSF wings of the bright source to improve the ability for detecting faint MIR point sources, such as sub-stellar objects, and faint extended emission from a disk (circumstellar disk). There are two components that must be inserted in front of the beam to apply this mode:

1. A hard-edged (top hat), low-reflectively focal plane mask of 0.83″ in radius at i0.

2. A hard-edged Lyot stop with a spider mask resembling the telescope pupil at p1.

Plate scale of the coronagraphy is the same as for the imaging mode (0.08″). The lab simulation shows that, at 1″ from the image peak, the intensity of a bright point source is at least 10 times lower in the coronagraphic mode than in the normal imaging mode.

## 3.8 Observation Technique

### 3.8.1 Chop - Nod

The technique which usually use to achieve the optical observations is not worth to use it for MIR observation. In the MIR, there are high thermal background contribution from Earth atmosphere, telescope mirrors, metals which hold the mirrors and detectors. Besides that, the thermal background emission is not only high in the MIR but also greatly unstable with time. Therefore, the chop-node technique is used to reduce thermal background effect.

Chop represents the telescope pointing to the source in the sky, and this allows the detector to take an image of the source plus the sky (on - source). The second mirror tilts slightly to another chop position and takes another image with only the sky (off - source). Subtracting the source + sky image with pure sky image removes the contribution of the background flux and it is called a saveset frame. The saveset frame consists of a positive and a negative source see Figure 3.9.

The change in the chop position from (on - source) to (off - source) is called chop throw. The chop throw is the angular distance between the (on - source) and (off - source) and measured in arcsec. The chop throw angle is very small to avoid the big change in the sky background. Also, the chop iteration should be fast to reduce the effect of fast variation of the sky emission. For most observations with GTC/CanariCam or Gemini / T-ReCS, a 15″ chop throw is used. Nod represents the telescope movement to another position. Also, is called "beam switch". This movement of the telescope occurs on time scales of tens of seconds. Then follow the same procedure in the nod position from chop on-source than chop off - source. To make more simple, the Chop procedure is performed by a slight move of the secondary mirror to get (on and off source) while the Nod procedure is performed by movement of the telescope itself.

Nod A is the first nod position, the telescope is pointing to the target and achieves the first chop position (on - source), then the second one (off - source). Nod B is the second nod position, the first chop position achieved (off - source), then the second one achieved (on - source) as shown in Figure 3.9. Nod is very important for a more fully thermal background removal. If the sky emission is irregular, it can be removed out through by a pair of nods (CanariCam, 2014; Gemini, 2016).
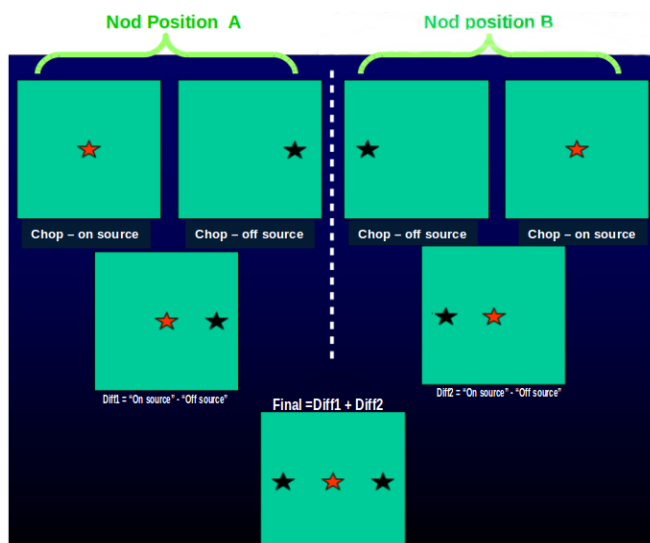
**Figure 3.9:** Illustration of chop-nod technique in the GTC telescope. Image credit: GTC
http://www.gtc.iac.es/instruments/canaricam/canaricam.php

## 3.9    Data Reduction

is a process which have to follow after observation to correct the data from any impurities and reduce other effects. The challenge in the MIR data reduction, where background emission have high emission, is how to recover the target flux very precisely from high background effect and other image artefacts. For high angular resolution, the important step is to recover the PSF of the observation accurately. Mostly, there are standard steps or pipelines for data reduction for each instrument. CanariCam instrument uses Flexible Image Transport System (FITS) files to save data. FITS is the standard archival data format for the astronomical data set. The FITS files contain not only information about the target, but also have in the header of files a very useful information about the size of image, instrument, telescope, coordinates, dates of observation ..etc.

The detector of CanariCam must be readout the frame very fast (20 - 30 millisecond) to avoid saturation in the detector and generating a huge number of data inside the camera. A good frame is added every 5 to 10 seconds to form "saveset" and reject bad frames by internal pipelines. Saveset can be defined as the smallest unit of output data that is saved in the FITS file. The CanariCam can select the frame time and numbers of frames for each saveset automatically. Several hundreds of the FITS file are reached

at the end of observation. The data are stored as [320,240,2,N] where 320×240 is the dimension of the image in pixel, 2 is the number of the chop positions at each nod position and there are two chop positions for each saveset, N is the number of saveset per nod. Saveset has two frames: one on-source frame and one off-source frame (Sky). There are two nod position can be applied in the CanariCam even ABAB or ABBA. A Nod is applied by the first frame for on-source and the second frame for off-source, while B is applied by the first frame for off-source and the second frame for on-source (Charles M. Telesco *et al.*, 2009).

I have used iDealCam software for data reduction, which is built in Interactive Data Language (IDL) program by (Li, 2014). iDealCam is using IDL GUI application for processing raw FITS data which are produced by CanariCam (Li *et al.*, 2013). iDealCam software can provide the astronomers a very efficiency and easy tool to upload the data to view images, reduce, and analyze multi-extension FITS files. In fact, raw MIR FITS files are like a very short movie rather than a single image, consisting of a large number of chop and nod frames. To see the final image of the observation, its need to combine all saveset together by using stacking image in the iDealCam. iDealCam is a FITS viewer and it is supporting different analyzing tools, aperture photometry, signal-to-noise measurements, is also has a polarimetry reduction tool. iDealCam is not modified to work for CanariCam imaging and polarimetry data only, but it can also deal with another type of data produced by T-ReCS (MIR camera of Gemini South), and Michelle (MIR camera of Gemini North). Figure 3.10 shows the graphical user interface for iDealCam.

## 3.10   Calibration Stars

Calibrators stars are very useful and used to compare the PSF or photometric of the standard stars with science star. Cohen standard stars are a list of 422 giants or super-giants stars, have a spectrum K or M type. Standard stars are known stars for us like flux, spectrum and used for calibration the observation. The calibration stars in Cohen list are based on the primary and secondary standard. The two Cohen's primaries are Alpha Lyr (A0 V) and Alpha Cma (A1 V). The ten Cohen's secondary are Beta And, Alpha Cet, Alpha Tau, Beta Gem, Alpha Hya, Mu Uma, Gamma Cru, Alpha Boo, Gamma Dra, Beta Peg. The spectral templates of the calibration stars can be useful to do a flux calibration not only MIR imaging but also low-resolution spectroscopy by
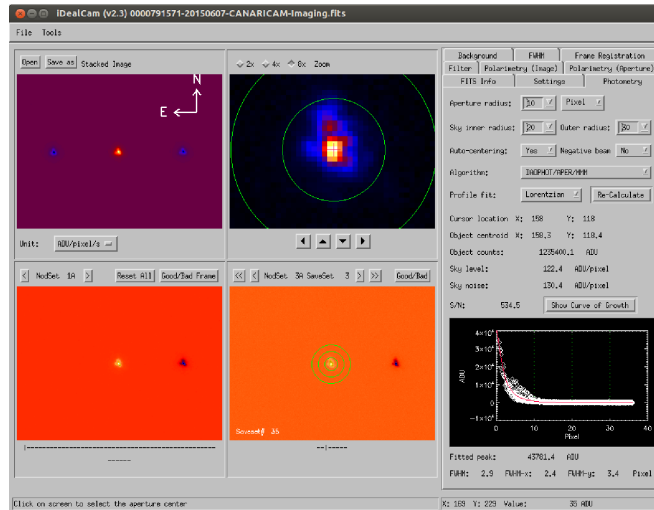
**Figure 3.10:** The iDealCam interface has two panels. The left panel is continued four screens to display the final stacked image and select Saveset/Nodset frames, whereas the right panel has a differents tools for data reduction.

smoothing to the appropriate resolution. The image quality of the telescope is measured by observing the PSF of the standard stars. The Cohen standard stars can be used for PSF calibration but not all cases are suitable for the PSF calibration. It is better do not use the supergiants standard stars for PSF calibration because they may have extended emission from the dust shell. The alpha Lyra (Vega) can be considered not suitable for PSF calibration due to the Vega star is known to have dust debris disk. I used Cohen standard stars in my observations for three aims for flux calibration, for PSF comparing and for spectroscopy calibration (Gemini, 2016).

# 4

# Characterization of the Pre-transitional Disk for HD 179218

## 4.1 Introduction

Herbig stars are pre-main sequence stars with intermediate mass and mostly born in clouds (see chapter 2) while some of them are born in isolated dark clouds such as my target HD 179218 (Stahler and Palla, 2008). Herbig stars were discovered by the astronomer George Herbig in 1920. Their mass is between (2 M$_\odot$ - 8 M$_\odot$), the luminosities between (10 - 10$^3$ L$_\odot$) and the temperature ranges between (8000 - 20000 K). Herbig stars are located in the Hertzsprung-Russell (HR) diagram in the cross section of the birth line and the ZAMS (LeBlanc, 2011).

In the last few years, many Herbig stars have been observed using numerous telescopes and techniques. This led to an increase in the number of the Herbig / Group Ib stars which have detected a gap in their disk such as HD 100546 (Bouwman *et al.*, 2003), HD 142527 (Fukagawa *et al.*, 2006), Oph IRS 48 (Geers *et al.*, 2007), HD 179218 Fedele *et al.* (2008), HD 135344 (Brown *et al.*, 2009), AB Aur (Honda *et al.*, 2010), HD 169142 (Honda *et al.*, 2012), HD 139614 (Matter *et al.*, 2016).

Protoplanetary disks with gaps are known as "Transitional Disks". There are different explanations for these transitional disks depending on different processes such as the accretion of the dust onto the star, photoevaporation and planet formation. Mostly, gaps are created in different locations in the disk which may take place in the inner or outer region of the disk. These gaps are optically thin as a result of the absence of dust

# 4. CHARACTERIZATION OF THE PRE-TRANSITIONAL DISK FOR HD 179218

particles which leaves only gas in this region. In contrast, other regions are filled with dust grains and are optically thick.

This depletion of the dust particles as well as gaps are related to planet formation, consequently, transitional disks have become very interesting for astronomers. Recently, several studies have made use of high-angular resolution and high sensitivity spectroscopy to obtain more information about the structure of transitional disks from the abundance of the silicate emission as well as PAH neutral and ionized emission in the infrared bands (Calvet *et al.*, 2002; Espaillat *et al.*, 2014; Fukagawa *et al.*, 2010; Furlan *et al.*, 2006).

Modelling the SED is not sufficient to see the whole picture and can not answer all questions about the protoplanetary evolution. SED modelling alone cannot be able to locate gaps and reveal the whole structure of the protoplanetary disk, such as in Acke *et al.* (2009); Isella *et al.* (2009). Therefore, many researchers have used high angular resolution imaging by using the largest telescopes and interferometers in the MIR to constrain the geometry of the disk and to resolve the compact disk structure for T Tauri and Herbig AeBe stars (Gräfe *et al.*, 2011; Mariñas *et al.*, 2011).

In this project, I concentrate on the MIR emission in the PAH and silicate bands for the protoplanetary disk of the young stellar object HD 179218. The observation is achieved using high angular resolution with the GTC / CanariCam in the N band. The PAHs can be excited by the direct UV radiation coming from the star and can be traced in the outer region of the disk such as in HD 97048 (Doucet *et al.*, 2006; Lagage *et al.*, 2006). In other cases, the PAHs can be used to resolve some of the most important questions in Herbig stars, e.g if there is any connection between Group I and Group II disks. Also, PAH can be used to determine the size of the gaps from tracing their emission in the surface of the disk (Maaskant *et al.*, 2014).

My study is focusing on the geometry of the Herbig star HD 179218 by observing it with the PAH and continuum filters. The disk is resolved in the PAH emission without silicate emission and then I calculate the diameter of the disk. The geometry of the disk has been constructed using radiative transfer modelling (RADMC3D) to build the spectral energy distribution and images for the protoplanetary disk in three filters to fit them with GTC observations.

In section 4.2, I introduce the properties and historical observations of HD 179218. In section 4.3, I describe the observation of HD 179218 with the GTC telescope / CanariCam instrument in three filters (8.6, 11.3 and 12.5 $\mu m$) and then explain how

I have reduced the MIR data. After that, in section 4.4 and 4.5, I describe statistical measurements for the FWHM and radial profiles of images in three filters for my source HD 179218 and two calibration stars HD 169414 and HD 187642.

In section 4.6, I calculate the photometry of HD 179218 after calibrating it with two calibration stars. In addition, I have reduced the spectrum of HD 179218 using the RedCan pipeline and then compared the spectrum that I have obtained with Spitzer and Infrared Space Observatory (ISO) spectrum for the same source.

In sections 4.7 and 4.8, I have used one of the radiative transfer codes, RADMC3D, to build a model of the protoplanetary disk for HD 179218 and then I have fitted the two models of the SED with observational SED. Furthermore, the physical properties of the pre-transitional disk for HD 179218 have been extracted such as size, mass, and flaring for the inner disk, gap, and outer disk.

In section 4.9, the images of the best model are convolved with the PSF of two calibrations stars at three wavelengths 8.6 $\mu m$, 11.3 $\mu m$, and 12.5 $\mu m$. The radial profile of the images is plotted and compared with radial profiles of observational images in PAH filters and Silicate filter.

In section 4.10 and 4.11, I compare the PAH emission in the HD 179218 with the two other Herbig stars HD 97048 and IRS 48. I have also discussed the origin of the PAH emission (inner disk vs. outer disk) and the charge state of the PAH emission (ionized vs. neutral) in the surface of the pre-transitional disk.

## 4.2   HD 179218 Target

The target HD 179218 (also, known as MWC 614) is classified as a Herbig Ae/Be star by The *et al.* (1994) and as Group Ia by Meeus *et al.* (2001). HD 179218 coordinates in the sky are $\alpha$ = 19h 11m 11.25s $\delta$ = +15°:47′:15.63″ and the other physical properties of the star are listed in Table 4.11.

HD 179218 has been studied before by Meeus *et al.* (2001); Acke and van den Ancker (2004); Dullemond and Dominik (2004a) by analyzing the SED from the ISO archive. They conclude that HD 179218 has a very strong IR emission due to the circumstellar dust and has a flaring disk with silicate and PAH emission. It is classified according to these properties as Herbig / Group Ia which has a flaring disk and silicate emission in the spectrum.

## 4. CHARACTERIZATION OF THE PRE-TRANSITIONAL DISK FOR HD 179218

Leinert *et al.* (2004) have used the Very Large Telescope Interferometer (VLTI) for IR observation at 10 *μm* to study HD 179218 and resolve the disk size between (1 AU - 10 AU). Monnier *et al.* (2006) observed the same target with interferometry techniques using the Mount Hopkins telescope in NIR at 1.65 *μm* and measured the diameter of the disk to be 3.1 AU.

Fedele *et al.* (2008) have observed HD 179218 using the VLTI telescope in the N-Band through interferometry techniques and high resolution spectroscopy at the [OI] 6300 Å. He concluded that HD 179218 could be a transitional disk with two disks and a gap. Where the inner disk size is between (0.3 AU - 3.2 AU), the outer disk size is between (15 AU - 23 AU) and the gap extends between (3 AU - 15 AU).

Transitional disks can be considered as a class of protoplanetary disk which have an inner region with lack of dust grains. Recently, these disks have been very important to study, because the depletion of dust grains or gaps in this region may be related to ongoing planet formation. The scheme below shows the diagram of the structure of the inner and outer disk for the HD 179218 model.
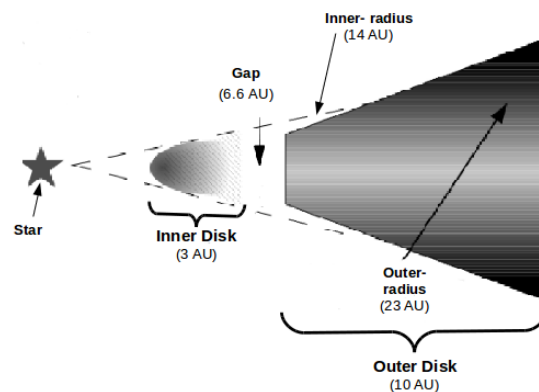


**Figure 4.1:** Scheme for the HD 179218 protoplanetary disk by Fedele *et al.* (2008) shows two components disk and a gap or shadow region between them.

Mariñas *et al.* (2011) used the Gemini North and T-ReCS on Gemini South to get high angular resolution imaging for HD 179218 at 12 *μm* and 18 *μm*. They could not resolve the disk at 18 *μm* and 11.7 *μm*. Recently, Honda *et al.* (2015) used Subaru/COMICS and the Gemini telescopes to observe HD 179218 in the MIR at wavelength 25 *μm*. They found no silicate emission from the the disk at this wavelength and could not resolve the disk. Table 4.1 shows historical observations for the HD 179218.

| Telescope | Diameter or Baseline [m] | $\lambda$ [$\mu m$] | FWHM ['']| Disk Size [AU] | References |
|-----------|------------------------|---------------------|----------|----------------|------------|
| VLTI/MIDI | 59.7-86.0 | 12.5 | 0.034 | 8 | (1) |
| MMT | 6.5 | 10.6 | 0.082 | 20 | (2) |
| VLTI/MIDI | 58,48, 53,44 | 10.3 | 0.038-0.049 | 9-12 | (3) |
| Subaru/CIAO | 8.2 | 1.65 | - | unresolved | (4) |
| Gemini-N,S | 8.1 | 11.7,18.3 | - | unresolved | (5) |
| Subaru/COMICS | 8.2 | 25 | - | unresolved | (6) |
| GTC/CanariCam | 9.5 | 8.6, 11.3 | 0.092, 0.084 | 27-24 | (7) |

**Table 4.1:** Summery of previous observations for HD 179218 using different wavelengths and different ground-based telescopes.
(1) Leinert *et al.* (2004), (2) Liu *et al.* (2007), (3) Fedele *et al.* (2008), (4) Fukagawa *et al.* (2010), (5) Mariñas *et al.* (2011), (6) Honda *et al.* (2015), (7) This work results.

## 4.3   Observation and Data Reduction

HD 179218 was observed using the GTC telescope / CanariCam instrument in MIR filters PAH1 (8.6 $\mu m$, $\Delta\lambda$ = 0.43 $\mu m$), PAH2 (11.3 $\mu m$, $\Delta\lambda$ = 0.60 $\mu m$) and Silicate Si6 (12.5 $\mu m$, $\Delta\lambda$ = 0.70 $\mu m$). CanariCam has a Raytheon 320×240 Si:As detector that covers a field of view of 26''x19''. The plate scale of the CanariCam detector is 0.08''/pixel. The chopping throw was 8'' and the position angle of the chopping was 90 degrees. The final image which is acquired after data reduction consists of one central positive image of the object surrounded by two negative images. The observation sequence is performed by observing the PSF of two different calibration stars, before and after the science target. The two calibration stars HD 169414 and HD 187642 are observed in the three filters (PAH1, PAH2, Si6) and used for the PSF, photometric, and spectroscopic calibration. The mean of the optical seeing for the observation days are extracted from the Differential Image Motion Monitor (DIMM) measurement [1]. Seeing values were excellent during 8th of June 2015 with a range from 0.42'' to 0.6''. For 15th of September the seeing was not good for the first calibrator star (1'') in comparison to the science target and another following calibration star was observed during a much better seeing conditions.

---

[1]http://www.not.iac.es/weather/dimm_index

# 4. CHARACTERIZATION OF THE PRE-TRANSITIONAL DISK FOR HD 179218

The PWV can be considered as good for N band observations. Here, values are extracted between 7 mm to 8 mm for both days. The low-resolution spectroscopic observations were achieved on the 2$^{nd}$ of July 2015 under good weather conditions with a seeing of 0.8″ and a PWV of 10 mm. The spectroscopy of the science target is calibrated with two different Cohen standard stars, which were observed before and after the science target. The total integration time and more details about the observation for the calibration stars (HD 169414, HD 187642) and the science star (HD 179218) are summarized in Table 4.2.

**Table 4.2:** Observing log. for the science target and for the two calibration stars in the PAH1, PAH2 and Si6 filters.

| Object | Date | Filter | Integ. Time [Sec] | Airmass | Seeing[ ″ ] | Flux |
|--------|------|--------|-------------------|---------|-------------|------|
| HD 169414 | 08/06/2015 | PAH1 | 397.145 | 1.04 | 0.60 | Calibrator star |
| HD 179218 | 08/06/2015 | PAH1 | 1853.343 | 1.06 | 0.42±0.03 | Science |
| HD 187642 | 08/06/2015 | PAH1 | 397.145 | 1.17 | 0.55 | Calibrator star |
| HD 169414 | 08/06/2015 | PAH2 | 417 | 7.7 | 0.51 | Calibrator star |
| HD 179218 | 08/06/2015 | PAH2 | 1807 | 8.1 | 0.45±0.02 | Science |
| HD 187642 | 08/06/2015 | PAH2 | 417 | 7.0 | 0.58 | Calibrator star |
| HD 169414 | 15/06/2015 | Si6 | 397.145 | 1.03 | 1 | Calibrator star |
| HD 179218 | 15/06/2015 | Si6 | 1853.343 | 1.08 | 0.6±0.03 | Science |
| HD 187642 | 15/06/2015 | Si6 | 397.145 | 1.11 | 0.5 | Calibrator star |
| HD 169414 | 02/07/2015 | LR-Spec. | 176.85 | 1.0 | 0.85 | Telluric Calibrator |
| HD 179218 | 02/07/2015 | LR-Spec. | 943.22 | 1.02 | 0.77 | Science |
| HD 187642 | 02/07/2015 | LR-Spec. | 176.85 | 1.06 | 0.80 | Telluric Calibrator |

I have used the iDealCam software (Li, 2014) for the data reduction. It was designed to deal with images from CanariCam instrument and to reduce the thermal background effects. The iDealCam is able to display the individual frames called "saveset" or stacking frames called "nodsets". Each nodset is composed of stacking eight savesets with integration times of 16 s for each nodset which is useful to observe the fainter object. The saveset duration of ∼ 2 s is the same for the science and calibration targets. The nodset or saveset can be realigned along their centroid through a two-dimensional Lorentzian fit of the PSF prior to the final shift-and-add stacking.

Despite observing in the MIR range with a good ~ 0.5″ - 0.6″ average seeing, the atmospheric turbulence above a 10 m class telescope still degrades the image quality, resulting in a non-fully diffraction-limited PSF. Depending on the instantaneous strength of turbulence, the image quality of the individual savesets can be significantly affected, which appears in the form of a distorted and elongated PSF.

## 4.4 Statistics of the Full Width at Half Maximum

I have fitted the PSF of calibration and science stars by using Lorentzian fitting for each individual saveset. There are three reasons for making a Lorentzian fit to every saveset instead of nodset. The first reason is to reduce the error which comes from the centring of eight savesets which is equivalent to one nodset. The second reason is the error that can occur from an inaccuracy in position between nods switch (telescope motion). The third reason is that the integration time of the saveset for calibration star and science target are equal.

The quality of the image depend on the shape of the PSF (circular shape) which is distorted and elongated because of the atmospheric turbulence. Therefore, I discard bad frames from the data by selecting "good" and "bad" frames in the data using visual inspection. Furthermore, I have discarded some of the savesets which have values less than the diffraction limit of the telescope as shown in Figure 4.2.

Three plots in the left of Figure 4.2 show the distribution of the FWHM for all saveset calibrator-science-calibrator observations in three filters (PAH1, PAH2 and Si6). The three plots on the right show the FWHM distribution after removing the bad frames and the frames with a FWHM lower than the theoretical diffraction limit of the telescope.

The blue open triangles show the FWHM for the individual savesets of the two calibration stars HD 169414 and HD 187642, respectively. The red open circles show the FWHM for individual saveset of the science star HD 179218. The black dashed line shows the theoretical diffraction limit of the GTC telescope in three filters. The diffraction limit of the GTC telescope in the three filters PAH1, PAH2 and Si6 are 0.19″, 0.25″ and 0.27″, respectively. The Si6 filter for the first calibration star HD 169414 shows unstable measurements for the FWHM during the observation as result of the poor seeing.

# 4. CHARACTERIZATION OF THE PRE-TRANSITIONAL DISK FOR HD 179218
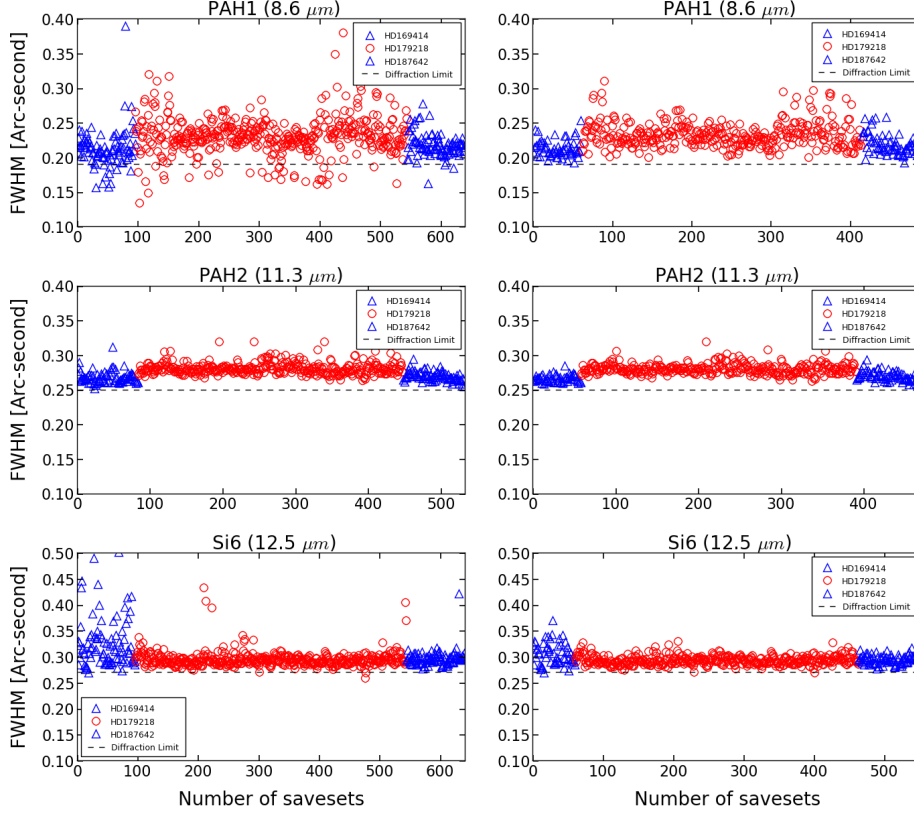


**Figure 4.2:** Illustrates the FWHM changing with time for each saveset before and after selecting a good savesets in the three filters PAH1, PAH2 and Si6.

The plot for PAH at 8.6 $\mu m$ and 11.3 $\mu m$ shows that the FWHM distribution for the science star HD 179218 is on average higher than the level of distribution of the two calibrators stars. As a result of the poor seeing for the first calibrator in the Si6 filter at 12.5 $\mu m$, the FWHM measurements have been cancelled from my calculation. The remaining second calibrator in the Si6 filter has the same value for FWHM as the science target.

The mean values of the FWHM measurement and $3\sigma$ uncertainty have been extracted from the saveset distribution for the science and two calibrator stars in the three filters, as shown in Table 4.3. The uncertainty of the FWHM measurements can be estimated by calculating the standard deviation of the mean value divided by the square root of the number of the selected savesets. This means that more than 99.7 % of FWHM of the science star is larger than the FWHM of the two other calibration stars in the PAH (8.6 $\mu m$, 11.3 $\mu m$) filters. While, the 99.7 % of the FWHM measurements

54

for the science are similar to the FWHM measurements for the second calibrator in the Si6 filter. The FWHM measurements of the first calibrator are neglected because of bad seeing.

| Object | Filter | On source [s] | Percentage [%] | FWHM$_L$ [$''$] $\pm 3\sigma$ |
|--------|--------|---------------|----------------|------------------------------|
| HD 169414 | PAH1 | 273 | 69 | 0.213 ± 0.004 |
| HD 179218 | PAH1 | 1501 | 81 | 0.232 ± 0.003 |
| HD 187642 | PAH1 | 314 | 79 | 0.217 ± 0.004 |
| HD 169414 | PAH2 | 287 | 70 | 0.267 ± 0.002 |
| HD 179218 | PAH2 | 1651 | 91 | 0.280 ± 0.001 |
| HD 187642 | PAH2 | 382 | 91 | 0.268 ± 0.002 |
| HD 169414 | Si6 | 397 | – | – |
| HD 179218 | Si6 | 1667 | 90 | 0.293 ± 0.001 |
| HD 187642 | Si6 | 364 | 91 | 0.294 ± 0.002 |

**Table 4.3:** shows the mean of the FWHM$_L$ and $3\sigma$ uncertainty which is calculated from the distribution of the savesets in three filters for calibration and science stars. The $L$ symbols refer to the FWHM measurements that are extracted from the Lorentzian fit.

The size of the disk for HD 179218 can be measured by following the same procedure which was used by Moerchen *et al.* (2007) to resolve the emission around main sequence stars. The criteria for resolving the disk is given by the difference between the FWHM of the science and the FWHM of the calibrator as described in this equation Moerchen *et al.* (2007):

$$\text{FWHM}_{\text{sci}} - \text{FWHM}_{\text{cal}} \geq 3\sigma_{\text{ext}} \tag{4.1}$$

where FWHM$_{\text{sci}}$ is the mean of the FWHM measurements for the selected saveset of the science star and FWHM$_{\text{cal}}$ is the mean of the FWHM measurements for these-lected saveset of the calibration stars. $\sigma_{\text{ext}}$ is the combined standard deviation of the mean and given by Moerchen *et al.* (2007):

$$\sigma_{\text{ext}} = \sqrt{\sigma_{\text{sci}}^2 + \sigma_{\text{cal}}^2} \tag{4.2}$$

where $\sigma_{\text{sci}}^2$ is the standard deviation of the mean of the FWHM measurements of the science star and $\sigma_{\text{cal}}^2$ is the standard deviation of the mean of the FWHM measurements of the calibration star.

## 4. CHARACTERIZATION OF THE PRE-TRANSITIONAL DISK FOR HD 179218

This criterion have applied with two calibration and science stars in the PAH filter at two wavelengths and the criterion applied with one calibration and science star in the silicate filter, the observations of first calibration star in the silicate filter are discarded because of the bad seeing. Table 4.4 shows the results of this criteria and that I have resolved the disk emission around HD 179218 in the PAH filters at two wavelengths and the disk emission is unresolved in the silicate filter.

| Object | Filter | $[\text{FWHM}_{\text{sci}} - \text{FWHM}_{\text{cal}}]_L \geq 3\sigma_{\text{ext}}$ | Resolved |
|--------|--------|:---:|:---:|
| *Savesets selection* | | | |
| Cal-1 | PAH1 | $0.019 \geq 0.006$ | Y |
| Cal-2 | PAH1 | $0.016 \geq 0.006$ | Y |
| Cal-1 | PAH2 | $0.013 \geq 0.002$ | Y |
| Cal-2 | PAH2 | $0.011 \geq 0.002$ | Y |
| Cal-2 | Si6 | $0.002 = 0.002$ | N |

**Table 4.4:** Resolution criterion for HD 179218 compared to the adjacent calibrators following Moerchen *et al.* (2010). The column (2) shows the result after applying the criteria with the term for Lorenztian fit being ($\text{FWHM}_L$) with 3 sigma uncertainty.

The diameter of the disk is measured by taking the quadratic subtraction of the mean FWHM of the science target from the mean FWHM of the calibration stars as described in the following equation:

$$D_{\text{Disk}} = \sqrt{\text{FWHM}_{\text{sci}}^2 - \text{FWHM}_{\text{cal}}^2} \qquad (4.3)$$

where $D_{\text{Disk}}$ is the diameter of the disk.

The diameter of the disk in the PAH filters is calculated by taking that the distance of the star is 290 pc from GAIA parallax measurements Gaia (2016) and reported in Table 4.5. The table shows the estimated radius of the disk emission in two PAH filters and it is between 12 - 15 AU.

The uncertainty of the emission diameter refers to the $1\sigma$ error in the diameter which estimated using this formula (Mariñas *et al.*, 2011):

$$\sigma = \frac{\sqrt{(\text{FWHM}_{\text{sci}} \times \sigma_{\text{sci}})^2 + (\text{FWHM}_{\text{cal}} \times \sigma_{\text{cal}})^2}}{D_{\text{Disk}}} \qquad (4.4)$$

| Object | Filter | D $_{Disk}$ $['']_L$ | Disk $_{radius}[AU]_L$ |
|--------|--------|----------------------|------------------------|
| HD 169414 | PAH1 | 0.092 ± 0.004 | 13.5 |
| HD 187642 | PAH1 | 0.082 ± 0.005 | 12.0 |
| HD 169414 | PAH2 | 0.084 ± 0.003 | 12.3 |
| HD 187642 | PAH2 | 0.081 ± 0.002 | 11.9 |
| HD 187642 | Si6 | 0.024 ± 0.009 | – |

**Table 4.5:** The diameter of the disk emission around HD 179218 and the radius of the disk are extracted in three filters as shown in table. The error of the diameter is estimated for $1\sigma$ using equation 4.4. The $L$ symbols refer to the FWHM measurements that are extracted from the Lorentzian fit.

## 4.5   Centering the images and a cumulative of the PSF

The final image for the science and calibration stars can be obtained after aligning each saveset and stacking them. The saveset alignment or re-centring is a very important process to get a good final image before stacking. The main purpose of the re-centring is to avoid an increase of the final FWHM due to the long observing time. A very simple re-centring step is depending on matching the centre of the saveset with other saveset centre. This produces an increase of the FWHM in the final image.

Therefore, the centering of the images is improved through re-alignment of each saveset by minimizing the difference between the core of each normalized PSF and the core of the initial calibration saveset. This method of re-centring is performed with an accuracy of one tenth of a pixel and leads to a better result in the FWHM of the final PSF.

Table 4.6 shows values of the FWHM$_P$ of the final image after re-centering and stacking all good savesets. The FWHM$_P$ values of the final image in the three filters are extracted from the radial profile plot and these values of the FWHM$_P$ are comparable with the FWHM$_L$ values in Table 4.3.

## 4. CHARACTERIZATION OF THE PRE-TRANSITIONAL DISK FOR HD 179218

| Object | Filter | On source [s] | Percentage [%] | FWHM$_P$ [''] ± 3$\sigma$ |
|---|---|---|---|---|
| HD 169414 | PAH1 | 273 | 69 | 0.233 ± 0.003 |
| HD 179218 | PAH1 | 1501 | 81 | 0.255 ± 0.002 |
| HD 187642 | PAH1 | 314 | 79 | 0.234 ± 0.003 |
| HD 169414 | PAH2 | 287 | 70 | 0.282 ± 0.002 |
| HD 179218 | PAH2 | 1651 | 91 | 0.298 ± 0.001 |
| HD 187642 | PAH2 | 382 | 91 | 0.285± 0.002 |
| HD 169414 | Si6 | 397 | – | – |
| HD 179218 | Si6 | 1667 | 90 | 0.313 ± 0.002 |
| HD 187642 | Si6 | 364 | 91 | 0.311 ± 0.003 |

**Table 4.6:** shows the mean of the FWHM$_P$ and 3$\sigma$ uncertainty which is extracted from the plot of the radial profile of the final image. The 3$\sigma$ uncertainty is calculated from the mean and error of the mean of the radial brightness profile for each saveset.

Using the same procedure that applied with FWHM$_L$ to resolve the disk and measure the size of the disk emission. Table 4.7 shows the result of the resolved disk emission in the PAH filters and unresolved emission in the silicate filter for the FWHM$_P$ measurements.

| Object | Filter | [FWHM$_{sci}$ - FWHM$_{cal}$]$_P$≥ 3$\sigma_{ext}$ | Resolved |
|---|---|---|---|
| *Savesets selection* | | | |
| Cal-1 | PAH1 | 0.022 ≥0.004 | Y |
| Cal-2 | PAH1 | 0.021 ≥0.004 | Y |
| Cal-1 | PAH2 | 0.016 ≥0.002 | Y |
| Cal-2 | PAH2 | 0.013 ≥0.002 | Y |
| Cal-2 | Si6 | 0.002 ≤0.004 | N |

**Table 4.7:** shows the resolve and unresolve emission around HD 179218 after centering all good savesets in three filters. The column (2) shows the result after applying the criteria, the term for the direct FWHM$_P$ extracted from the plot of the radial brightness profile is with 3 sigma uncertainty.

The results of the disk diameter for FWHM$_P$ measurements by using equation 4.3 are listed in Table 4.8.

| Object | Filter | D $_{\text{Disk}}$ $['']_P$ | Disk $_{\text{radius}}[\text{AU}]_p$ |
|--------|--------|------------|------------------|
| HD 169414 | PAH1 | 0.103 ± 0.003 | 15 |
| HD 187642 | PAH1 | 0.101 ± 0.003 | 15 |
| HD 169414 | PAH2 | 0.096 ± 0.002 | 14.1 |
| HD 187642 | PAH2 | 0.087 ± 0.002 | 12.8 |
| HD 187642 | Si6 | 0.053 ± 0.011 | – |

**Table 4.8:** shows the diameter of the disk emission around HD 179218 and the radius of the disk in three filters. The *L* symbols refer to the FWHM measurements that are extracted from the plot of the radial brightness profile. The error of the diameter is estimated for $1\sigma$ using equation 4.4.

Figure 4.3 demonstrates the advantage of the re-centering method and the cumulative FWHM of the stacked image is given as a function of the number of the co-added savesets. The plots show that the FWHM of the stacked image are comparatively the same to the statistical value in Table 4.3.

The final images are shown in Figure 4.4. The first two rows show the final images of the calibrator-science-calibrator stars in the PAH1 and PAH2 filters. The last row shows the final images for the science and second calibrator stars in the silicate filter. As described before, the first calibrator in the silicate filter was discarded due to bad seeing.
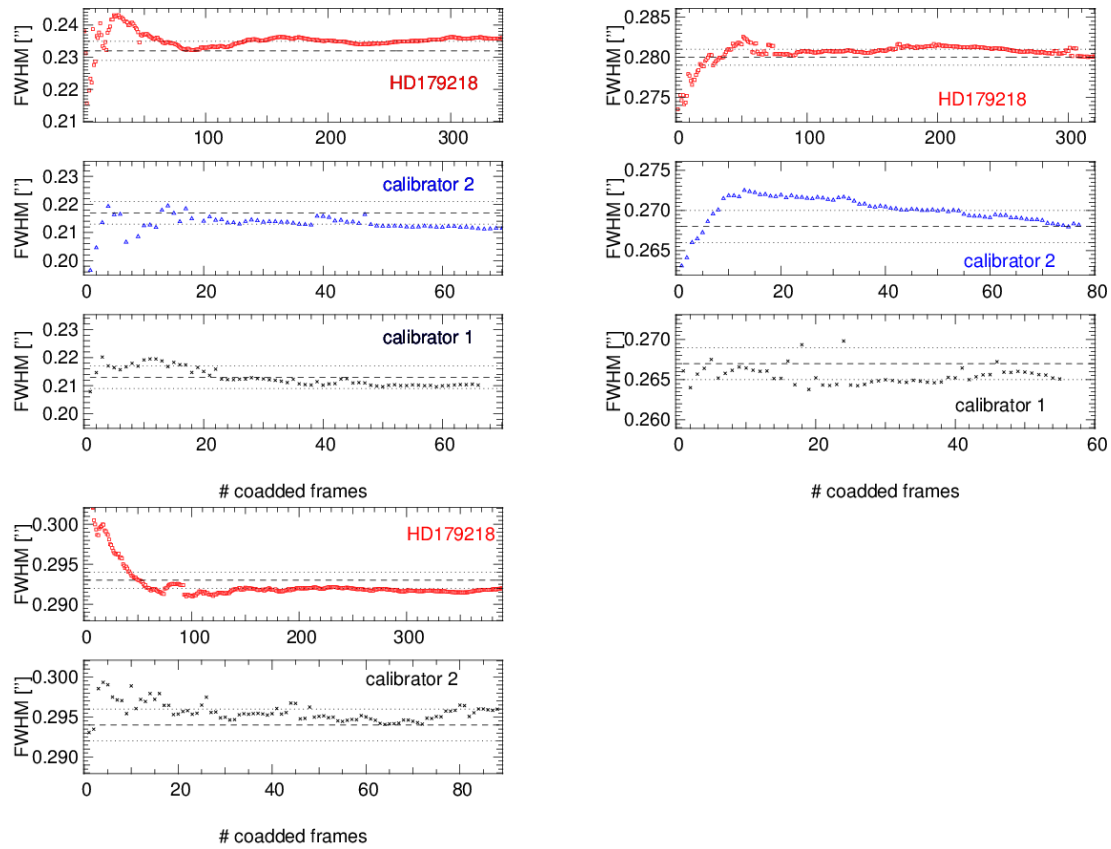
**Figure 4.3:** shows cumulative of the FWHM for both calibration stars (HD 169414 and HD 187642) and the science star (HD 179218) in PAH1, PAH2 and Si6 filters with the number of the co-added savesets. The bold dashed line is the average of the FWHM measurements and the dashed lines are the error bars of the average. The red circles represent the PSF of the science and the blue triangles are the PSF of the calibrators.
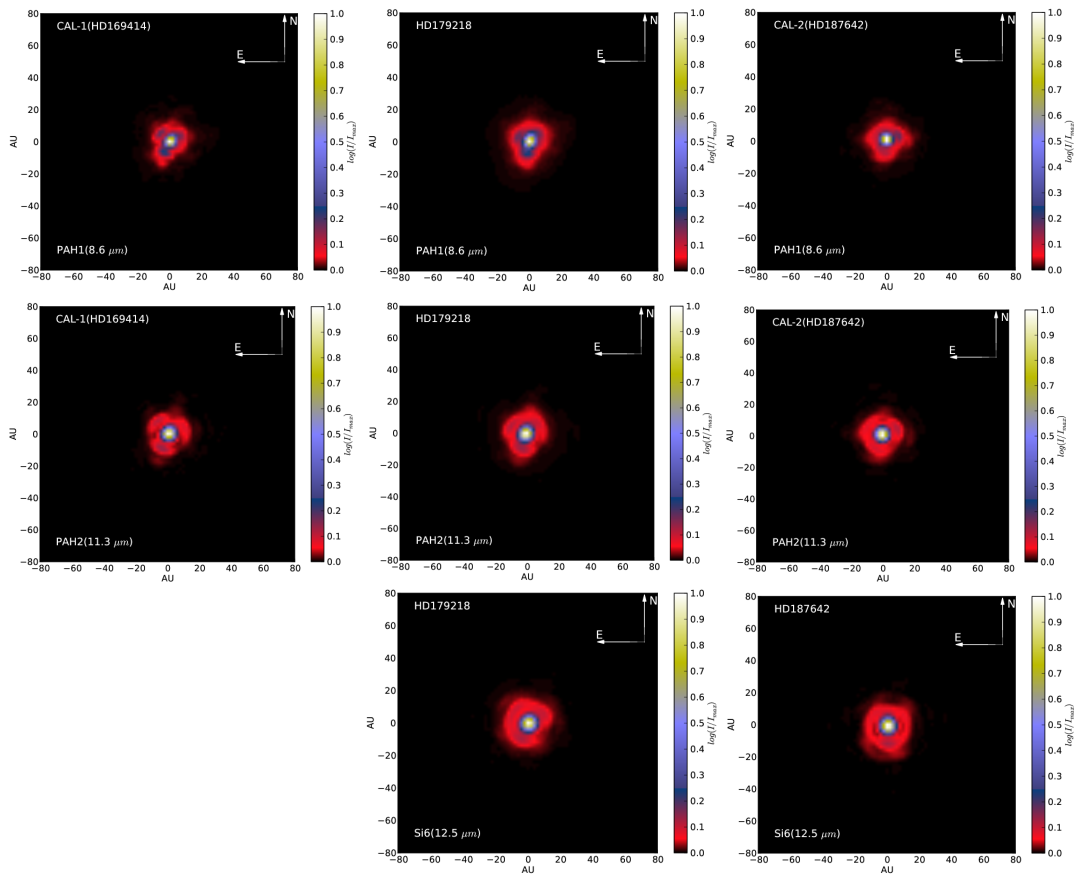
**Figure 4.4:** The final images of the science and calibration stars after shifting and adding good savesets.

The radial profile of the brightness distribution for the individual selected savesets have been plotted for science and calibrators in three filters after re-centering each saveset. I have extracted the mean value of the radial brightness profile for a good saveset and plotted with $3\sigma$ error bars, as shown in Figure 4.5.

The figure illustrates the profile of the science in red while the blue line is for the two calibrator profiles. It is obvious from the plot that the PAH emission is resolved at both wavelengths and with two calibrators stars. The plot also shows that the profile of the science matches the profile of the calibrator which means that there is no emission in the silicate features from HD 179218.
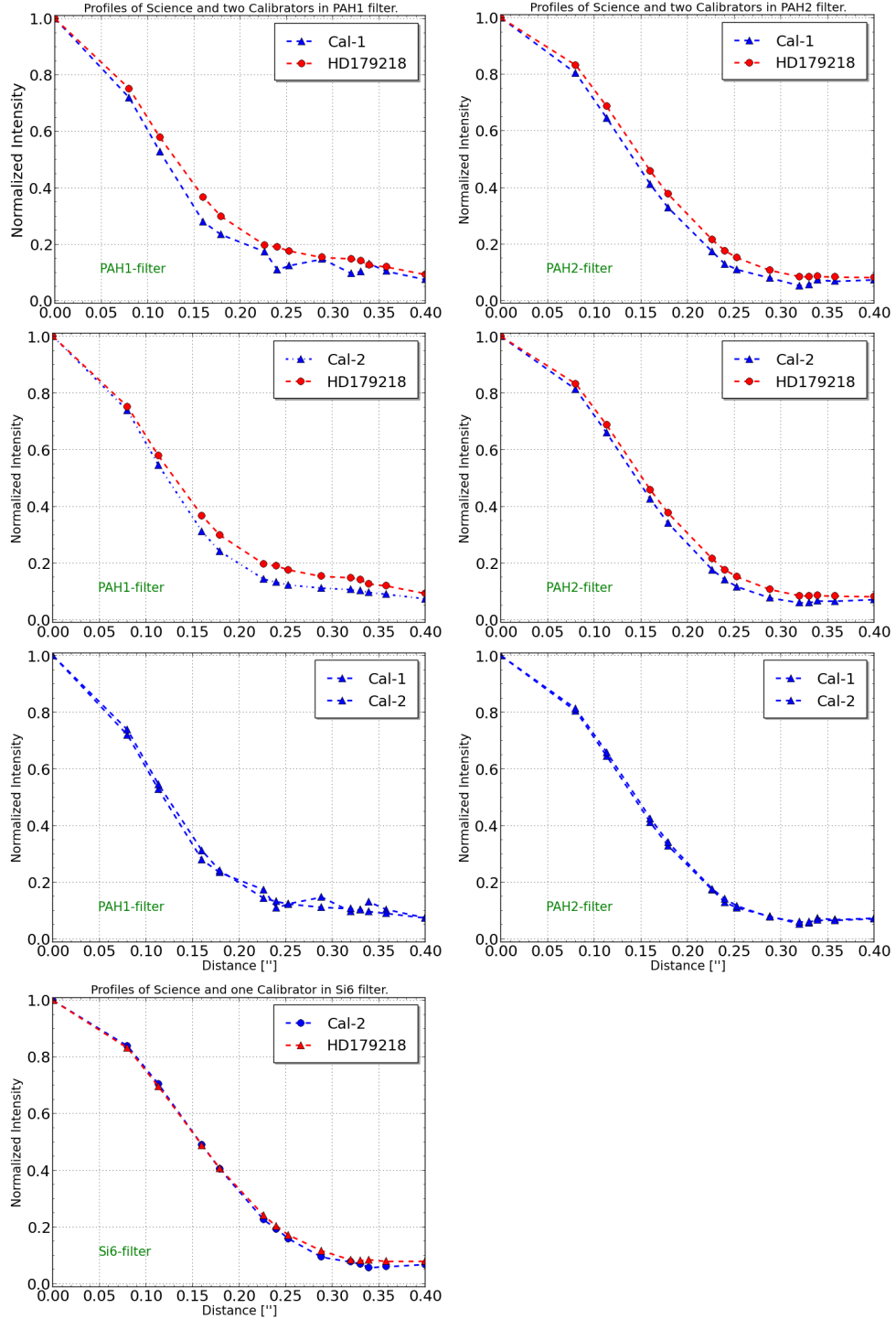
**Figure 4.5:** shows the radial brightness profiles for science and two calibrators stars in three filters. The flux is normalized to one and distances are given in arc-second.

## 4.6   Photometry and Spectroscopy of HD 179218

The first calibrator star was observed before the science target star and then followed by the second calibrator star for achieving the photometric calibration. I have used iDealCam software by Li *et al.* (2013) to obtain the photometric measurements of the science target HD 179218 and the other two calibrator stars HD 169414 and HD 187642. For including the background, I have applied a circular aperture of 20 pixels (1.6″) for the inner circle and 30 pixels (2.4″) for the outer aperture. The same values of the aperture radius have been applied for measuring the photometry of the two calibrator stars and the science target. The aperture of the flux area was chosen to be 4 times larger than FWHM of the PSF to include a possible circumstellar disk associated with the observed star. I demonstrate the stability of the measured flux through the whole period of observation for the three filters, as illustrated in Figure 4.6.

The flux values of the calibrator stars HD 169414 and HD 187642 were taken from the Cohen table for the standard stars [1]. The percentage of the flux variation during the observations for the calibration and science stars in three filters are estimated and listed in Table 4.9.

| Object | Stability percentage | Filters |
|--------|:--------------------:|---------|
| HD 169414 | 0.58% | PAH1 |
| HD 179218 | 0.60% | PAH1 |
| HD 187642 | 0.49% | PAH1 |
| HD 169414 | 0.97% | PAH2 |
| HD 179218 | 0.41% | PAH2 |
| HD 187642 | 0.59% | PAH2 |
| HD 169414 | 3% | Si6 |
| HD 179218 | 1.41% | Si6 |
| HD 187642 | 0.19% | Si6 |

**Table 4.9:** Percentage of flux stability for calibrator and science stars during observation.

In the PAH1 and Si6 filter the second calibrator star HD 187642 is more stable compared to the science object HD 179218 and the first calibrator star HD 169414. The change in the flux stability is caused by atmospheric or seeing changes during the

---

[1]`www.astro.ufl.edu/~dli/web/IDEALCAM_files/iDealCam_v2.0.zip`
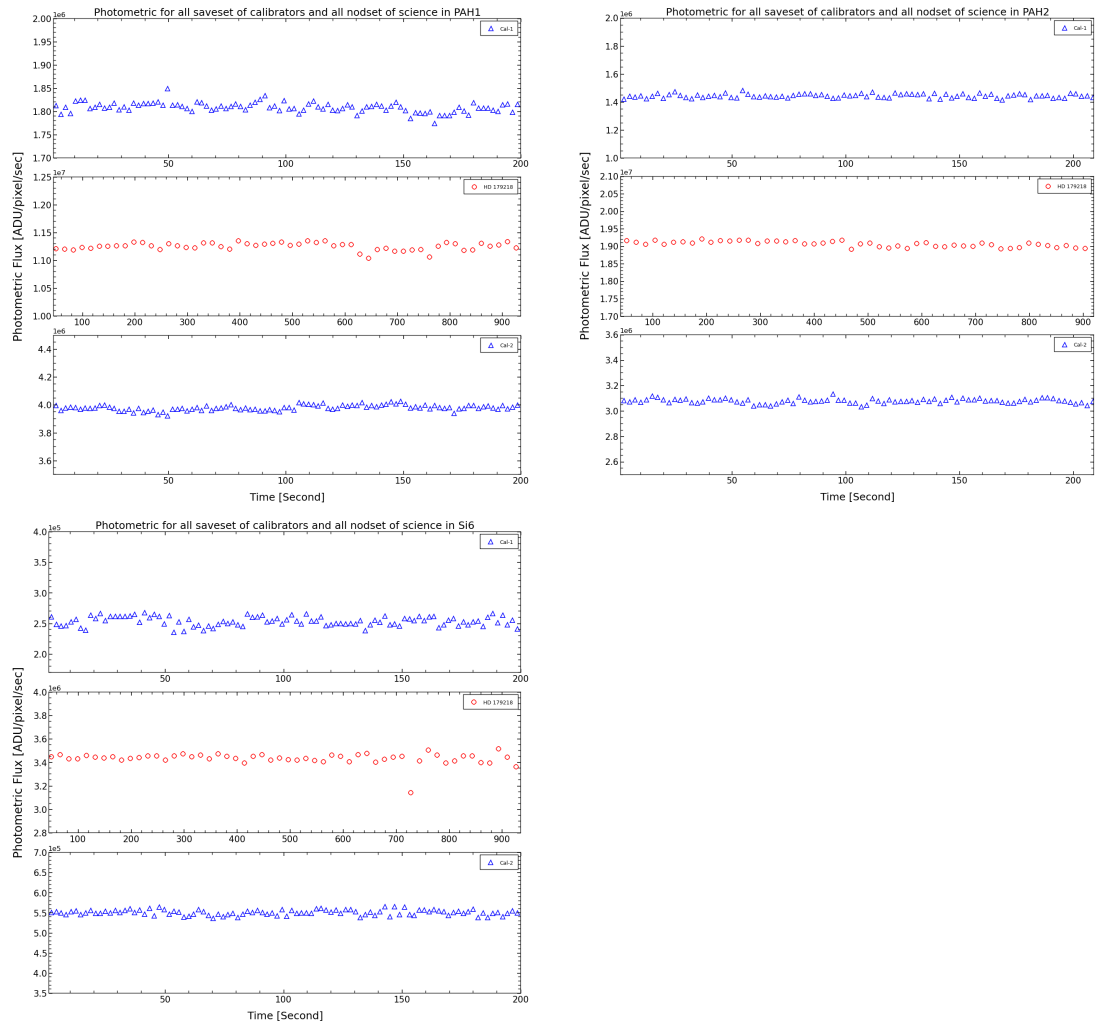
**Figure 4.6:** shows the stability of the flux for science and calibrator stars in three filters during the observation.

observation. The value of the flux fluctuation is less than 1.5 % for all observations. This result is a good measurement for the flux of star observed from a ground-based telescope. There is only one measurement with a flux fluctuation larger than 1.5 % which is for the first calibrator star in filter Si6 because of the poor seeing (> 1″). The flux density of HD 179218 has been extracted in three filters. I calibrated the science star with two different calibrator stars to get the value of the flux with error as shown in Table 4.10.

## 4. CHARACTERIZATION OF THE PRE-TRANSITIONAL DISK FOR HD 179218

| Calibration | Filters | Flux-science in [Jy] $\pm 3\sigma$ | Flux-Calibration in [Jy] |
|---|---|---|---|
| Cal1-HD 169414 | PAH1 | 14.88 ± 0.36 | 19.2 |
| Cal2-HD 187642 | PAH1 | 15.32 ± 0.36 | 43.3 |
| Cal1-HD 169414 | PAH2 | 22.43 ± 0.63 | 12.2 |
| Cal2-HD 187642 | PAH2 | 22.02 ± 0.42 | 25.4 |
| Cal1-HD 169414 | Si6 | 16.77 ± 1.65 | 9.9 |
| Cal2-HD 187642 | Si6 | 16.23 ± 0.69 | 20.8 |

**Table 4.10:** The flux of HD 179218 in the three filters after calibrating it with photometric standard stars in the first column with $3\sigma$ uncertainties. The large uncertainties in the flux of the first calibrator HD 169414 in the Si6 filter is due to bad seeing.

Spectroscopic measurements for HD 179218 have been obtained at low-angular resolution in the MIR using CanariCam on the GTC with long-slit spectroscopy. I have used a low spectral resolution 10 $\mu m$ grating, which covers the N-band~ 7.5 - 13 $\mu m$ with R=$\lambda/\Delta\lambda$ ~175 and a wide slit 0.36″. The observations were taken consequently for calibrator-science-calibrator stars using the standard MIR chop-nod technique on July 1, 2015, for HD 179218. The on-source integration times for the spectroscopy of the two calibration stars and for the science target are shown in Table 4.2. The data is reduced using the RedCan pipeline for the CanariCam instrument (Gonzlez-Martn, O. et al., 2013) that includes stacking of the individual observations, wavelength calibration, trace determination, spectral extraction, and flux calibration.

Figure 4.7 shows the spectrum of HD 179218 which has been rescaled to fit the spectrum of the same target HD 179218 from the Spitzer and ISO space telescopes (Acke and van den Ancker, 2004; Fedele et al., 2008). The rescaled spectrum of HD 179218 is also consonant with the photometric measurement values (green circles) in the three filters. The comparison of the spectra show a good agreement of the flux between Spitzer and GTC spectrum in the two filters 8.6 $\mu m$ and 12.5 $\mu m$, and slightly less agreement at 11.3 $\mu m$.

The ISO spectrum compared to the GTC spectrum shows better agreement in the whole spectrum except at 12.5 $\mu m$. The effect of the ozone feature of the atmosphere is very strong and obvious in the region between 9.3 - 9.9 $\mu m$. In addition to that, the flux of HD 179218, which is measured using CanariCam, shows that the flux between 9 and 9.2 $\mu m$ is larger by 10 to 20 % than the flux measured by ISO and Spitzer, respectively.
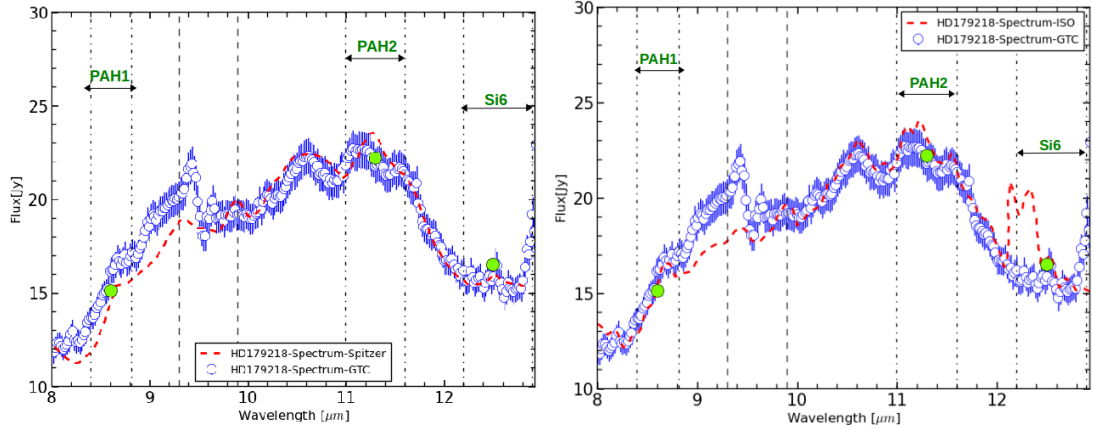
**Figure 4.7:** The low resolution spectrum of HD 179218 by CanariCam (blue open circles with error bars) and comparison with Spitzer and ISO spectrum (the red dashed line). The green filled circles represent the photometry measurements at PAH1, PAH2 and Si6. The vertical dotted lines represent the bandwidths of the three filters. The vertical dashed line indicates the region of the atmospheric ozone feature.

## 4.7 Radiative Transfer Model RADMC3D Code

A good observation is not enough to understand the protoplanetary disk, therefore, it is very necessary to support observations by a model to describe the geometry, structure, density distribution, and materials of the disk. The disk model can be used to explain the spectral energy distribution and images. Therefore, my main purpose is to reproduce the spectral energy distribution and the image in continuum emission for HD 179218 and fit it with my observation in the three filters (PAH1, PAH2, Si6).

I have used a radiative transfer model to construct the spectral energy distribution and the image at 12.5 $\mu m$ to convoloved with for HD 179218 by using RADMC3D software for integrating the radiative transfer equation along ray-tracing. RADMC3D is a software built by Dullemond and Dominik (2004b), see also (Dullemond, 2012) and has abilities to calculate the dust temperature and density of the protoplanetary disk in three dimensions assuming hydrostatic equilibrium by using Monte Carlo simulations (Bjorkman and Wood, 2001). The RADMC3D code has been applied successful in many other studies e.g Andrews *et al.* (2011); Matter *et al.* (2016); Pinte *et al.* (2009).

## 4. CHARACTERIZATION OF THE PRE-TRANSITIONAL DISK FOR HD 179218

The radiative transfer equation as it is in the code RADMC3D is described here in [1] as:

$$\frac{dI_v}{ds} = J_v^{therm} + J_v^{scat} - (\alpha_v^{abs} + \alpha_v^{scat})I_v \tag{4.5}$$

Where $J_v^{therm}$ is the thermal emission and given by:

$$J_v^{therm} = \alpha_v^{abs}B_v(T) \tag{4.6}$$

and $\alpha_v^{abs}$ is the extinction coefficient for absorption and $B_v(T)$ is the Planck function. The extinction coefficient for absorption, $\alpha_v^{abs}$, is estimated from the density distribution $\rho$ and the absorption opacity $\kappa_v^{abs}$ where:

$$\alpha_v^{abs} \equiv \rho\kappa_v^{abs} \tag{4.7}$$

The scattering of light is included in the calculation of the RADMC3D code and I have selected the simple method of isotropic scattering (scattering-mode = 1). The mean intensity of the scattering $J_v^{scat}$ is given by:

$$J_v^{scat} = \alpha_v^{scat}\frac{1}{4\pi} \int I_v \mathrm{d}\Omega \tag{4.8}$$

where $\Omega$ is the solid angle, $\alpha_v^{scat}$ is the extinction coefficient for scattering and it is estimated from the density distribution $\rho$ and scattering opacity $\kappa_v^{scat}$ where:

$$\alpha_v^{scat} \equiv \rho\kappa_v^{scat} \tag{4.9}$$

The model of the spectrum and the image of the protoplanetary disk for HD 179218 are created using RADMC3D. The disk for HD 179218 is described as a passive flared disk based on the model with a gap between the inner and the outer disk (Fedele *et al.*, 2008). I have considered the disk coordinates as polar coordinates which consist of the radial grid (r) and angular grid ($\theta$).

---

[1] http://www.ita.uni-heidelberg.de/~dullemond/software/radmc-3d/radmc-3d_v0.41.pdf

The dust density distribution in the disk is assumed to be in hydrostatic equilibrium similar to the gas density distribution and is described in this equation:

$$\rho(r) = \frac{\Sigma(r)}{H(r)\sqrt{2\pi}}\exp\left(\frac{-z^2}{2H^2(r)}\right) \tag{4.10}$$

where $z \simeq (\frac{\pi}{2} - \theta)r$ is the vertical height in the disk. For the geometrical thin disk $z \gg r$. $H(r)$ is the scale height of the disk and can be used to characterize the disk flaring by the flaring exponent $\beta$ as described by:

$$H(r) = H_o\left(\frac{r}{r_o}\right)^{1+\beta} \tag{4.11}$$

where $H_o = H(r_o)$ is the initial point for the scale height and can be chosen randomly with $r_o$ which represents the initial point for the radius of the disk. $\beta$ is the flaring component. The profile of the density distribution $\Sigma(r)$ as a function of the disk radius is calculated from the equation:

$$\Sigma(r) = \Sigma_0\left(\frac{r}{r_o}\right)^{p} \tag{4.12}$$

$\Sigma_0$ is the initial surface density of the disk in $g/cm^2$ at the radius ($r_o$), $r$ is the radius of the disk in AU and p is the power law of the surface density (Dullemond and Dominik, 2004b). $\Sigma_0$ can be added directly to the code by the user or can be calculated from the mass of the disk ($m_{disk} = m_{dust} + m_{gas}$) and in my calculation I have used the mass of the disk.

The size of the dust grains is adopted according to the power law distribution of the grain size between $a_{min}$ and $a_{max}$ by using the equation:

$$n(a) \, \alpha \, a^{-3.5} \tag{4.13}$$

The power law index -3.5 is the same as the distribution of sizes in the interstellar medium (Mathis *et al.*, 1977).
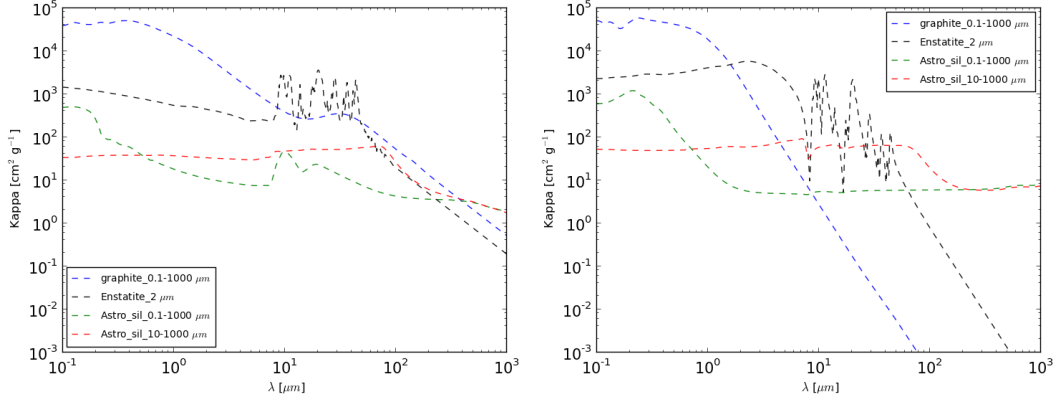
**Figure 4.8:** The left plot is the absorption cross section per unit of mass for graphite, crystalline enstatite and silicate. The right plot is the scattering cross section per unit of mass for graphite, crystalline enstatite and silicate.

I have chosen a mix of dust grains in the disk such as graphite and silicate in the inner disk, gap and mid-plane. The graphite has been used in the different models and considered as an important feature to fit the observation (Carmona *et al.*, 2014; Matter *et al.*, 2016; Meeus *et al.*, 2002). For the outer component, I have used the crystalline enstatite and silicate grains the model of (Juhász *et al.*, 2010).

Figure 4.8 shows the optical properties of materials that have been used in the disk. The size of the grains for the crystalline enstatite is selected to be 2 *μm* in the outer disk. The size of the silicate and graphite grains is between a minimum size of 0.1 *μm* and a maximum size of 1000 *μm* in the inner disk, gap and outer disk while in the mid-plane the grain size for silicate is chosen between 10 *μm* and 1000 *μm* since it is known that the large grains are located in the mid-plane of the protoplanetary disk (Williams and Cieza, 2011).

## 4.7.1 Stellar Parameters

The stellar spectrum is modelled by a Kurucz model with stellar inputs chosen for HD 179218 from two different references to compare between two models. The input stellar parameters such as the mass, temperature, and radius are taken from two different references. The input stellar parameters for the model-1 are extracted from Alecian *et al.* (2013) and the input parameters for model-2 are extracted from Dominik *et al.* (2003). Two different stellar parameters of HD 179218 are used to create the

**Table 4.11:** Stellar parameters for HD 179218 used to fit two models of the disk.

| Parameters | Model-1[1] | Model-2[2] |
|---|---|---|
| Stellar spectral Type | B9e [1] | B9e [1] |
| Stellar temperature | 9640 K [1] | 10000 K [2] |
| Stellar mass | 3.66 $M_\odot^{(1)}$ | 2.70 $M_\odot^{(2)}$ |
| Stellar radius | 4.8 $R_\odot^{(1)}$ | 3 $R_\odot^{(2)}$ |
| Stellar age | 1.08 Myrs [1] | 1.08 Myrs [1] |
| Stellar luminosity | 181 $L_\odot^{(1)}$ | 80 $L_\odot^{(2)}$ |
| Distance | 290[3] | 290[3] |
| Position Angle | 23 ° [4] | 23 ° [4] |
| Inclination | 57 ° [2,5] | 57 ° [2,5] |

(1) Alecian *et al.* (2013),(2) Dominik *et al.* (2003) (3) Gaia (2016),
(4) Fedele *et al.* (2008), (5) Dominik *et al.* (2003)

SED model and the radial brightness profile of the image model at 12.5 $\mu m$ then fit them with observational SED and the radial profile of the image at 12.5 $\mu m$ which is unresolved. The two different stellar parameters are listed in Table 4.11.

The observational SED of the HD 179218 is taken from (Acke and van den Ancker, 2004) and the star distance is extracted from the GAIA space telescope (293 pc) Gaia (2016).

The interstellar extinction is another important factor that should be considered for fitting the SED. The extinction is described by the absorption and the scattering of the light by dust and gas particles. The extinction depends on the wavelength and the size of the dust particles. Therefore, the light from the celestial object is scattered and absorbed by a different amount. For this reason, the extinction of the light is higher at short wavelengths and smaller at longer wavelengths and this is called "Reddening". The extinction which fits the stellar parameters for model-1 in the J band is $A_J = 0.18$ magnitude and then converted to V-band using $A_J = A_V/3.55$, which means $A_V = 0.64$ (Mathis, 1990). The extinction value for the model-2 is $A_J = 0.0$.

## 4.7.2 The Disk Structure

The model of HD 179218 has an axisymmetric structure and consists of five compo-
nents: star, inner disk, gap, outer disk, and mid-plan. I have assumed that the disk is a
passive and transitional disk according to the previous interferometric MIR observation
by Fedele *et al.* (2008), as shown in Figure 4.9.

Figure 4.9 shows the disk components, the material contained in each component,
and the size of each component. The radius of the inner disk is assumed to be 3.2
AU, the inner radius of the outer disk is 14 AU and the outer radius of the outer disk
is 23 AU. I have used the model-1 input stellar parameters then I changed the size,
power law (p), mass (M), scale height (H), flaring (β) in each component (inner disk,
gap and outer disk) to study their influence on the shape of the SED. I have run the
radiative transfer model and changed the disk parameters to get a good visual fit with
the observational SED.

Besides that, I have produced a synthetic image at 12.5 μm and convolved the image
with the PSF of the calibration star in the Si6 filter. After that, I have compared the
radial brightness profile of the synthetic image with the radial brightness profile of the
science at Si6 filter.
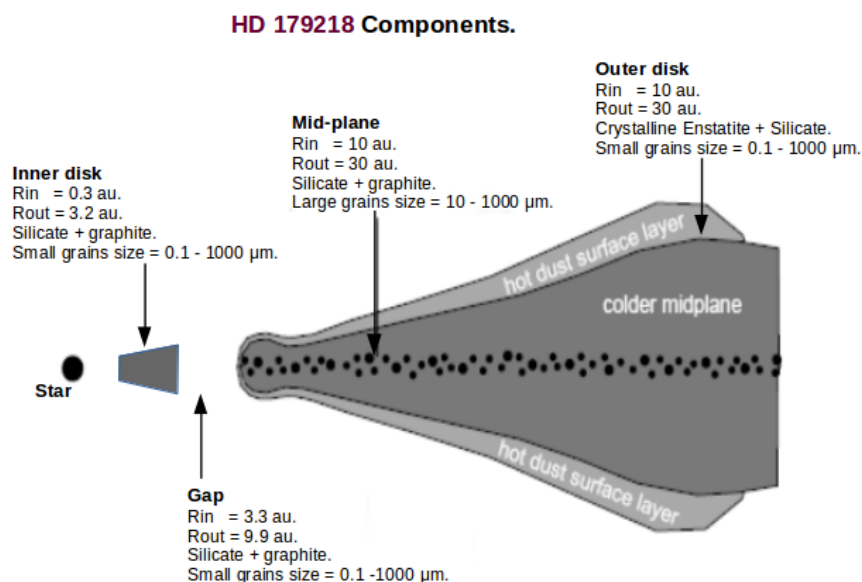


**Figure 4.9:** shows the HD 179218 system components. It also shows the size and the
chemical composition of each component that are used in the RADMC3D to built a disk
model.

### 4.7.3 The Inner Disk

The inner disk have assumed that consists of the dust with very small grains of silicate and graphite. The size of the silicate and graphite grains are between 0.1 - 1000 $\mu m$. The initial size of the inner disk has been taken from Fedele *et al.* (2008) where the disk size extends from 0.2 - 3.2 AU. When the size of the disk is reduced to less than 3.2 AU, it increases the emission in the NIR and in the same time decreases the emission in the MIR and FIR coming from the outer disk. The perfect value for the power law of the surface density in the inner disk is p = 0 where the disk becomes optically thin.

Different values for the power law density have examined such as −2, +2 and then it noticed that the power law of the surface density does not have a significant effect on the NIR part of the SED. If I select the power law of the surface density value p = +2, there is only a very tiny increase of the flux in the NIR. The vertical scale height value of the inner disk should be nearly 0.02 to fit the SED. The major influence on the inner disk comes from the scale height of the disk and the mass of the disk as shown in Figure 4.10.

In the left Figure 4.10 shows, the SED fitting plot and in the right plot shows that the radial brightness profile of the convolved model image is only resolved at 12.5 $\mu m$ continuum emission when the scale height of the inner disk is larger than 0.04. It is unresolved for the scale height less than 0.04.
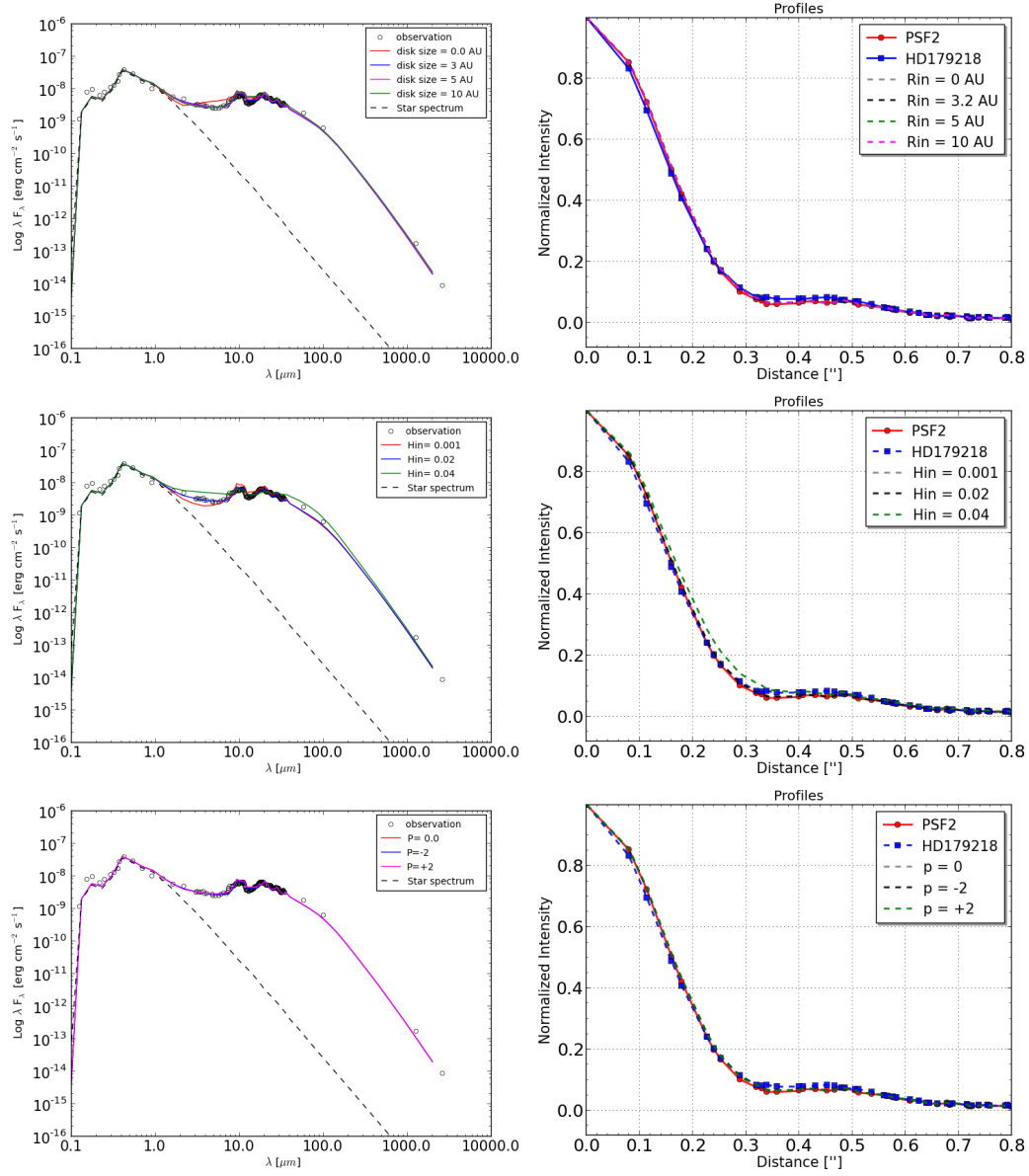
**Figure 4.10:** shows the influence of some parameters such as power law, mass, flaring index, and the vertical scale for the inner disk on the shape of the SED and the radial profile of the convolved image at 12.5 $\mu m$.

### 4.7.4 The Outer Disk

The outer disk consists of the warm atmosphere that emits in the MIR and colder mid-plane which is optically thick and emits in the FIR and sub-millimetre. The dust composition consists of crystalline enstatite and silicate grains according to Juhász *et al.* (2010). I have used an enstatite abundance of 10 % and a silicate abundance of 90 % to fit the SED. Figure 4.11 shows how the abundance in the outer disk plays a role in the shape of the SED. When I chose 100 % of the silicate in the outer disk and 0 % of the enstatite, the shape of the SED got smoother in the FIR region. Therefore, I need to consider a little abundance of the enstatite to get a good fit for the SED.
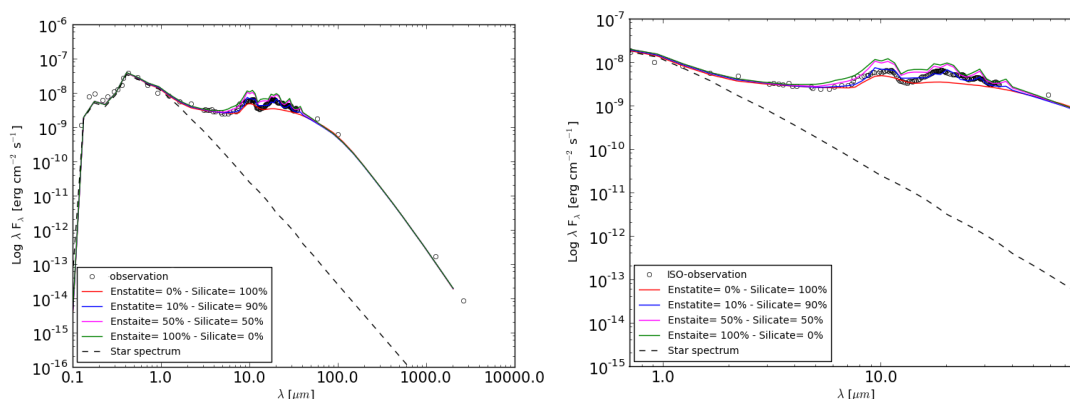


**Figure 4.11:** The left figure shows the influence of the crystalline enstatite on the shape of the whole SED. The right figure shows the specific region in the SED between (1 $\mu m$ - 100 $\mu m$).

The size of the outer disk model is assumed to have different sizes of 30 AU, 50 AU, 80 AU, 100 AU and 150 AU. The SED shows a good fit with an outer disk size of 80 AU. A smaller size makes the flux increase in the MIR. The radial brightness profile of the synthetic image matches with the radial brightness profile of the science at 12.5 $\mu m$ in all sizes as shown in Figure 4.12.

The power law of the surface density has been examined with varying values between -2 and +2 to fit the SED and the radial brightness profile of the synthetic image at 12.5 $\mu m$. The radial brightness profile of the synthetic image becomes larger than the radial brightness profile of the science when the power law of the density is larger than -0.5. I only find a good fit for the observational SED and the radial brightness profile when the power law of the surface density is negative as shown in Figure 4.13.
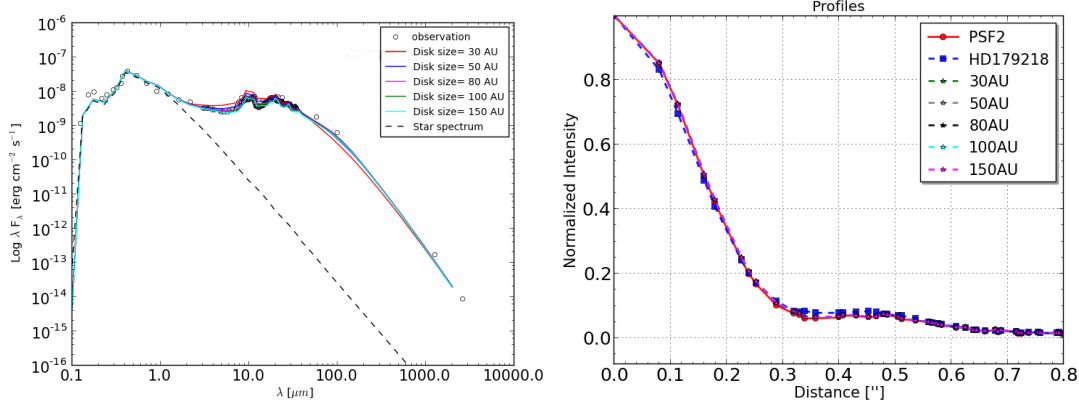
**Figure 4.12:** The left figure shows the influence of change the size of the outer on the shape of the SED. The right figure shows radial brightness profile of the convolve synthetic image at 12.5 $\mu m$ with PSF of the calibration in the Si6 filter.
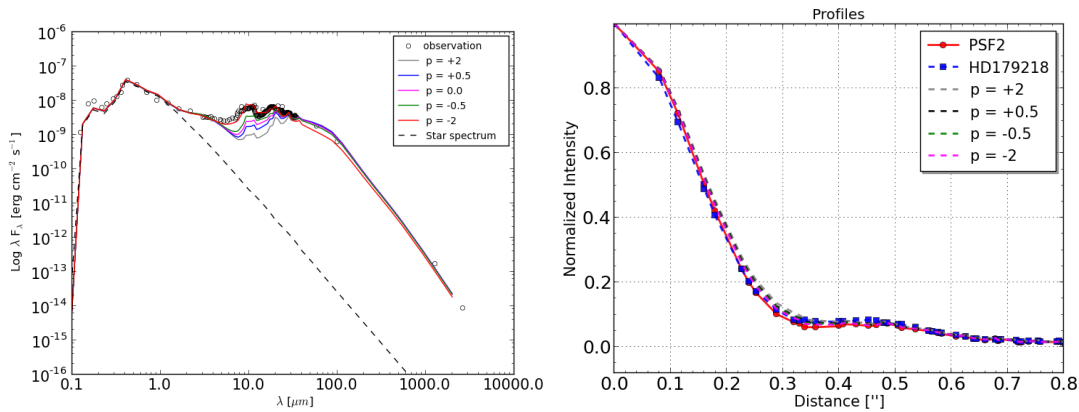


**Figure 4.13:** The left figure shows the influence of changing the power law of the outer disk on the shape of the SED. The right figure shows radial brightness profile of the convolved synthetic image at 12.5 $\mu m$ with the PSF of the calibration in the Si6 filter.

The dust scale height of the outer disk is varied between 0.05, 0.15, and 0.2 to fit the SED and the radial brightness profile of the synthetic image at 12.5 $\mu m$. The effect of the dust scale height on the shape of the SED is very clear. The outer disk become less luminous when the dust scale height decreases. There is an influence on the radial brightness profile of the model only when the scale high is 0.05 as shown in Figure 4.14.

**Figure 4.14:** The left figure shows the influence of the dust scale height of the outer disk on the shape of the SED. The right figure shows the radial brightness profile of the convolved synthetic image at 12.5 $\mu m$ with the PSF of the calibration in the Si6 filter.

Since most studies and observation proved that the MIR emission in the Herbig stars comes from the outer region (Acke and van den Ancker, 2004; Meeus *et al.*, 2001), the mass in the outer disk is examined in this model. I have fitted the SED with the mass in the outer disk to be approximately 0.015 $M_\odot$ which is nearly the same mass as in the Dominik *et al.* (2003) model with 0.01 $M_\odot$. The radial brightness profile shows no change in the size of the PSF of the image model when increasing or decreasing the mass in the outer disk. Figure 4.15 shows how the mass of the outer disk dominates the emission of the outer disk.

The two types of the flaring profile, $\beta = 1/7$ and $\beta = 2/7$, have been tested as in other references (Matter *et al.*, 2016). Figure 4.16 represents the influence of the two types of the flaring on the SED and radial brightness profile at 12.5 $\mu m$.

The inner radius of the outer disk between (6 AU - 20 AU) to fit the SED and the radial brightness profile of the image model. The inner radius of the outer disk has a major influence on the MIR region and on the shape of the PSF of the synthetic image. Due to that, the best fit for the size of the inner radius is 10 AU ± 1 AU. The radial brightness profile of the convolved image model with the PSF of the calibration star is similar to the radial brightness profile of the science in the Si6 filter which means the disk is unresolved in the continuum emission.
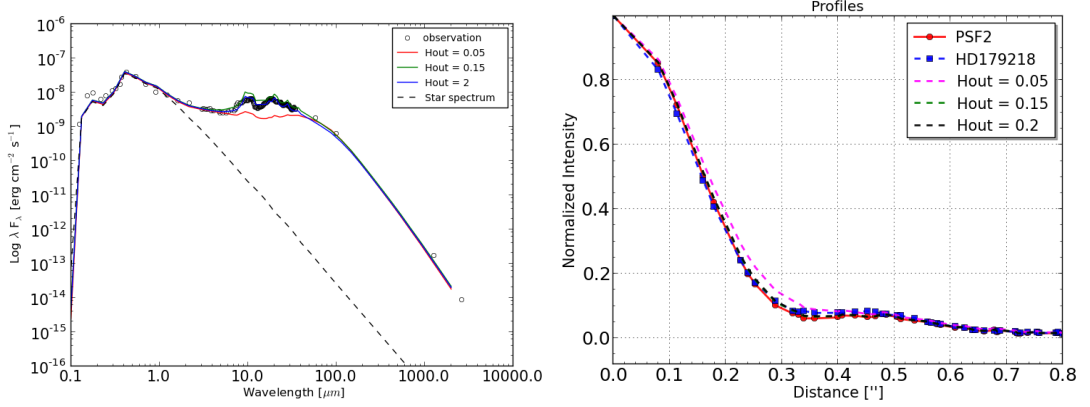
**Figure 4.15:** The left figure shows the influence of varying the mass in the outer disk on the shape of the SED. The right figure shows the radial brightness profile of the convolved synthetic image at 12.5 $\mu m$ with the PSF of the calibration in the Si6 filter.
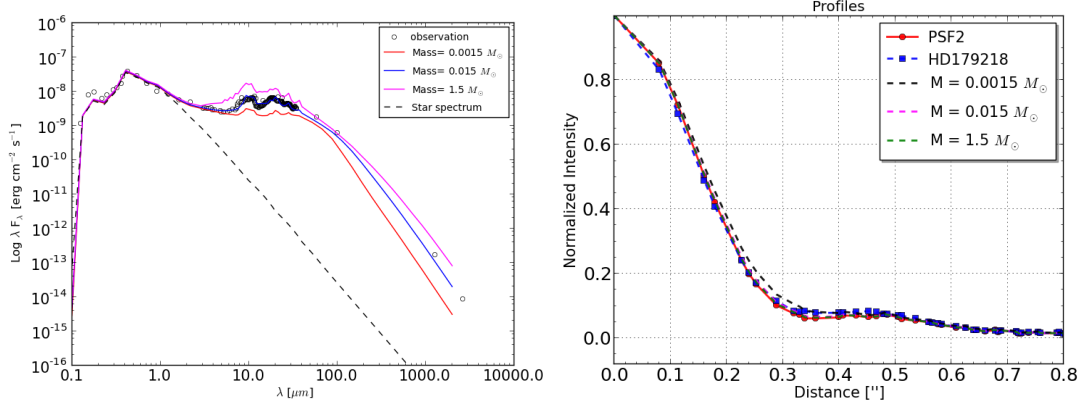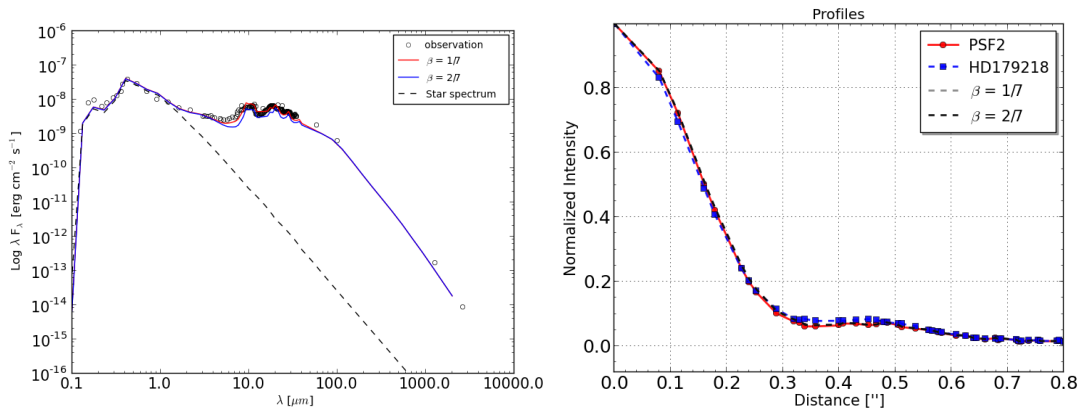


**Figure 4.16:** The left figure shows the influence of two types of flaring in the outer disk on the shape of the SED. The right figure shows the radial brightness profile of the convolved synthetic image at 12.5 $\mu m$ with the PSF of the calibration in the Si6 filter.

On the other hand, the radial brightness profile of the convolved image model becomes larger than the radial brightness profile of the science in the Si6 filter when the size of the inner radius of the outer disk is larger than 15 AU (resolved the disk) as shown in figure 4.17.

**Figure 4.17:** The left figure shows the influence of the inner radius of the outer disk on the shape of the SED. The right figure shows the radial brightness profile of the convolved synthetic image at 12.5 $\mu m$ with the PSF of the calibration in the Si6 filter.

## 4.7.5 The Gap

Gaps are present in many Herbig/Group I stars and there are several mechanisms that might explain gaps such as, photoevaporation, grain growth, a puffed up inner disk, and planet formation in the disk. The dust components in the gap are assumed similar to the outer and inner disk components. The dust in the gap consists of graphite and silicate with smaller grain sizes between 0.1 $\mu m$ - 1000 $\mu m$.

The percentage of graphite in the gap is 40 % larger than in the inner and outer disk. I have chosen the percentage of graphite in the gap between (10 - 20 %). The gap is depleted of the warm dust grains with a small amount still remaining. This small amounts of dust is needed to fit the SED in the MIR as shown in Figure 4.18 and its mass equals 1.4 $\times 10^{-8}$ M$_\odot$.

The left part of Figure 4.18 shows the influence of mass in the gap on the SED while the right part shows that the gap does not have any influence on the radial brightness of the image model. The power law of the surface density in the gap has been tested by varying the value between -2 and 2. A good value for the dust power law was found to fit the SED and radial brightness profile of the image model after convolving the image with the PSF of the calibration star.
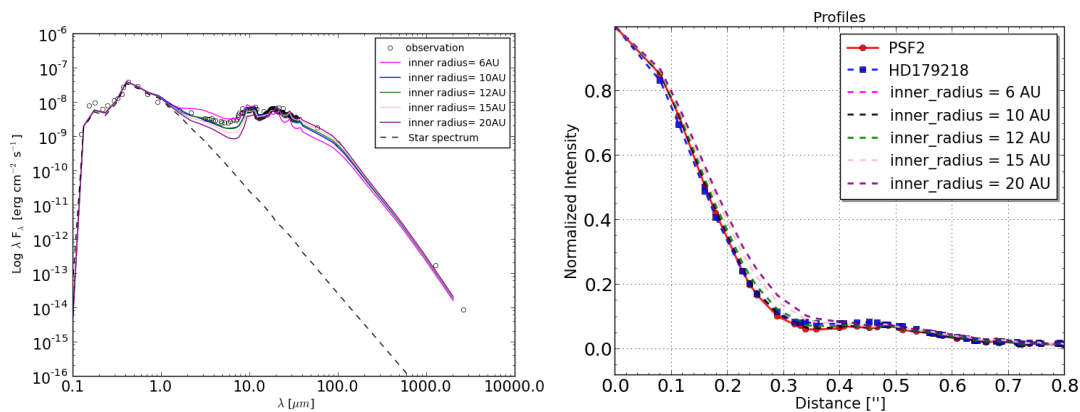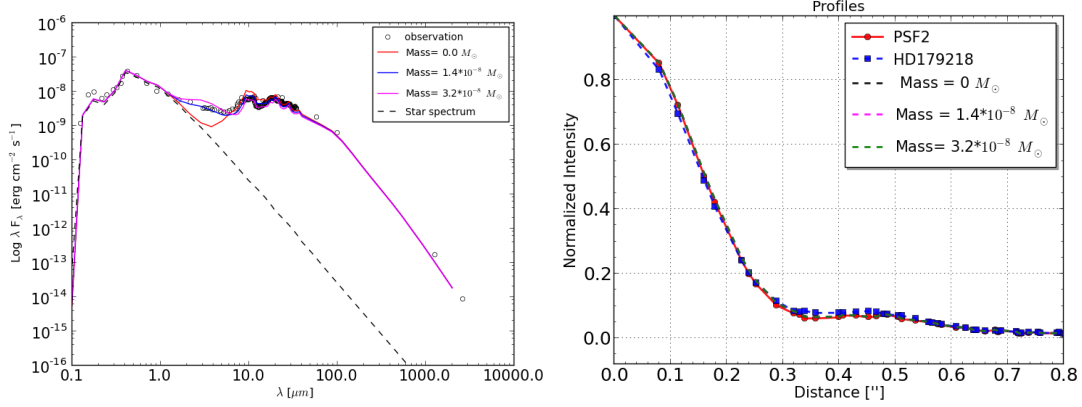
**Figure 4.18:** The left figure shows the influence of the mass in the outer disk on the shape of the SED. The right figure shows the radial brightness profile of the convolved synthetic image at 12.5 $\mu m$ with the PSF of the calibration in the Si6 filter.
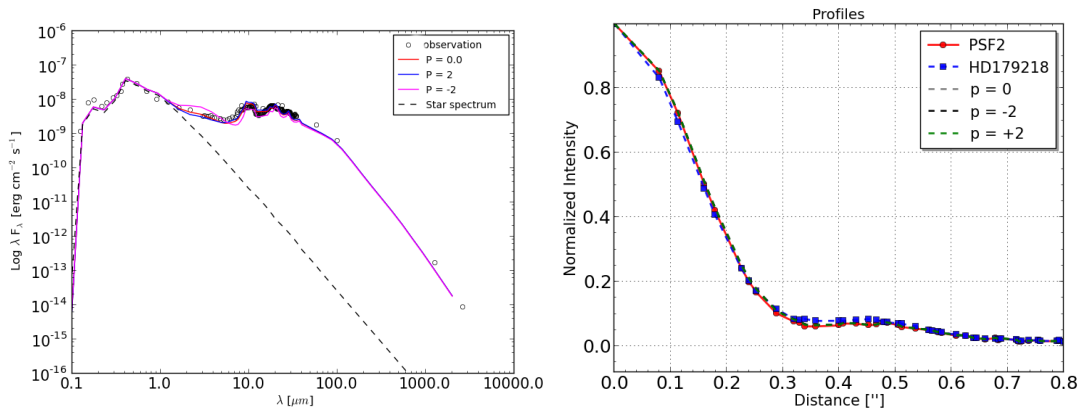


**Figure 4.19:** The left figure shows the impact of the power law of the surface density on the shape of the SED. The right figure shows there is no impact of the radial brightness profile.

Figure 4.19 shows the influence of the power law of the surface density on the SED and the radial brightness profile for the image model in the Si6-filter. The two types of flaring $\beta = 1/7$ and $\beta = 2/7$ have been examined for the gap and I have found that there is no influence from the flaring on the shape of the SED or on the radial brightness profile.

# 4.8  Best Models Fitting

The SED fitting confirmed that the HD 179218 system should have a gap in the disk with a very small and thin inner disk which produces a small amount of emission around 1 $\mu m$. Additionally, the inner disk reduces the flux around 3 $\mu m$ by blocking part of the starlight which would otherwise heat material within the gap.

These effects are depicted in Figure 4.20, which shows the shape of the SED when I remove one of the disk components. When the inner disk component is removed from the system, the gap receives most light from the star and becomes slightly brighter while the flux of the inner radius decreases a bit. On the other hand, the flux of the SED would decrease in the NIR if the gap would not contain any mass and the flux in the inner radius of the outer disk would be increased.
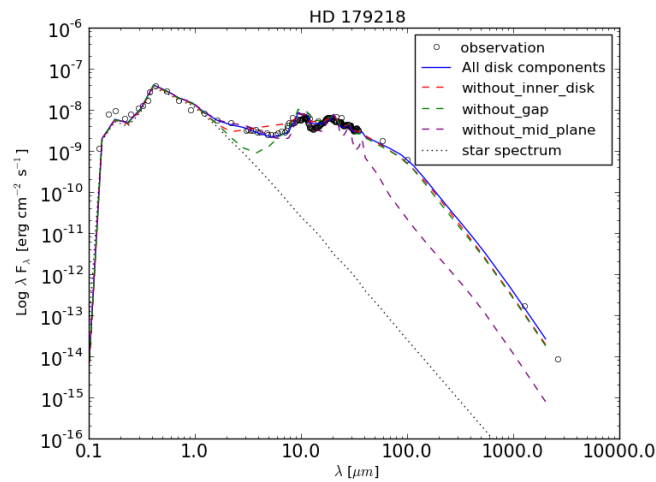


**Figure 4.20:** The SED model with whole disk components (inner disk, gap, mid-plane and outer disk) represents the blue line. The red dashed line represents the disk without inner disk. The green dashed line is the disk without gap. The purple dashed line is the disk without mid-plane. The black open circle represents the observational SED of the HD 179218. The black dotted line represent the spectrum of the star for the model-1 input parameters.

Two different models for the stellar parameters was selected to fit the observational SED and radial brightness profile of the target at 12.5 $\mu m$ as described in the following:

## 4. CHARACTERIZATION OF THE PRE-TRANSITIONAL DISK FOR HD 179218

### 4.8.1 Model-1

To fit the SED and radial brightness profiles of the HD 179218 system using stellar parameters from Alecian *et al.* (2013). I have fixed the stellar parameters, inclination i, position angle PA, and the distance of the system d which are listed in Table 4.11.

After that, I have examined the outer disk parameters by varying the power law of the surface density p between -2 and 2 in steps of 0.5, the inner radius of the outer disk $R_{in}$ between (8 AU - 12 AU) in steps of 1 AU and the outer radius of the outer disk $R_{out}$ with different sizes 30 AU, 50 AU, 80 AU, 100 AU, and 150 AU. The synthetic model of the SED and the radial profile of the image at 12.5 $\mu m$ have been compared with the observations.

The reduced Chi-square method has been used to fit the different SED models as a function of the three parameters p, $R_{in}$, $R_{out}$ and which model at 12.5 $\mu m$ is unresolved. The mathematical expression for the reduced Chi-square method is described in equation:

$$\chi_r^2 = \frac{\chi^2}{N - \upsilon} \tag{4.14}$$

where N is the number of observations and $\upsilon$ is the number of fit parameters.

$$\chi^2 = \sum_{i=1}^{N} \frac{(x_i - \mu_i)^2}{\sigma_i^2} \tag{4.15}$$

where $x_i$ is the observational data, $\mu_i$ is the model and $\sigma_i^2$ is the variance.

The mid-plane and the outer disk have the same parameter value for p in the all models. When I have a positive power law for the surface density $p \geq 0$, this means most of the mass is located in the outer radius of the outer disk and the PSF radial profile at 12.5 $\mu m$ is resolved as shown in Table 4.21.

The negative power law $p \leq 0$ does not fit the SED with low values for the outer disk $R_{out}$, while for the large values of the outer radius (e.g. $R_{out}$ = 150 AU) and a negative power law, the flux in the FIR and sub-mm range is underestimated. The best fit for the SED is obtained when the parameters values are p = -1.5, $R_{in}$ = 10 AU, $R_{out}$ = 80 AU with a non-reduced value of $\chi^2$=302 (or $\chi_r^2$ = 1.9 for N - $\upsilon$ = 157).

The result of the best fit for the SED and synthetic image is given in Figure 4.22. The left figure shows the SED of the model in which the red line almost prefectly fits

the whole SED of the observation in the black open circles. The black dashed line represents the spectrum of the star with an extinction value of $A_V = 0.64$. The right figure shows the synthetic image for the whole system at 12.5 $\mu m$ with inner disk, gap, and outer disk. The inner disk, gap, mid-plane, and the outer disk parameters which have used to create the SED and images are listed in Table 4.12.

The optical depth of the system is the dust opacity $\kappa_v$ times the surface density, as described in the following equation (Williams and Cieza, 2011):

$$\tau_v = \Sigma \kappa_v \qquad (4.16)$$

The radial integrated optical depth of the whole system is calculated and plotted using the RADMC3D code, as shown in Figure 4.23.

I have managed to fit the radial profile by considering the size of the outer disk to be 80 AU, the size of the inner disk to be ∼ 2 AU and the gap extension to be ∼ 7 AU. I have created the image of the this model using the RADMC3D code in three wavelengths 8.6, 11.3 and 12.5 $\mu m$ and convolved the images with two calibrations to get the final convolved image. Figure 4.25 shows the radial profile of the science, calibration and convolved model in three wavelength.

| | Ri | | | | |
|---|---|---|---|---|---|
| | 8 AU | 9AU | 10AU | 11AU | 12AU |
| p=-2,Ro=30AU | 3557 | 2947 | 2433 | 2285 | 1935 |
| p=-1.5,Ro=30AU | 3044 | 2557 | 2206 | 2076 | 1814 |
| p=-1,Ro=30AU | 2553 | 2253 | 1944 | 1912 | 1623 |
| p=0,Ro=30AU | 1967 | 1731 | 1690 | 1665 | 1505 |
| p=+1,Ro=30AU | 1781 | 1676 | 1559 | 1547 | 1418 |
| p=+2,Ro=30AU | 1823 | 1669 | 1637 | 1621 | 1478 |
| | | | | | |
| p=-2,Ro=50AU | 1493 | 1094 | 850 | 718 | 585 |
| p=-1.5,Ro=50AU | 974 | 758 | 607 | 547 | 454 |
| p=-1,Ro=50AU | 578 | 482 | 448 | 443 | 408 |
| p=0,Ro=50AU | 469 | 500 | 529 | 534 | 566 |
| p=+1,Ro=50AU | 848 | 840 | 848 | 853 | 841 |
| p=+2,Ro=50AU | 1132 | 1124 | 1114 | 1112 | 1082 |
| | | | | | |
| p=-2,Ro=80AU | 727 | 503 | 376 | 309 | 291 |
| p=-1.5,Ro=80AU | 391 | 330 | *302* | 325 | 365 |
| p=-1,Ro=80AU | 346 | 407 | 443 | 530 | 609 |
| p=0,Ro=80AU | 1075 | 1154 | 1172 | 1227 | 1264 |
| p=+1,Ro=80AU | 1730 | 1707 | 1737 | 1743 | 1753 |
| p=+2,Ro=80AU | 1893 | 1890 | 1906 | 1898 | 1886 |
| | | | | | |
| p=-2,Ro=100AU | 633 | 471 | 373 | 330 | 333 |
| p=-1.5,Ro=100AU | 423 | 385 | 365 | 409 | 474 |
| p=-1,Ro=100AU | 477 | 565 | 610 | 682 | 781 |
| p=0,Ro=100AU | 1489 | 1489 | 1489 | 1489 | 1489 |
| p=+1,Ro=100AU | 2074 | 2097 | 2106 | 2112 | 2138 |
| p=+2,Ro=100AU | 2328 | 2330 | 2330 | 2360 | 2350 |
| | | | | | |
| p=-2,Ro=150AU | 644 | 548 | 499 | 499 | 550 |
| p=-1.5,Ro=150AU | 582 | 603 | 643 | 721 | 806 |
| p=-1,Ro=150AU | 777 | 898 | 987 | 1074 | 1226 |
| p=0,Ro=150AU | 1951 | 2012 | 2131 | 2173 | 2242 |
| p=+1,Ro=150AU | 2992 | 2965 | 2973 | 3015 | 3063 |
| p=+2,Ro=150AU | 3356 | 3385 | 3407 | 3360 | 3412 |

**Figure 4.21:** Non-reduced Chi-square table to fit the SED with different values for parameters p, $R_{in}$, $R_{out}$. The light and gray boxes represent the models at 12.5 $\mu m$ which has unresolved and resolved PSFs, respectively.
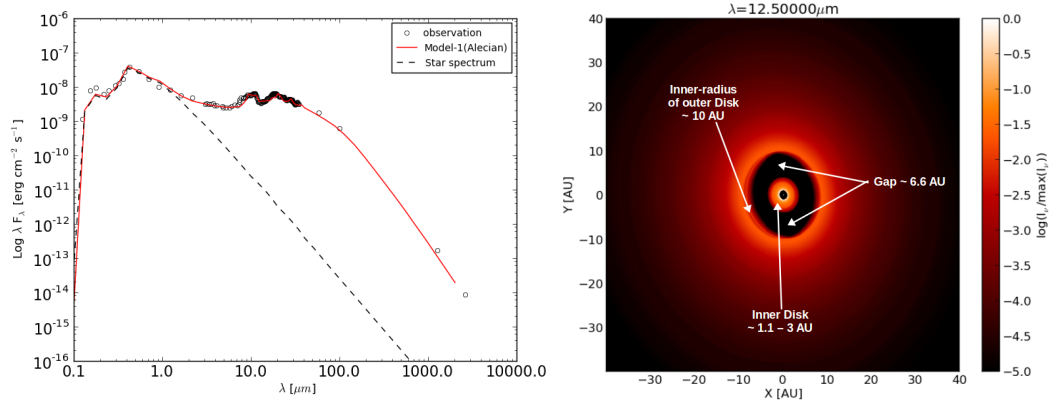
**Figure 4.22:** The left plot shows the best SED fitting for stellar input parameters of the model-1. The black open circle represents the observational SED and the red line represents my model for the HD 179218 system. The black dotted line represents the spectrum of the star for the model-1 input parameters. The right figure shows the model of the transitional disk with a gap for the input parameters of the model-1 and is made by using the RADMC3D code.
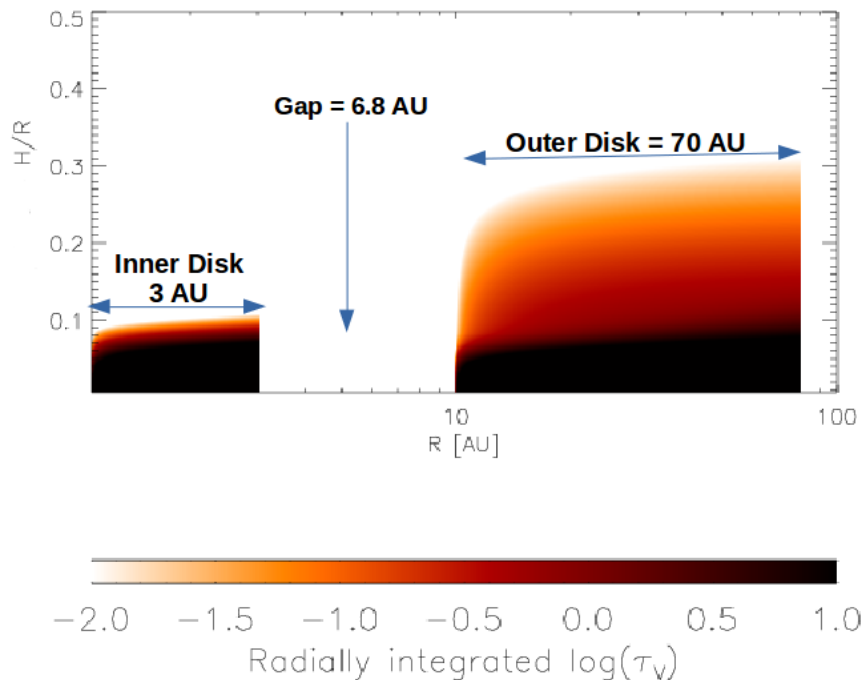


**Figure 4.23:** The radial integrated optical depth at 12.5 $\mu m$ for the HD 179218 system.

**Table 4.12:** The disk parameters that I used to fit the observational SED and the radial profile of the image at 12.5 $\mu m$ with stellar input of the Model-1.

**(a)** Inner disk parameters for the small grains.

| Parameters | Values |
|---|---|
| Silicate fraction | 100 % |
| graphite fraction | 0 % |
| $R_{in}$ | 1.1 AU |
| $R_{out}$ | 3 AU |
| Size | 1.9 AU |
| Mass | 0.0015 $M_{\odot}$ |
| p | 0 |
| $H_{in}$ | 0.02 |
| $\beta$ | 1/7 |

**(b)** Gap parameters for the small grains.

| Parameters | Values |
|---|---|
| Silicate fraction | 60 % |
| graphite fraction | 40 % |
| $R_{in}$ | 3.1 AU |
| $R_{out}$ | 9.9 AU |
| Size | 6.8 AU |
| Mass | $2 \times 10^{-11} M_{\odot}$ |
| p | 0 |
| $H_{in}$ | 0.1 |
| $\beta$ | 1/7 |

**(c)** Mid-plane parameters for the large grains.

| Parameters | Values |
|---|---|
| Silicate fraction | 70 % |
| graphite fraction | 30 % |
| $R_{in}$ | 10 AU |
| $R_{out}$ | 80 AU |
| Size | 70 AU |
| Mass fraction | 99 % |
| p | -1.5 |
| $H_{out}$ | 2 |
| $\beta$ | 3/7 |

**(d)** Outer disk parameters for the small grains.

| Parameters | Values |
|---|---|
| Enstatite fraction | 10 % |
| Silicate fraction | 90 % |
| $R_{in}$ | 10 AU |
| $R_{out}$ | 80 AU |
| Size | 70 AU |
| Mass | 0.015 $M_{\odot}$ |
| p | -1.5 |
| $H_{out}$ | 0.12 |
| $\beta$ | 1/7 |

**Notes.** Note that $R_{in}$ is the inner radius of the disk, $R_{out}$ is the outer radius of the disk. p is the power law of the surface density, $H_{in}$ is the scale height of the inner radius and $H_{out}$ is the scale height of the outer radius. $\beta$ is the flaring of the disk.

### 4.8.2 Model-2

Another set of stellar parameters have taken where the star is less luminous and has less temperature compared with model-1 parameters. This model is also used to fit the observational SED and the radial profile of the convolved image of the model with the science image at wavelength 12.5 $\mu m$. The stellar parameters of Model-2 are taken from Dominik *et al.* (2003) and listed in Table 4.11.

The parameters that are considered to fit the SED and the radial profile of the science image are shown in Table 4.13. The table consists of the geometric parameters for the four components: inner disk, gap, outer disk and mid-plane with values that fit the SED and the radial profile of the science at 12.5 $\mu m$. The extinction value for this model that I selected to fit the SED is $A_V = 0.0$
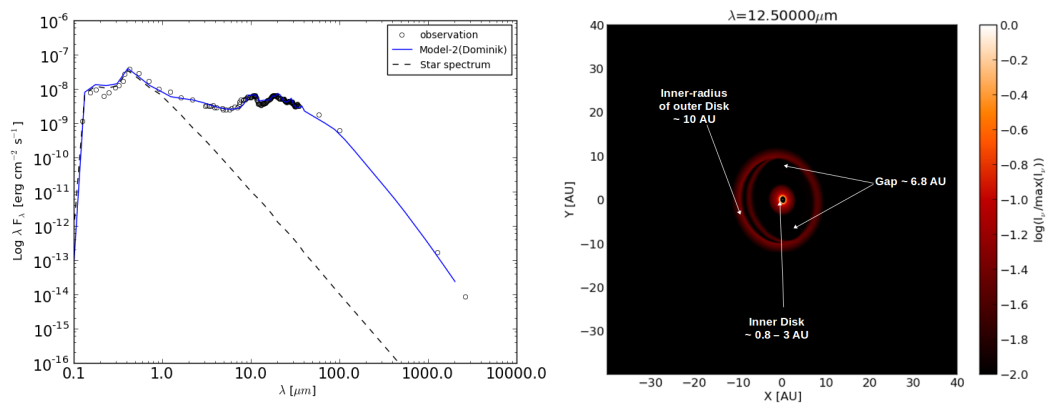


**Figure 4.24:** The left plot shows the best SED fitting for stellar input parameters of the model-2. The black open circle represents the observational SED and the blue line represents my model for the HD 179218 system. The black dotted line represents the spectrum of the star for the model-2 input parameters. The right figure shows the model of the transitional disk with gap for the input parameters of the model-2 and is made by using RADMC3D code.

**Table 4.13:** The disk parameters that used to fit the observational SED and the radial profile of the image at 12.5 $\mu m$ with stellar input of the Model-2.

**(a)** Inner disk parameters for the small grains.

| Parameters | Values |
|---|---|
| Silicate fraction | 80 % |
| graphite fraction | 20 % |
| $R_{in}$ | 0.8 AU |
| $R_{out}$ | 3 AU |
| Size | 2.2 AU |
| Mass | $6 \times 10^{-4} M_{\odot}$ |
| p | 0 |
| $H_{in}$ | 0.04 |
| $\beta$ | 1/7 |

**(b)** gap parameters for the small grains.

| Parameters | Values |
|---|---|
| Silicate fraction | 60 % |
| graphite fraction | 40 % |
| $R_{in}$ | 3.1 AU |
| $R_{out}$ | 9.9 AU |
| Size | 6.8 AU |
| Mass | $2.2 \times 10^{-20} M_{\odot}$ |
| p | 0 |
| $H_{in}$ | 0.1 |
| $\beta$ | 1/7 |

**(c)** Mid-plane parameters for the large grains.

| Parameters | Values |
|---|---|
| Silicate fraction | 100 % |
| graphite fraction | 0 % |
| $R_{in}$ | 10 AU |
| $R_{out}$ | 80 AU |
| Size | 70 AU |
| Mass fraction | 94 % |
| p | -2 |
| $H_{out}$ | 2 |
| $\beta$ | 1/7 |

**(d)** Outer disk parameters for the small grains.

| Parameters | Values |
|---|---|
| Enstatite fraction | 10 % |
| Silicate fraction | 90 % |
| $R_{in}$ | 10 AU |
| $R_{out}$ | 80 AU |
| Size | 70 AU |
| Mass | 0.014 $M_{\odot}$ |
| p | -2 |
| $H_{out}$ | 0.18 |
| $\beta$ | 1/7 |

**Notes.** Notice that $R_{in}$ is the inner radius of the (inner disk, gap or outer disk), $R_{out}$ is the outer radius of the (inner disk, gap or outer disk). p is the power law of the surface density, $H_{in}$ is the scale height of the inner radius and $H_{out}$ is the scale height of the outer radius. $\beta$ is the flaring of the disk.

## 4.9 The Radial Brightness Profile Model Fitting

Images of the best fit model in the continuum emission have been created for all three wavelengths 8.6, 11.3 and 12.5 $\mu m$ and for the two input models. After that, the image models have convolved with the PSF of the two calibration stars HD  169414 and HD 187642.

Figure 4.25 shows the radial profile of the science in the black open circles and it is resolved in the PAH filters (8.6 $\mu m$, 11.3 $\mu m$). The red open square show the two calibration stars in the three filters and the blue dashed line represents the convolved image model in three thermal filters. The radial profile of the science in the silicate filter 8.6 $\mu m$ is unresolved for calibration and models.

The intensity is normalized to 1 and plotted in the x-axis, and the y-axis is the distance in arcsecond. The radial profile fits for an inner radius of the outer disk of 10 AU and outer disk size of 80 AU. The important change for fitting the radial profile is to change the value of the density power-law from positive to negative and a better value is found in the range -1.5 and -2 for model-1 and model-2.
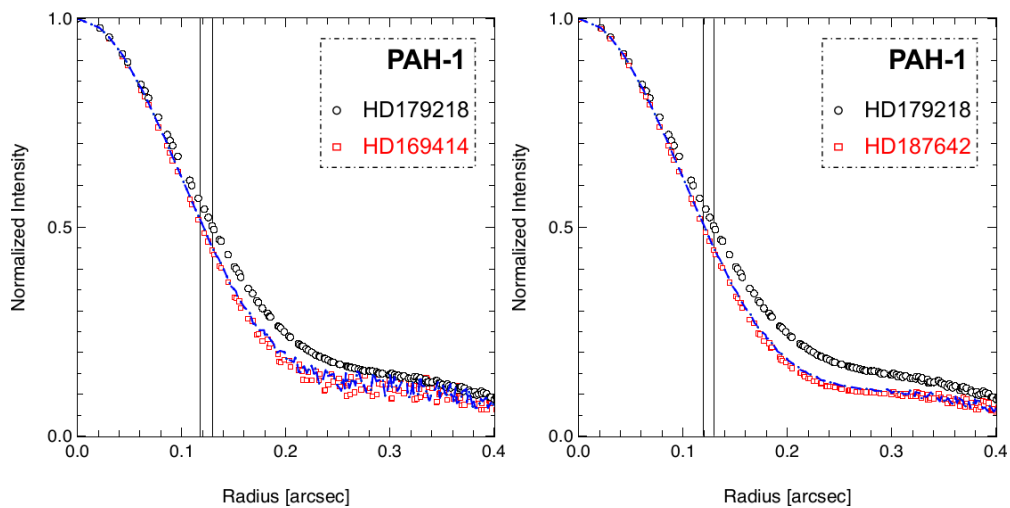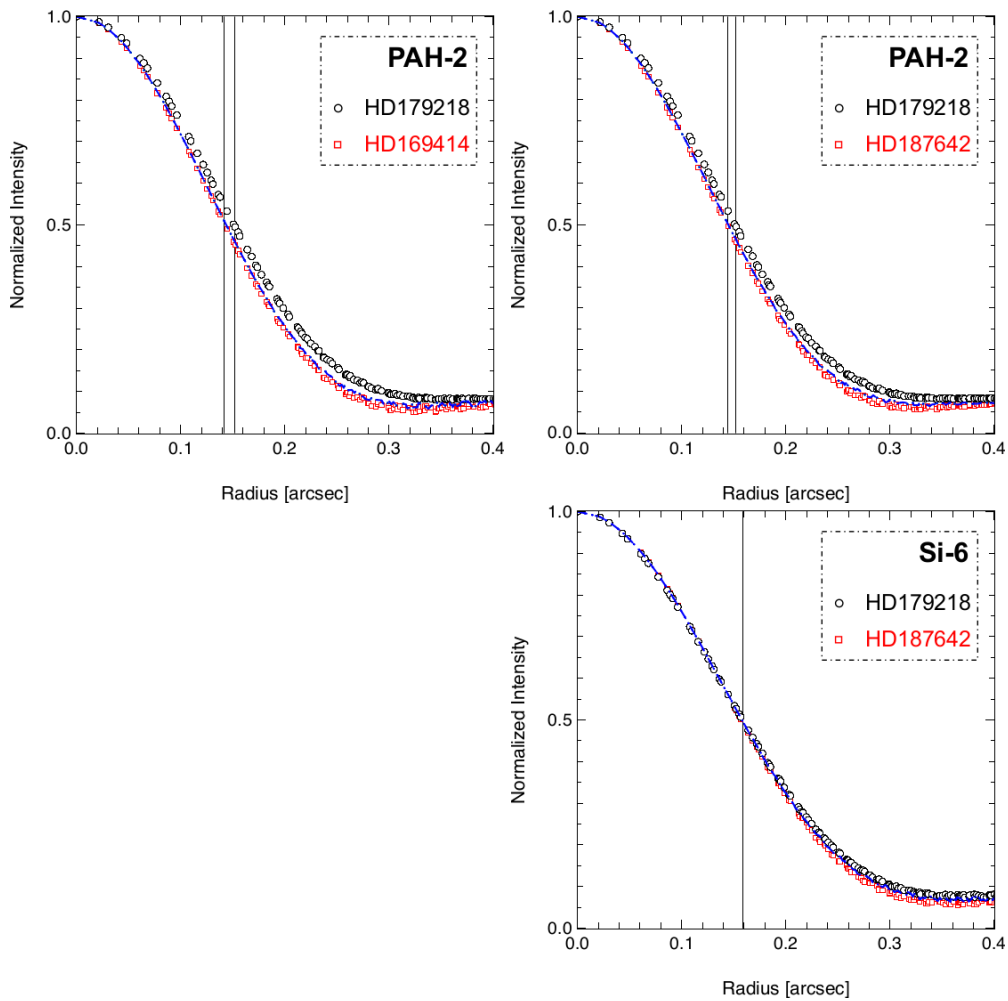
**Figure 4.25:** The plots show radial profiles of the science, calibrator and the model of HD 179218 in the three filters PAH1, PAH2 and Si6. The open black circles refer to the science star, the open red squares refer to the calibrator stars and the dashed blue line is the radial profile of the synthetic image after convolving it with the PSF of the calibrators. The vertical black lines represent the differences in the FWHM between the science and the calibrator according to the value in Table 4.3.

## 4.10 Comparing HD 179218 with HD 97048

The origin of the PAH emission comparing to the continuum emission in HD 179218 have been investigated more in this thesis. In the first step, it is necessary to extract the flux density in the continuum from the total emission that was observed using the GTC at 8.6 $\mu m$ and 11.3 $\mu m$. Therefore, I have subtracted the photometry measurement in Table 4.10 from the flux density of the PAH contribution 3.8 Jy, 2.85 Jy at 8.6 $\mu m$ and 11.3 $\mu m$, respectively as measured by Juhász *et al.* (2010). The result of the subtraction represents the value of the flux density in the continuum which is 11.4 Jy, 19.1 Jy for 8.6 $\mu m$ and 11.3 $\mu m$, respectively. In the second step, I have built a hybrid model of the image in the continuum based on the image for HD 179218 that I have created using RADMC3D. Then, I overlapped it with a geometrical model that has a PAH brightness distribution to examine the radial profile of the Gaussian model and uniform disk modified model (UD) with radius $R_{UD}$ by changing the power law r$^P$ for the PAH emission.

The result of this procedure is shown in Figure 4.26, where the blue filled dots represent the science radial profile, the black dotted line represents the radial profile of the Gaussian model and the red line represents the uniform disk model in two filters PAH1 (left) and PAH2 (right). The radial profiles are fitted in the core of the science PSF and there is only an underestimate of the emission in the wings at 8.6 $\mu m$ as shown in the zoom-in (top right corner of the plot in Figure 4.26).
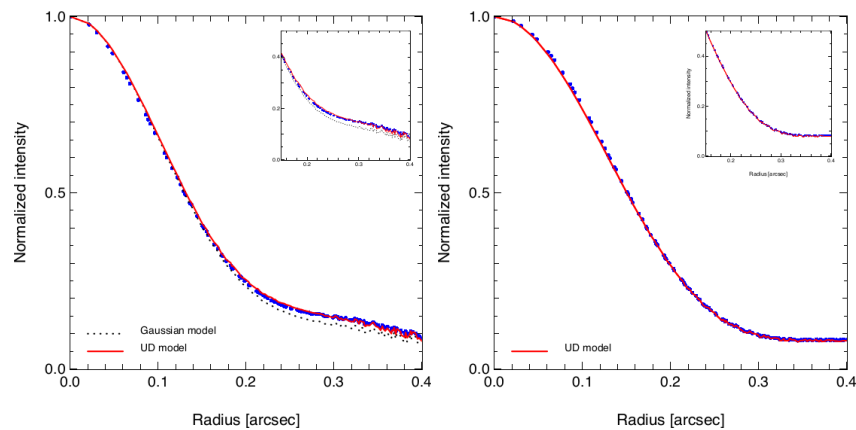


**Figure 4.26:** shows the model of the science PSF profile with a hybrid model based on the Gaussian disk and on the uniform disk models in the PAH1 (left) and PAH2 filter (right). Zoom-in view of the wings are shown in the right corener of the plots.

## 4. CHARACTERIZATION OF THE PRE-TRANSITIONAL DISK FOR HD 179218

Besides that, the uniform disk model (UD) which has p=0, $R_{UD}$ = 0.3″ (87 AU at distance = 293 pc) is matching the radial profile of HD 179218. Despite the small size of the emission is estimated around HD 179218 by applying the quadratic subtraction of FWHM, this result shows that the emission at 8.6 $\mu m$ and 11.3 $\mu m$ extends relatively in the large distance of the outer disk. This extended emission of the PAH in the outer disk of HD 179218 is similar to the case of the disk emission that is found around HD 97048 in same filter, where HD 97048 is a Herbig star and the emission is resolved to several tens of the astronomical units using VLT / VISIR in the 8.6 $\mu m$ and 11.3 $\mu m$ (Doucet *et al.*, 2006). The disk diameter around HD 97048 is extracted by quadratic subtraction and is ∼ 40 AU at a distance of 180 pc, which is slightly larger than the disk around HD 179218. Since HD 97048 is closer than HD 179218, the emission is better resolved in the outer disk of HD 97048. The result of the resolved emission proves that the FWHM of the science is 1.32 times larger than the FWHM of the calibration star. Figure 4.27 shows FWHM in the PAH2 (11.3 $\mu m$) filter and the FWHM in the silicate filter SIV (10.49 $\mu m$) for HD 97048. There is a large amount of the PAH emission in the wings of the HD 97048 PSF and it is ∼ 380 AU in radius (Doucet *et al.*, 2006).
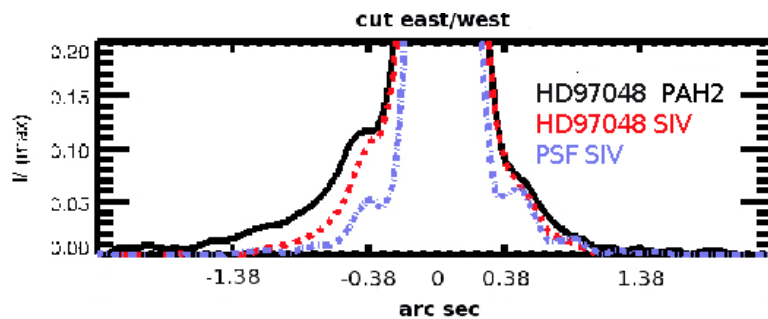


**Figure 4.27:** shows the radial profiles of the observed HD 97048 using VLT / VISIR in PAH2 and SIV bands, and the calibration star HD 85503 in the SIV band. The black line represents the radial profile of the HD 97048 image in the PAH2 band, the red dashed line represents the radial profile of HD 97048 in the SIV band and the blue dashed dot line represents the radial profile of the calibration star image in the SIV band (Doucet *et al.*, 2006).

# 4.11 PAHs Charge State in the HD 179218

There are two states for the PAH emission in Herbig stars disks. Either it is ionized
or neutral, depending on studies performed recently by Maaskant *et al.* (2013, 2014).
These studies make a comparison between PAH emission and thermal continuum emission of four Herbig stars and found that the PAH emission in the pre-transitional disk
can originate either in the inner optical thin disk (high-UV radiation and low electron
density) or in the outer optical thick disk (low-UV radiation and high electron density).

Moreover, these studies suggest that there is a relation between the spatial extent
of the PAH emission and continuum emission, where the charge state of the PAH
molecules can be traced by comparing the ratio of the $I_{6.2}/ I_{11.3}$ or $I_{3.3}/ I_{7.7}$ such as in
Figure 4.28, or by comparing the relative strength of emission at 8.6 *μm* and 11.3 *μm*
(Maaskant *et al.*, 2014).
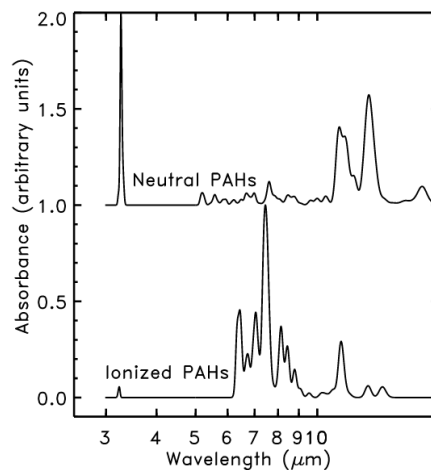


**Figure 4.28:** shows two types of spectra for the PAHs emission. The neutral PAH emission
is represented in the top and the ionized PAH emission is represented in the bottom (Peeters
*et al.*, 2002).

Therefore, the PAH emission that is caused by the neutral PAH molecules can be
traced by comparing the strong emission for 3.3 *μm* and 11.3 *μm* features in the MIR
spectrum like in the PAH emission around HD 97048 (Doucet *et al.*, 2006; Lagage
*et al.*, 2006). In the opposite case, the PAH emission that is caused by the ionized PAH
molecules can be traced by the ratio of $I_{6.2}/I_{11.3}$ where the ratio should be larger than
unity and the size of the PAH emission at 11.3 *μm* and should be more compact than
the continuum emission like the emission around IRS 48 (Maaskant *et al.*, 2014).

## 4. CHARACTERIZATION OF THE PRE-TRANSITIONAL DISK FOR HD 179218

For HD 179218, numerous studies based on ISO and Spitzer spectroscopy have confirmed the stronger emission for the PAH feature at 8.6 $\mu m$ compared to the PAH emission at 11.3 $\mu m$ (Acke *et al.*, 2010; Juhász *et al.*, 2010; Meeus *et al.*, 2001; Seok and Li, 2017).

By comparing the continuum subtracted spectrum of the HD 179218 model with two other Herbig star spectra (IRS 48 and HD 97048 models), It was found that there is a similarity between the spectrum of HD 179218 and the spectrum of IRS 48 in terms of strength of the emission at 6.2 $\mu m$ and 7.7 $\mu m$ features compared to 11.3 $\mu m$, as shown in Figure 4.29, the spectra are normalized to the peak emission at 6.3 $\mu m$.
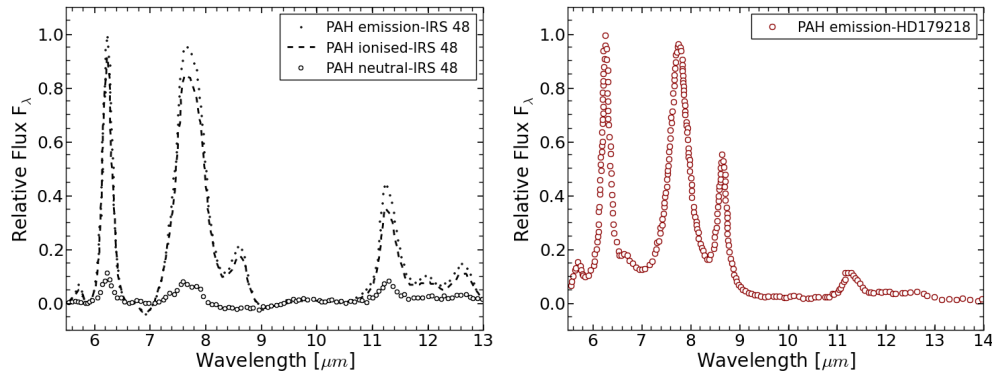


**Figure 4.29:** Left-figure: the plot shows the PAH emission model for IRS 48 which is extracted from Maaskant *et al.* (2014). The small dotted line represents the total PAH emission, the dashed line represents the emission from the ionised PAH (optically thin disk) and the large open circles represent the PAH emission from the neutral PAH (optically thick disk). Right-figure: the red open circles represent the PAH emission model for HD 179218 from Seok and Li (2017).

Based on the PAH emission scenario around IRS 48, the PAH emission is ionized and located in the optically thin disk around HD 179218. However, observational MIR imaging results and the model for HD 179218 suggest that the PAH emission does not originate in the inner disk, but that it may extend to the outer disk surface.

# 5

# Spatially Resolved Imaging of the Debris Disk for Epsilon Eridani

## 5.1 Introduction

Many debris disks are detected around main sequence stars like the sun. These debris disks consist of icy, rocky bodies, comets, and asteroids. The size of grains in debris disks are in the range of micron sized particles to kilometre sized planetesimals. The zodiacal light in our solar system is a very attractive example of a debris disk and can be observed by the naked eye.

The origin of the dust in the debris disk and in a very close region to the star (exozodical dust cloud) is still mysterious. The time scale for dust depletion due to Poynting-Robertson drag is very short compared to the age of the system. Therefore, the dust in the inner region must be transient or produced by external sources.

Most of the debris disks can be detected by resolving the emission around the star in MIR and FIR wavelengths. The warm dust in the habitable zone of a debris disk is important to study and to learn more about the terrestrial planet formation, to image possible planets, and to study the relation between the dust in debris disks and planets.

In the last few years, many theories predicted a statistical correlation between the debris disk population and planets. Wyatt *et al.* (2007) and Raymond *et al.* (2012) predicted that debris disks hosting planets tend to emit more in the infrared than debris disks without planets.

## 5. SPATIALLY RESOLVED IMAGING OF THE DEBRIS DISK FOR EPSILON ERIDANI

Numerous observations have proven this relation such as images for the two different systems $\beta$ Pic and HR 8799 (Lagrange *et al.*, 2009; Marois *et al.*, 2008), respectively. The presence of a giant planet in the debris disk induces different structures in these disks such as clumps, warps, cavities, etc. because of the dynamical interaction.

A recent analysis from Spitzer space observatory data discovered a relation between debris disks and masses of planets in the nearest 60 G-type stars. Four out of the six stars which have a planet with mass smaller than Saturn also show evidence for a debris disk (Wyatt *et al.*, 2012). More recent surveys dependent on data from the Herschel Space Observatory / DUNES programme show that 20 ± 2 % of stars like sun have a debris disk similar to the Kuiper belt (Pilbratt *et al.*, 2010). The rate of the detection mostly depends on the temperature of the star and the observatory sensitivity, and reaches up to 30 % in the case of the A-type stars.

In the last ten years many observations using space and ground-based telescopes in the MIR with higher angular resolution have been able to resolve debris disks in a few astronomical units around the star. One example is the debris disk surrounding star $\zeta$ Lep,a 230 Myr old A-type star resolved by Moerchen *et al.* (2007) using Gemini South with MIR camera. The resolved disk is 3 AU which is comparable to the size of the asteroid belt in our solar system. Moerchen *et al.* (2010) used MIR imaging from Spitzer and IRAS for a sample of A stars to resolve the debris disks.

## 5.2  Epsilon Eridani Target

Epsilon Eridani known also as (Ran, HR1084, HD 22049, HIP16537), is a main sequence star with an age between 0.5 - 1.4 Gyr. It has a spectral type K2V is located at a distance of 3.2 pc and the mass of the star is 0.8 $M_\odot$ (Bonfanti *et al.*, 2015; Di Folco *et al.*, 2004). It is one of the so-called "fabulous four" ($\beta$ Pictoris, Fomalhaut, Vega) showing IR emission which comes from the debris disk around the star and that was the first time detecte a debris disk around main sequence star using IRAS space telescope (Aumann *et al.*, 1984).

The debris disk of Epsilon Eridani has been resolved with Multi-Band Imaging Photometer for Spitzer (MIPS) at 24 $\mu m$, 70 $\mu m$ and imaged in the sub-millimetre at 450 $\mu m$ and 850 $\mu m$ using the JCMT / Submillimeter Common-User Bolometer Array (SCUBA). The face-on images show a multi-ring structure at distance 20 AU to 120 AU similar to our Kuiper belt. The clumpy structure of the debris disk is due

to the known Jovian planet close to the habitable zone of the system. (Backman *et al.*, 2009; Chavez-Dagostino *et al.*, 2016; Greaves *et al.*, 1998).

According to Greaves *et al.* (1998); Greaves *et al.* (2014); Reidemeister *et al.* (2011) the disk is composed of four components: two belts in the inner regions, a ring consisting of ice, silicate and silicate halo (Figure 5.1). The radius of the two inner belts models is 3 AU and 20 AU with temperatures of 155 K and 55 K, respectively.

The outer disk radius of the ice and silicate extend between 35 AU - 90 AU while the radius of the silicate halo extends between 90 AU - 110 AU. The model suggests that the warm dust in the inner region is originating from the outer region and transported to the inner region by Poynting-Robertson drag.

The two inner belts are responsible for more than 95 % IR emission between 20 $\mu m$ - 30 $\mu m$ at T = 100 K - 150 K. These two belts consist of astronomical silicate grains with a size of the grains of 3 $\mu m$ for both belts. In addition to that, two giant planets in the inner region of the disk are observed using radial velocity analysis (Hatzes *et al.*, 2000; Moran *et al.*, 2004). This motivates us to study the exozodiacal dust of Epsilon Eridani in MIR wavelength using high angular resolution to resolve the inner disk.



|     |     |     |
| --- | --- | --- |
| (a) | (b) | (c) |
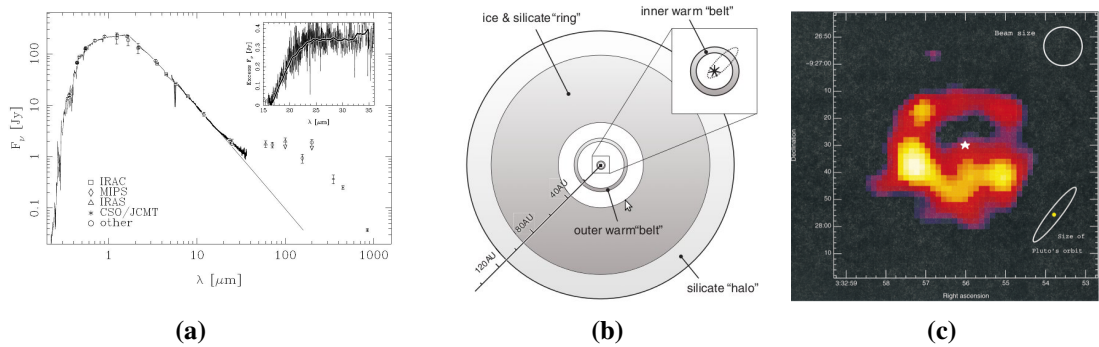
**Figure 5.1:** (a) The SED of Epsilon Eridani extracted from different space and ground-based telescopes. (b) The model of the disk including the prediction of an inner emission at ∼ 3 AU (Backman *et al.*, 2009). (c) Observed emission around Epsilon Eridani using JCMT at 850 $\mu m$ (Greaves *et al.*, 1998).

## 5.3   Observation and Data Reduction

Epsilon Eridani was observed in the Q4 filter $\lambda = 20.5\ \mu m$ using GTC telescope with CanariCam instrument. The observation has been taken on $6^{th}$ of January 2013 for standard star Gamma Eridani then the science target Epsilon Eridani, followed again by Gamma Eridani. The optical seeing was poor in average ($> 1''$) and the measured PWV is above to the limit (PWV $\lesssim$ 5mm) even that can be considered is acceptable for the Q-band and good for the N-band.

The observations sequence and more details of the observations are listed in Table 5.1. The first reference star 80 Cet has observed and used only for photometric calibration not for PSF calibration. The shape of the PSF for 80 Cet is not clear to make a comparison with PSF of the science target. While the second reference star Gamma Eridani has used for the PSF and photometric calibration with the science target. The best image quality cannot be guaranteed with GTC telescope because the telescope does not have fast guiding. Therefore I have to test the data during observation and I have to set some criteria to select good data in the following sections.

**Table 5.1:** Summary of observations of the science target Epsilon Eridani and reference stars Gamma Eridani on $6^{th}$ of January 2013.

| Object | UT | Inte. Time | Seeing['']  | Airmass | PWV[mm] | Flux |
|--------|-----|-----------|-----------|---------|---------|------|
| 80 Cet | 19:55:04-19:58:36 | 165s | 1.16 | 1.27 | 5.9 | Photometric Ref. |
| GammaEri. | 20:35:54-20:39:27 | 134s | 1.08 | 1.466 | 5.6 | PSF and phot. Ref. |
| EpsilonEri. | 20:50:33-21:25:33 | 1568s | 1.54±0.05 | 1.28 | 5.4 | Science |
| GammaEri. | 21:45:42-21:49:14 | 113s | 1.5 | 1.353 | 5.2 | PSF and phot. Ref. |
| GammaEri. | 21:50:19-21:53:51 | 108s | 1.4 | 1.351 | 5.2 | PSF and phot. Ref. |
| EpsilonEri. | 22:11:26-22:46:05 | 1568s | 1.20±0.1 | 1.306 | 5.2 | Science |
| GammaEri. | 22:52:27-22:55:59 | 139s | 1.27 | 1.39 | 6.0 | PSF and phot. Ref. |
| 80 Cet | 23:00:50-23:04:21 | 165s | 1.32-1.15 | 1.55 | 5.9 | Photometric Ref. |

# 5.4 Full-Width-at-Half-Maximum

## 5.4.1 FWHM Measurements of Savesets

The quality of the image can be determined by measuring the PSF of the image, ellipticity, and Strehl-ratio. Therefore, I have performed a non liner least square fit of the PSF (Lorentzian fit) for every saveset of the reference star and every saveset of the science star. There is no difference in this case between a Lorentzian fit or a Gaussian fit because they have a similar central part of the PSF (Li *et al.*, 2010).
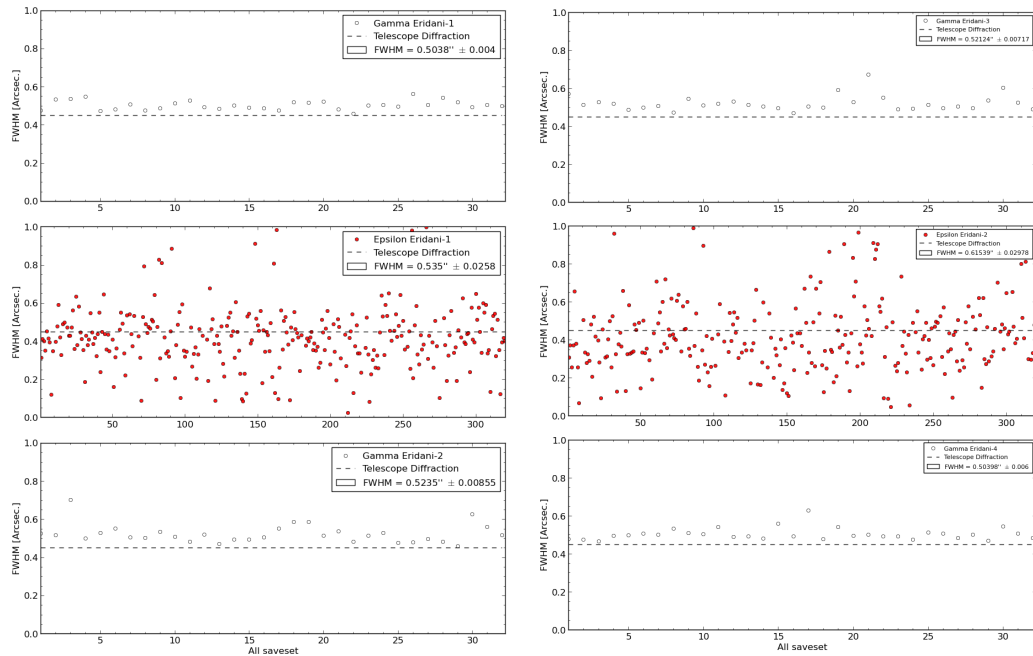


**Figure 5.2:** The FWHM measurements for each saveset of the reference-science-reference in the first column and again reference-science-reference in the second column. The black open circles show the reference star, the red fill circle shows the science star and the black dashed line shows the diffraction limit of the telescope.

Figure 5.2 shows the FWHM change during the observation for the reference star (Gamma Eridani) and science star (Epsilon Eridani) in the Q4 filter. The black open circles represent the reference star and the red circles represent the science star. The black dashed line shows the diffraction limit of the GTC telescope at wavelength 20.5 $\mu m$ which is 0.45″. The science star is observed longer than the reference star because it

is less bright. The FWHM of the reference star is more stable during the observation and the effect of the atmosphere in the FWHM is less. The FWHM of the science star was not stable during the observation as shown in Figure 5.2.

Therefore, I have examined the FWHM of the science in different methods before stacking the saveset to get the final image. Many of the FWHM values for the science star are below the diffraction limit of the telescope and it is better to discard them from the data to avoid those bias values. I have selected only reasonable values of the FWHM in the range 0.45″ - 0.8″. The upper limit of 0.8″ is chosen because larger than this value it has a very bad shape of the PSF. Table 5.2 shows the integration time and the number of the saveset before and after applying this condition.

**Table 5.2:** FWHM measurements for savesets before and after applying a condition.

| Object | Inte. Time[s] | All saveset | FWHM[″] | Inte. Time[s] | Select saveset | FWHM[″] |
|---|---|---|---|---|---|---|
| GammaEri. | 165.14 | 32 | 0.5038 ± 0.0040 | 165.14 | 32 | 0.5038 ± 0.0040 |
| EpsilonEri. | 1651.48 | 320 | 0.5350 ± 0.0258 | 510.48 | 99 | 0.5264 ± 0.0063 |
| GammaEri. | 165.14 | 32 | 0.5235 ± 0.0086 | 165.14 | 32 | 0.5235 ± 0.0086 |
| GammaEri. | 165.14 | 32 | 0.5212 ± 0.0071 | 165.14 | 32 | 0.5212 ± 0.0071 |
| EpsilonEri. | 1651.48 | 320 | 0.6153 ± 0.0298 | 438.67 | 85 | 0.550 ± 0.0090 |
| GammaEri. | 165.14 | 32 | 0.5041 ± 0.0060 | 165.14 | 32 | 0.5041 ± 0.0060 |

Different methods have followed to select a reference and science frames. The frames which have a FWHM value in the range of the $1\sigma$, $2\sigma$, and $3\sigma$ have selected. In this method, the average of the FWHM of all frames for the reference and science stars have measured then calculated the standard deviation of the average. Frames that contain values of the FWHM less or larger than (FWHM$_{average}$± $1\sigma$ ,$2\sigma$, and $3\sigma$) are discarded from my calculations. Figure 5.3 shows the FWHM measurements after applying the above criteria. The average of the FWHM has been extracted before and after applying the criteria. Tables 5.3, 5.4 and 5.5 shows the average of the FWHM for Gamma Eridani and Epsilon Eridani with percentage of removed savesets and integration time for $1\sigma$, $2\sigma$, and $3\sigma$.
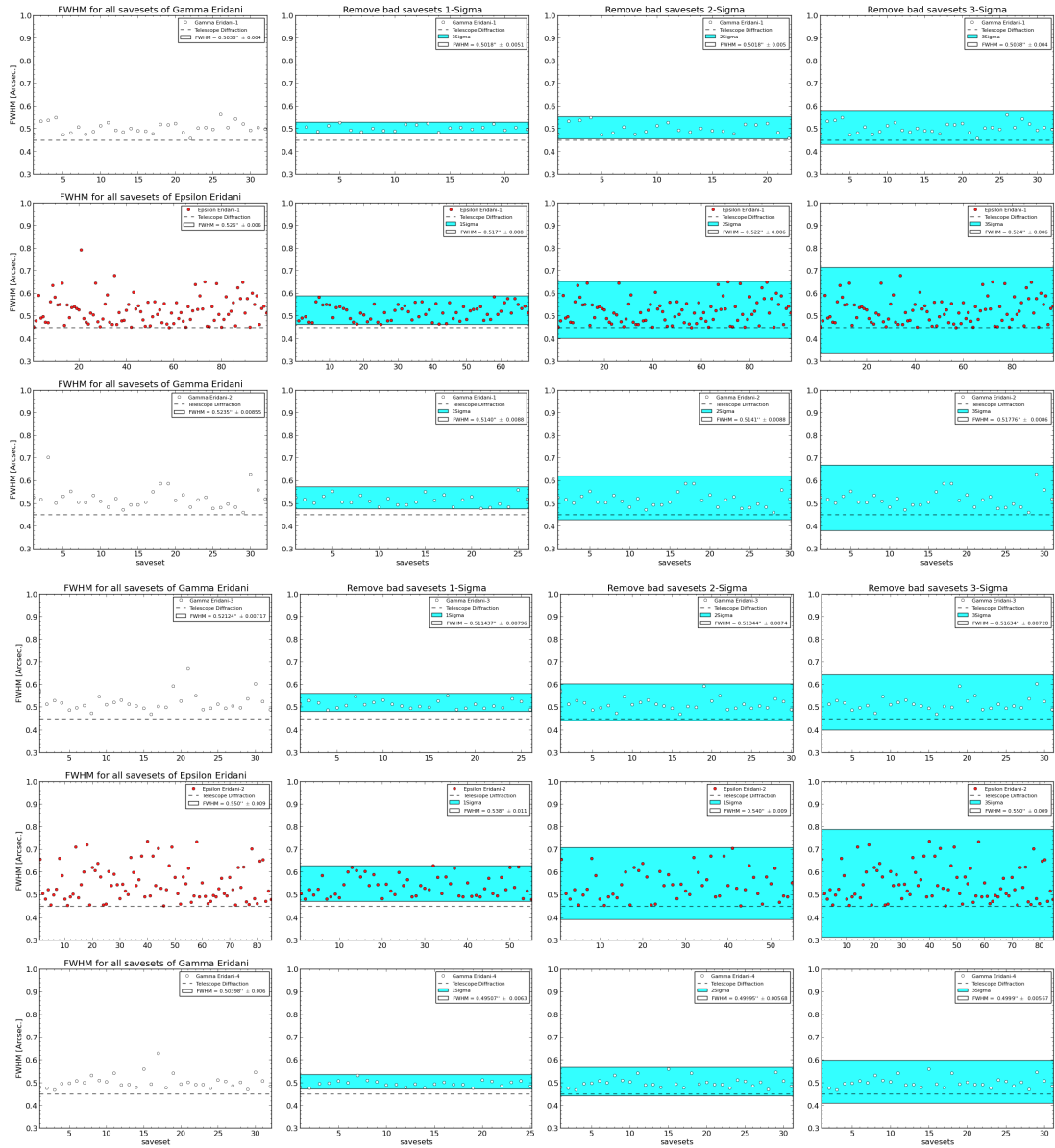
**Figure 5.3:** From the left to right: FWHM measurement for all savesets of Epsilon Eridani and Gamma Eridani with a FWHM between (0.45-0.8″) and after applying the criteria for 1σ, 2σ, and 3σ.

## 5. SPATIALLY RESOLVED IMAGING OF THE DEBRIS DISK FOR EPSILON ERIDANI

I conclude from the FWHM measurement that Epsilon Eridani is larger than Gamma Eridani using FWHM measurements within $1\sigma$, $2\sigma$, and $3\sigma$.

Savesets shown a very high background noise effect from the atmospheric background and it can hardly recognize the PSF of the saveset, therefore it is better to measure the FWHM of each nodset instead of the saveset. Each nodset is composed of 8 stacked savesets by using the iDealCam code. In contrast to the PSF of the saveset, the PSF of the nodset is clearly recognized as shown in Figure 5.4.

**Table 5.3:** FWHM measurements for savesets 1-Sigma.

| Object | Total Time [Sec] | No. saveset | Percentage[%] | FWHM [″] ± $3\sigma$ |
|--------|------------------|-------------|---------------|----------------------|
| GammaEri. | 113.50 | 22 | 68.75 | 0.502 ± 0.005 |
| EpsilonEri. | 350.85 | 68 | 68.69 | 0.517 ± 0.008 |
| GammaEri. | 134.18 | 26 | 81.25 | 0.514 ± 0.009 |
| GammaEri. | 134.18 | 26 | 81.25 | 0.511 ± 0.007 |
| EpsilonEri. | 283.84 | 55 | 64.71 | 0.538 ± 0.011 |
| GammaEri. | 129.01 | 25 | 78.12 | 0.495 ± 0.006 |

**Table 5.4:** FWHM measurements for savesets 2-Sigma.

| Object | Total Time [Sec] | No. saveset | Percentage[%] | FWHM [″] ± $3\sigma$ |
|--------|------------------|-------------|---------------|----------------------|
| GammaEri. | 159.98 | 31 | 96.88 | 0.502 ± 0.005 |
| EpsilonEri. | 500.16 | 97 | 97.98 | 0.522 ± 0.006 |
| GammaEri. | 154.8 | 30 | 93.75 | 0.514 ± 0.009 |
| GammaEri. | 154.8 | 30 | 93.75 | 0.513 ± 0.007 |
| EpsilonEri. | 412.8 | 80 | 94.12 | 0.540 ± 0.009 |
| GammaEri. | 154.8 | 31 | 96.88 | 0.511 ± 0.006 |

**Table 5.5:** FWHM measurements for savesets 3-Sigma.

| Object | Total Time [Sec] | No. saveset | Percentage[%] | FWHM [$''$] $\pm 3\sigma$ |
|--------|------------------|-------------|---------------|---------------------------|
| GammaEri. | 165.14 | 32 | 100 | 0.504 ± 0.004 |
| EpsilonEri. | 505.68 | 98 | 98.99 | 0.524 ± 0.006 |
| GammaEri. | 159.96 | 31 | 96.88 | 0.518 ± 0.009 |
| GammaEri. | 159.96 | 31 | 96.88 | 0.516 ±0.007 |
| EpsilonEri. | 438.67 | 85 | 100 | 0.550 ±0.009 |
| GammaEri. | 159.96 | 31 | 96.88 | 0.511 ± 0.006 |
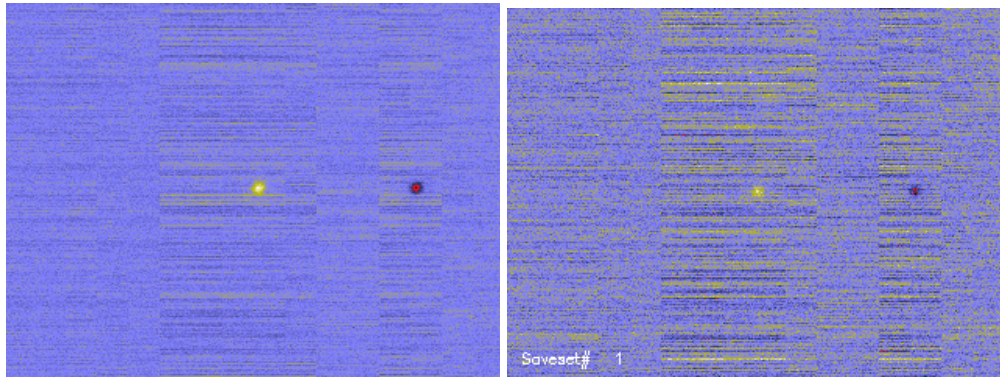


**Figure 5.4:** The left image shows a nodset frame and has a single target with a positive image in the middle of the frame and a negative image on the right. The right image shows one saveset frame with a positive image of the target in the middle and a negative image on the right side.

## 5.4.2 FWHM Measurements of Nodsets

The FWHM for each nodset of Epsilon Eridani have measured using the iDealCam code and the FWHM measurements for each saveset of Gamma Eridani have achieved using a Lorentzian fit code. The total number of savesets for Gamma Eridani is 32 which results in 4 nodsets. It is difficult to notice the FWHM behaviour from only 4 measurements. Therefore, I preferred to keep the saveset measurements of the FWHM for Gamma Eridani and compare it with the Epsilon Eridani. Figure 5.5 shows the FWHM measurement for each saveset of Gamma Eridani and each nodset for Epsilon Eridani.
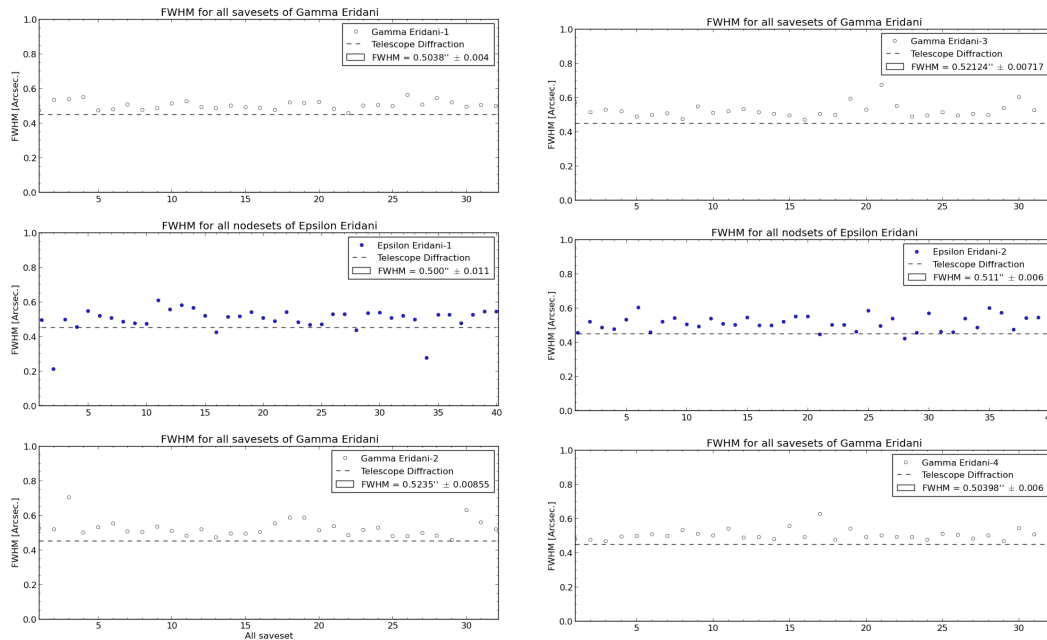
**Figure 5.5:** The FWHM measurements for each savesets-nodsets-savesets of the reference-science-reference respectively in the first column and again reference-science-reference in the second column.

Figure 5.5 shows values of the FWHM for Epsilon Eridani that are lower than the diffraction limit of the telescope. The same procedure was followed with all saveset measurements by discarding the FWHM values which have smaller values than the diffraction limit of the telescope.

The FWHM of Gamma Eridani is never measured to be smaller than the diffraction limit of the telescope. Therefore, It is not needed to discard any of the FWHM measurements of Gamma Eridani from the data. The integration time for each nodset (8 savesets) is 20.64 seconds because the integration time for each saveset is 2.58 seconds.

Table 5.6 shows the sequence of observations for Gamma Eridani and Epsilon Eridani, the total numbers of the savesets for Gamma Eridani, and the total number of the nodsets for Epsilon Eridani before and after discarding the FWHM measurements which are below the diffraction limit of the telescope (0.45″) as shown in Figure 5.5.
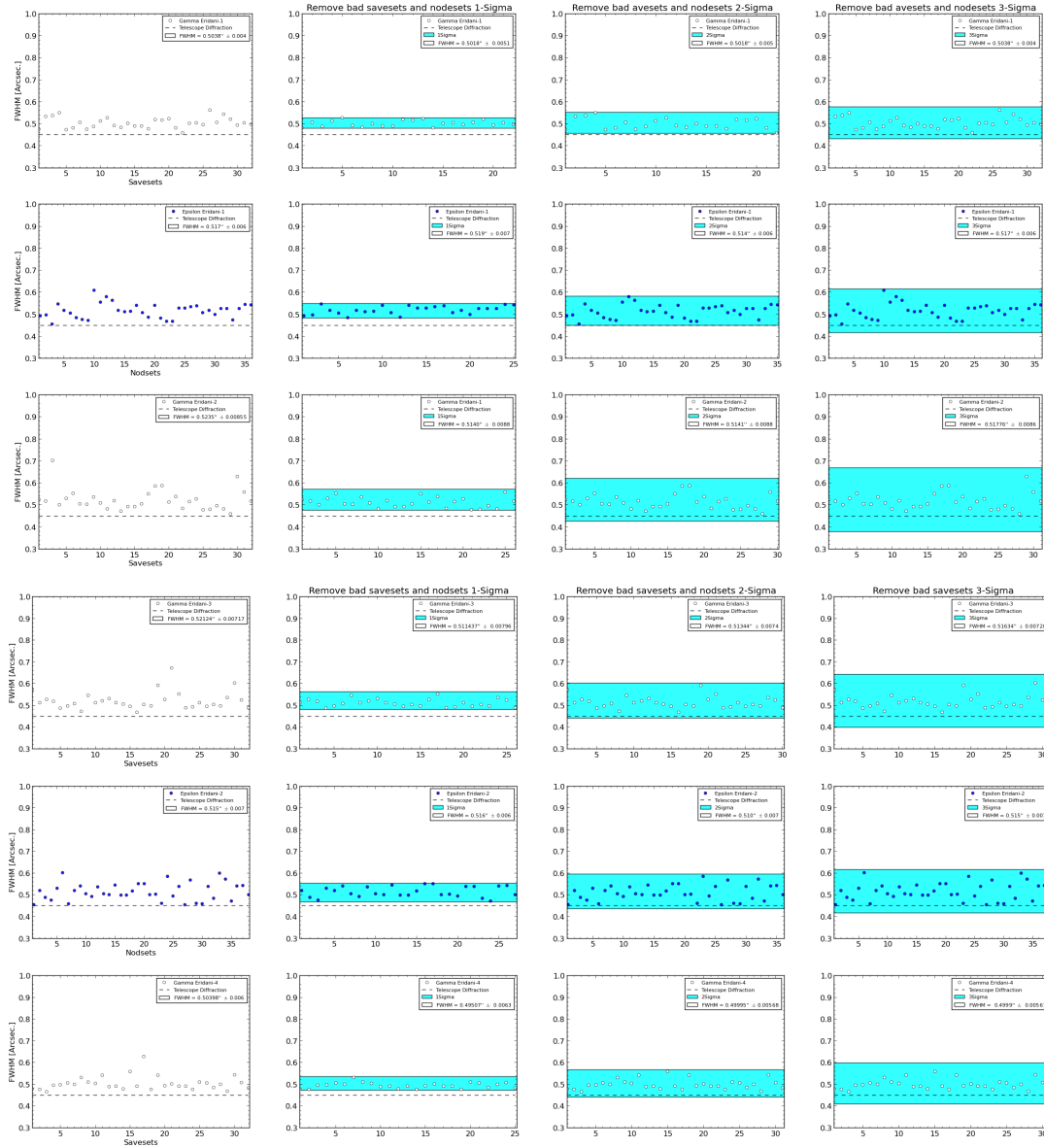
**Table 5.6:** FWHM measurements for nodsets before and after discarding frames.

| Object | Inte. Time[s] | All | FWHM[″] | Inte. Time[s] | Select | FWHM[″] |
|---|---|---|---|---|---|---|
| GammaEri. | 165.14 | 32(saveset) | 0.504 ± 0.004 | 165.14 | 32(saveset) | 0.504 ± 0.004 |
| EpsilonEri. | 1651.48 | 40(nodsets) | 0.500 ± 0.011 | 1486.3 | 36(nodsets) | 0.517 ± 0.033 |
| GammaEri. | 165.14 | 32(saveset) | 0.524 ± 0.009 | 165.14 | 32(saveset) | 0.524 ± 0.009 |
| GammaEri. | 165.14 | 32(saveset) | 0.521 ± 0.007 | 165.14 | 32(saveset) | 0.521 ± 0.007 |
| EpsilonEri. | 1651.48 | 40(nodsets) | 0.511 ± 0.006 | 1568.8 | 38(nodsets) | 0.515 ± 0.007 |
| GammaEri. | 165.14 | 32(saveset) | 0.504 ± 0.006 | 165.14 | 32(saveset) | 0.504 ± 0.006 |

By following the same method which used in section 5.4.1 to select saveset frames of reference and nodset frames for the science stars. Figure 5.6 shows the FWHM measurements after frame selection. The FWHM average for the reference and the science star have measured before and after applying the selection.

Tables 5.7, 5.8 and 5.9 show the average of the FWHM of the savesetes for Gamma Eridani and the average of the FWHM of the nodsets for Epsilon Eridani including the percentage of removed savesets or nodsets and the integration time for $1\sigma$, $2\sigma$, and $3\sigma$.

**Figure 5.6:** FWHM measurements for all savesets of Gamma Eridani in (black open circle). Blue circles show the FWHM of the selected saveset frames for Epsilon Eridani within $1\sigma$, $2\sigma$, and $3\sigma$.

**Table 5.7:** FWHM measurements for 1-Sigma.

| Object | Total Time [Sec] | No. of Select | Percentage[%] | FWHM [″] |
|---|---|---|---|---|
| GammaEri. | 113.50 | 22(savesets) | 68.75 | 0.502 ± 0.005 |
| EpsilonEri. | 1032.2 | 25(nodsets) | 69.44 | 0.517 ± 0.006 |
| GammaEri. | 134.18 | 26(savesets) | 81.25 | 0.514 ± 0.009 |
| GammaEri. | 134.18 | 26(savesets) | 81.25 | 0.511 ± 0.007 |
| EpsilonEri. | 1114.7 | 27(nodsets) | 71.05 | 0.516 ± 0.006 |
| GammaEri. | 129.01 | 25(savesets) | 78.13 | 0.495 ± 0.006 |

**Table 5.8:** FWHM measurements for 2-Sigma.

| Object | Total Time [Sec] | No. of Select | Percentage[%] | FWHM [″] |
|---|---|---|---|---|
| GammaEri. | 159.98 | 31(saveset) | 96.88 | 0.502 ± 0.005 |
| EpsilonEri. | 1445 | 35(nodsets) | 97.22 | 0.514 ± 0.006 |
| GammaEri. | 154.8 | 30(saveset) | 93.75 | 0.514 ± 0.009 |
| GammaEri. | 154.8 | 30(saveset) | 93.75 | 0.513 ± 0.007 |
| EpsilonEri. | 1486.28 | 36(nodsets) | 94.74 | 0.510 ± 0.007 |
| GammaEri. | 154.8 | 31(saveset) | 96.88 | 0.511 ± 0.006 |

**Table 5.9:** FWHM measurements for 3-Sigma.

| Object | Total Time [Sec] | No. of Select | Percentage[%] | FWHM [″] |
|---|---|---|---|---|
| GammaEri. | 165.14 | 32(saveset) | 100 | 0.504 ± 0.004 |
| EpsilonEri. | 1486.29 | 36(nodsets) | 100 | 0.517 ± 0.006 |
| GammaEri. | 159.96 | 31(saveset) | 96.88 | 0.518 ± 0.009 |
| GammaEri. | 159.96 | 31(saveset) | 96.88 | 0.516 ±0.007 |
| EpsilonEri. | 1568.86 | 38(nodsets) | 100 | 0.515 ±0.007 |
| GammaEri. | 159.96 | 31(saveset) | 96.88 | 0.511 ± 0.006 |

### 5.4.3   FWHM Measurements of Ellipticity Selection

The ellipticity of the PSF is used to select good and bad frames. The ellpiticity of a
good frame as stated in the GTC telescope web-page for the Q4 filter is 0.06. The
ellipticity is described by the following equation:

$$Ellipticity = 1 - \frac{\text{FWHM}_y}{\text{FWHM}_x} \tag{5.1}$$

where $\text{FWHM}_y$ is the semi-major axis and $\text{FWHM}_x$ is the semi-minor axis. The
$\text{FWHM}_x$ and $\text{FWHM}_y$ are extracted from the fitted PSF. The ellipticity is considered a
good index of the image quality (Li *et al.*, 2010).

Therefore, I have selected savesets of Gamma Eridani and nodsets of Epsilon Eri-
dani which have ellipticity equal or less than 0.06. The table below shows the average
of the FWHM in the limit of the ellipticity criteria.

**Table 5.10:** FWHM measurements selected by Ellipticity criteria.

| Object | Total Time [Sec] | No. of Select | Percentage[%] | FWHM ["] |
|---|---|---|---|---|
| GammaEri. | 98.04 | 19(savesets) | 59.38 | 0.498 ± 0.029 |
| EpsilonEri. | 1032 | 25(nodsets) | 69.44 | 0.510 ± 0.083 |
| GammaEri. | 67.08 | 13(savesets) | 40.63 | 0.520 ± 0.059 |
| GammaEri. | 103.20 | 20(savesets) | 62.50 | 0.514 ± 0.048 |
| EpsilonEri. | 701.84 | 17(nodsets) | 44.74 | 0.518 ± 0.067 |
| GammaEri. | 108.36 | 21(savesets) | 65.63 | 0.496 ± 0.026 |

Many frames for Gamma Eridani and for Epsilon Eridani was discarded even if
they show a good PSF shape by visually (no elongation of the PSF visible) because
these frames have a too large value of the ellipticity.

### 5.4.4   FWHM Measurements of Visual Selection

The savesets of Gamma Eridani do not have values less than the diffraction limit of the
telescope. From visual checking I find that some PSF shapes are elongated. Therefore,
it is better to check them visually to ensure that bad frames are not included in the final
image.

The same criteria have applied for the nodsets measurement of Epsilon Eridani because the PSF of the saveset is not as clear as the PSF of the nodsets. Figure 5.7 shows the FWHM of the reference and the science stars after selecting good frames visually. The FWHM values during observation for the reference and science star are not stable because of the high value of the seeing as shown in Table 5.1.
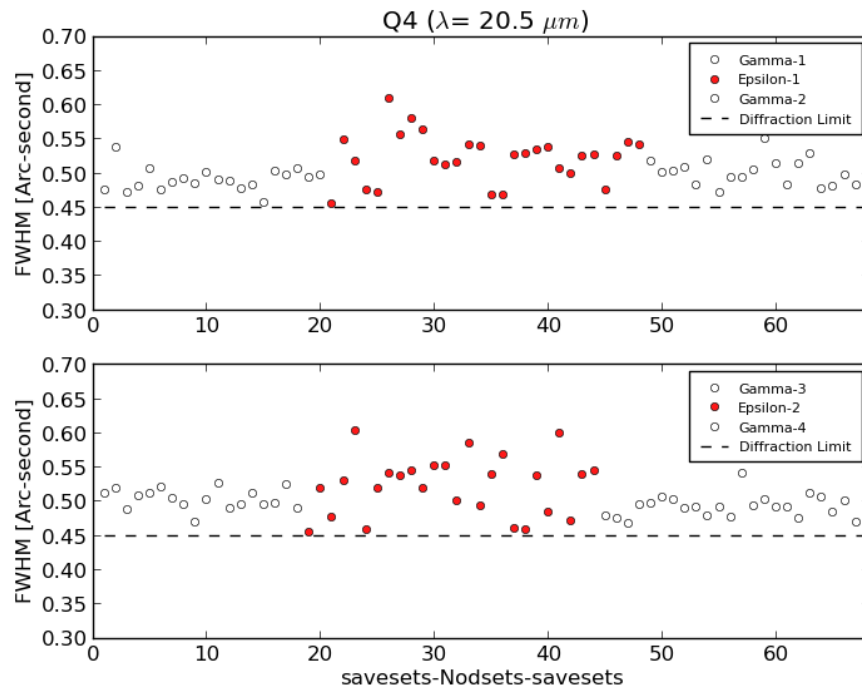


**Figure 5.7:** The figure shows the FWHM after selecting visually good and bad frames for Gamma Eridani and for Epslion Eridani. The black open circles represent the FWHM of good frames for Gamma Eridani and the red circles represent the FWHM of good nodsets for Epsilon Eridani. The dashed line represents the theoretical diffraction limit of the telescope (0.45″) in the Q4 filter.

Table 5.11 shows the average of the FWHM after the selection of good saveset frames for the reference star and good nodsets for the science star. I discarded frames using visual selection (good PSF shape) and discarded frames with values of the FWHM less than the value of the diffraction limit of the telescope (0.45″). The average of the FWHM for reference and science stars are plotted in Figure 5.8 with one sigma uncertainty.

## 5. SPATIALLY RESOLVED IMAGING OF THE DEBRIS DISK FOR EPSILON ERIDANI

**Table 5.11:** FWHM measurements selected by visual.

| Object | Total Time [Sec] | No. of Select | Percentage[%] | FWHM [″] |
|--------|------------------|---------------|---------------|----------|
| GammaEri. | 103 | 20(savesets) | 62.50 | 0.490 ± 0.004 |
| EpsilonEri. | 577.98 | 28(nodsets) | 77.78 | 0.522 ± 0.006 |
| GammaEri. | 103 | 20(savesets) | 62.50 | 0.499 ± 0.006 |
| GammaEri. | 93 | 18(savesets) | 56.25 | 0.503 ± 0.003 |
| EpsilonEri. | 557.34 | 27(nodsets) | 71.05 | 0.523 ± 0.008 |
| GammaEri. | 124 | 24(savesets) | 75 | 0.491 ± 0.003 |
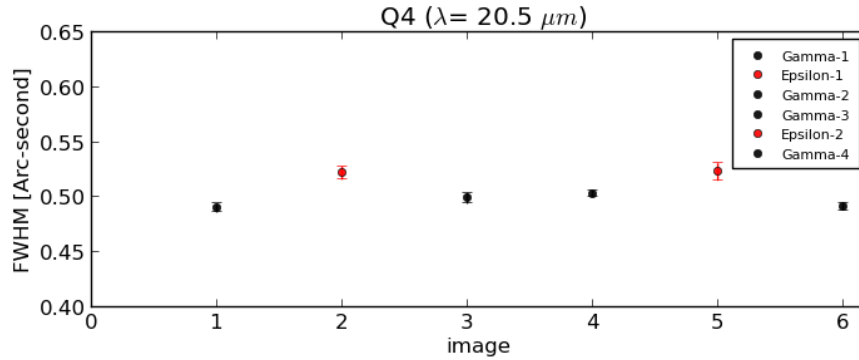


**Figure 5.8:** Black circles show the average of the FWHM with 1 sigma uncertainty for Gamma Eridani (reference star). Red circles show the average of the FWHM with 1 sigma uncertainty for the Epsilon Eridani (science star).

The same procedure have followed for Epsilon Eridani data which was used to resolve other debris disk and described in chapter 4 (equation 4.1). This procedure uses a statistical method called a Student t-test for the values that have unknown and unequal variances (Moerchen *et al.*, 2010). The FWHM values for reference and science stars are changing very fast in the MIR observation because of the seeing. Therefore, this method is very suitable to compare the FWHM of the reference and science star during the observation. The result of if the disk is resolved or not for both observations of the science star (Epsilon Eridani) with the four observations of the reference star (Gamma Eridani) is shown in Table 5.12.

Table 5.12 shows that the disk is resolved with only two observations Gamma-1 and

Gamma-4 for Epsilon Eridani-1 while unresolved using Gamma-2 and Gamma-3. The same case for Epsilon Eridani-2 which is resolved with only two observations Gamma-1 and Gamma-4 for Epsilon Eridani-1 and unresolved using Gamma-2 and Gamma-3. This is caused by the seeing, which is clearly worse (1.54″ during the first observation of Epsilon Eridani than for the second observation of Epsilon Eridani (1.2″, see Figure 5.7), which leads to a decrease of the quality of the PSF in the first case.

| Calibrator | $\mathrm{FWHM_{sci}}$ - $\mathrm{FWHM_{ref}} \geq 3\sigma_{\mathrm{ext}}$ | Resolved |
|---|---|---|
| **Epsilon-1** | | |
| Gamma-1 | $0.032 \geq 0.020$ | Y |
| Gamma-2 | $0.023 \leq 0.025$ | N |
| Gamma-3 | $0.019 \leq 0.020$ | N |
| Gamma-4 | $0.031 \geq 0.023$ | Y |
| **Epsilon-2** | | |
| Gamma-1 | $0.033 \geq 0.029$ | Y |
| Gamma-2 | $0.024 \leq 0.028$ | N |
| Gamma-3 | $0.020 \leq 0.025$ | N |
| Gamma-4 | $0.032 \geq 0.026$ | Y |

**Table 5.12:** The table shows which observation for Epsilon Eridani are resolved after applying Student t-test (Moerchen *et al.*, 2010) criteria.

The diameter of the debris disk is measured by taking the quadratic subtraction of the mean FWHM of the science from the mean FWHM of the references stars as described in equation 4.3 The radius of the debris disk in the Q4 filter is estimated by assuming that the distance of the star is 3.2 pc (Backman *et al.*, 2009) as shown in Table 5.13.

| Calibrator | $D_{\text{Disk}}$ [$''$] | Disk radius in[AU] |
|---|---|---|
| **Epsilon-1** | | |
| Gamma-1 | 0.18 ± 0.02 | 0.3 |
| Gamma-4 | 0.18 ± 0.03 | 0.3 |
| **Epsilon-2** | | |
| Gamma-1 | 0.17 ± 0.02 | 0.3 |
| Gamma-4 | 0.17 ± 0.01 | 0.3 |

**Table 5.13:** The radius of the debris disk around Epsilon Eridani in Q4 filter.

## 5.5  MIR Data Reduction

The iDealCam have used for stacking good the selected frames since the code has the ability to find the centroid of the frames and stacking them together. The final image is shown in Figure 5.9 as we see there are two negative PSFs and one positive. The final image shows three different patterns in the background. The pattern of the background in the first negative PSF (Frame-1) is different from two the others frames (Frame-2) and (Frame-3).

This pattern is repeated in the final images for the two observations of Epsilon Eridani and has less effect on the final images for the four observations of Gamma Eridani. This means that the pattern could come from the atmospheric effects, or because the science target is a faint source comparing with reference star, or might be something happened to the detector during the observation.
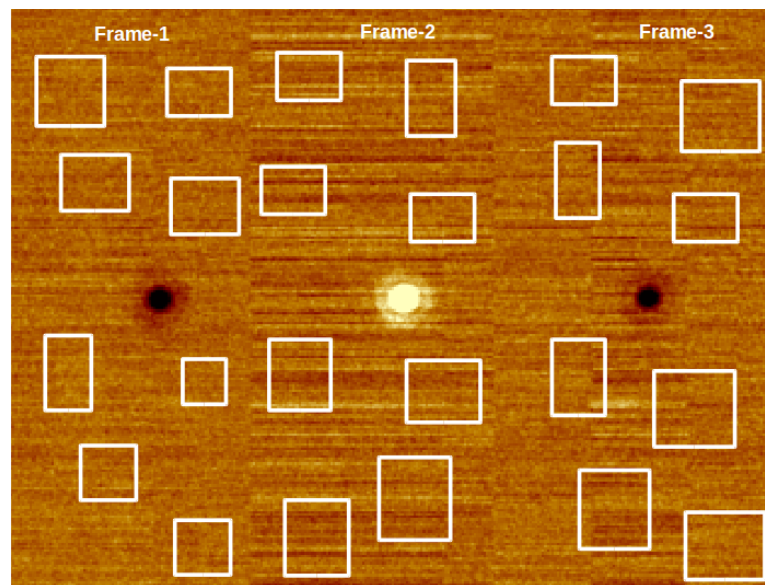


**Figure 5.9:** The final image for the science (Epsilon Eridani). The image consists of two negative and one positive PSF. The white boxes are selected randomly to calculate the mean of counts inside these boxes.

Different techniques have applied to reduce the noise caused by the atmosphere in the image and to remove the strap pattern in the positive PSF. The positive PSF is more important for us than the two negative since it represents the real light coming from the source and reaching the telescope.

## 5. SPATIALLY RESOLVED IMAGING OF THE DEBRIS DISK FOR EPSILON ERIDANI

The first technique for reducing the background noise is to divide the image into three frames (Frame-1, Frame-2, Frame-3) and to maker small boxes with different sizes in the each frames (as shown in Figure 5.9) then calculate the mean of the photons inside those boxes. The next step is to calculate the standard deviation of the mean values insides the boxes and then take the sum of the standard deviations from all boxes to subtract from the whole frame. This technique is used to reduce the background noise and to get smoother radial profiles for the image.

The second technique is used to remove stripes in frame-2. I have done that by taking the average of the first 10 pixels from the left of frame-2 in each row and subtracted the value of the average from each row in frame-2. The result of using this technique is shown in Figure 5.10.
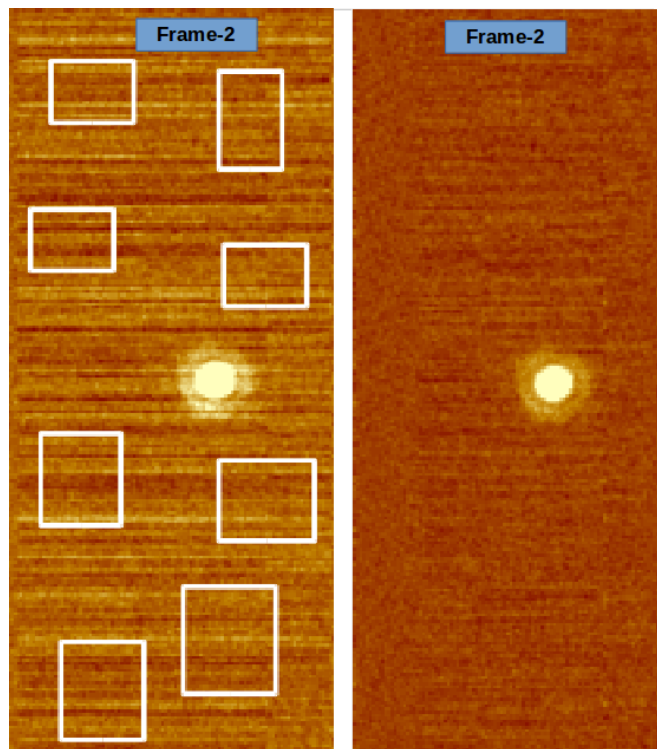


**Figure 5.10:** The left image represents frame-2 before removing stripes and the right image represents crop frame-2 after removing the stripes pattern with technique described in the text.
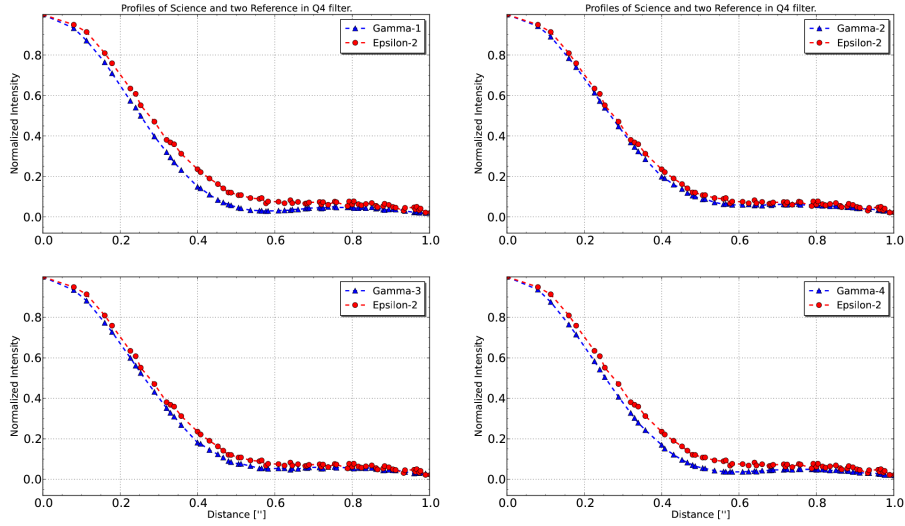
# 5.6   Radial Profiles

The azimuthal radial profile of the PSF distribution was plotted for the final images of Epsilon Eridani and Gamma Eridani after the flux intensity of the image have normalized to one as shown in Figure 5.11. The red dotted line represents the radial profile of Epsilon Eridani for the two observations in the Q4 filter and the blue dotted line represents the radial profiles of Gamma Eridani for the four observations in the Q4 filter.

The first four plots in the subfigure (a) 5.11 show the radial profile of Epsilon Eridani for the first observation with the red dotted line compared with radial profiles of Gamma Eridani for the four observations (blue dotted line). The second four plots in the subfigure (b) 5.11 show the radial profile of Epsilon Eridani for the second observation (red dotted line) compared to the radial profile of Gamma Eridani.



(a)
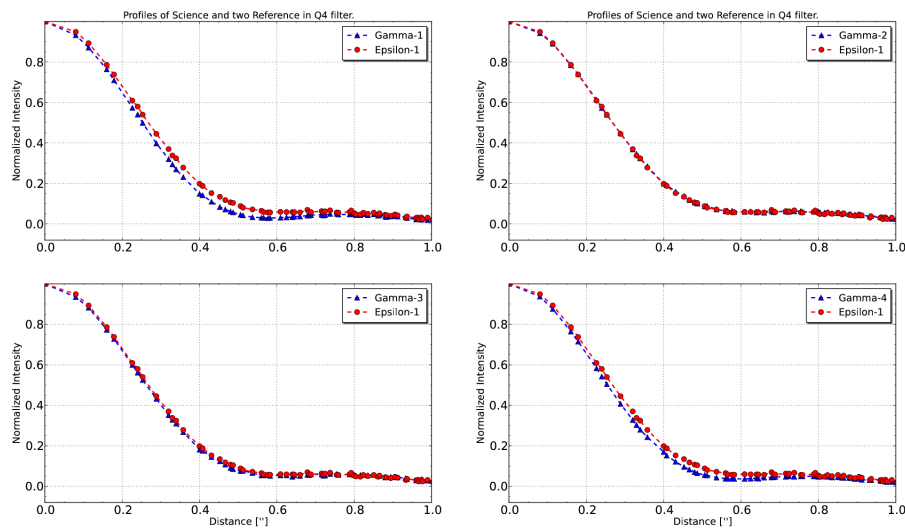
**(b)**

**Figure 5.11:** The red dotted line represents the radial profile of the final image for Epsilon Eridani-1,2 and the blue dotted line represents the radial profile of the final image for Gamma Eridani-1,2,3,4.

## 5.7   Disk Model

I have created a synthetic model of the disk to compare it with my result. The model of the disk is based on the calculation of the temperature gradient of the disk. The disk is irradiated by the light from the star and re-emit it again as a black body. The equation of the black body radiation at specific temperature is described below and known as Planck's equation:

$$B(\lambda, T) = \frac{2hc^2}{\lambda^5} \frac{1}{e^{\frac{hc}{\lambda k T}} - 1} \qquad (5.2)$$

where c is the speed of light, h is the Planck constant, k is the Boltzmann constant, $T$ is the temperature, $\lambda$ is the wavelength and B is the flux density. The temperature of

the disk at a specific distance from the star can be calculated using the follow equation:

$$T(r) = T_0\left(\frac{r}{r_0}\right)^{-q} \tag{5.3}$$

where $r_0$ is the reference radius (e.g, 1 AU), $T_0$ is the temperature at $r_0$ and q is the power law of the temperature.

The surface density of the disk is described in this equation:

$$\Sigma(r) = \Sigma_0\left(\frac{r}{r_0}\right)^{-p} \tag{5.4}$$

$\Sigma_0$ is the initial surface density of the disk in $g/cm^2$ and p is the power law of the density.

The result of the disk model is shown in Figure 5.12. I have used a face on narrow ring with radius between 0.5 - 2.5 AU and the flux of the star and the disk are estimated from Backman *et al.* (2009) at 20.5 $\mu m$. The photospheric flux of the star is $F_{star} = 2.18$ Jy and the excess flux of the disk $F_{ex} = 0.286$ Jy.
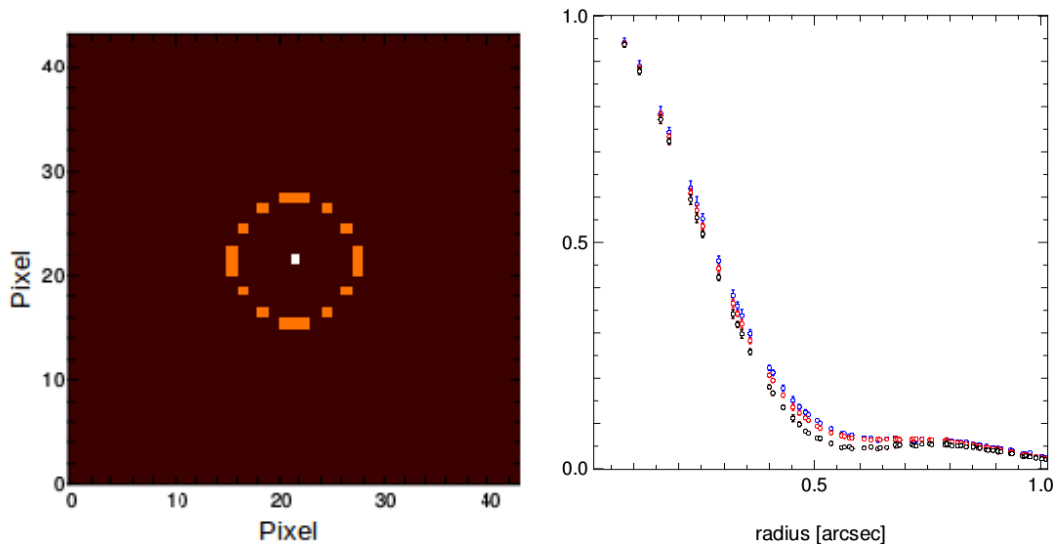


**Figure 5.12:** The left figure represents the model of the disk for Epsilon Eridani and the disk radius is set in this case to 1.4 AU. The right plot represents profiles of the PSF reference in black, the synthetic model in red and the science target in blue.

The synthetic model of the disk have convolved with the final normalized PSF of Gamma Eridani and then compared it to the final image of Epsilon Eridani. The radial profiles of the model, synthetic model, and science are shown in right plot in Figure 5.12.

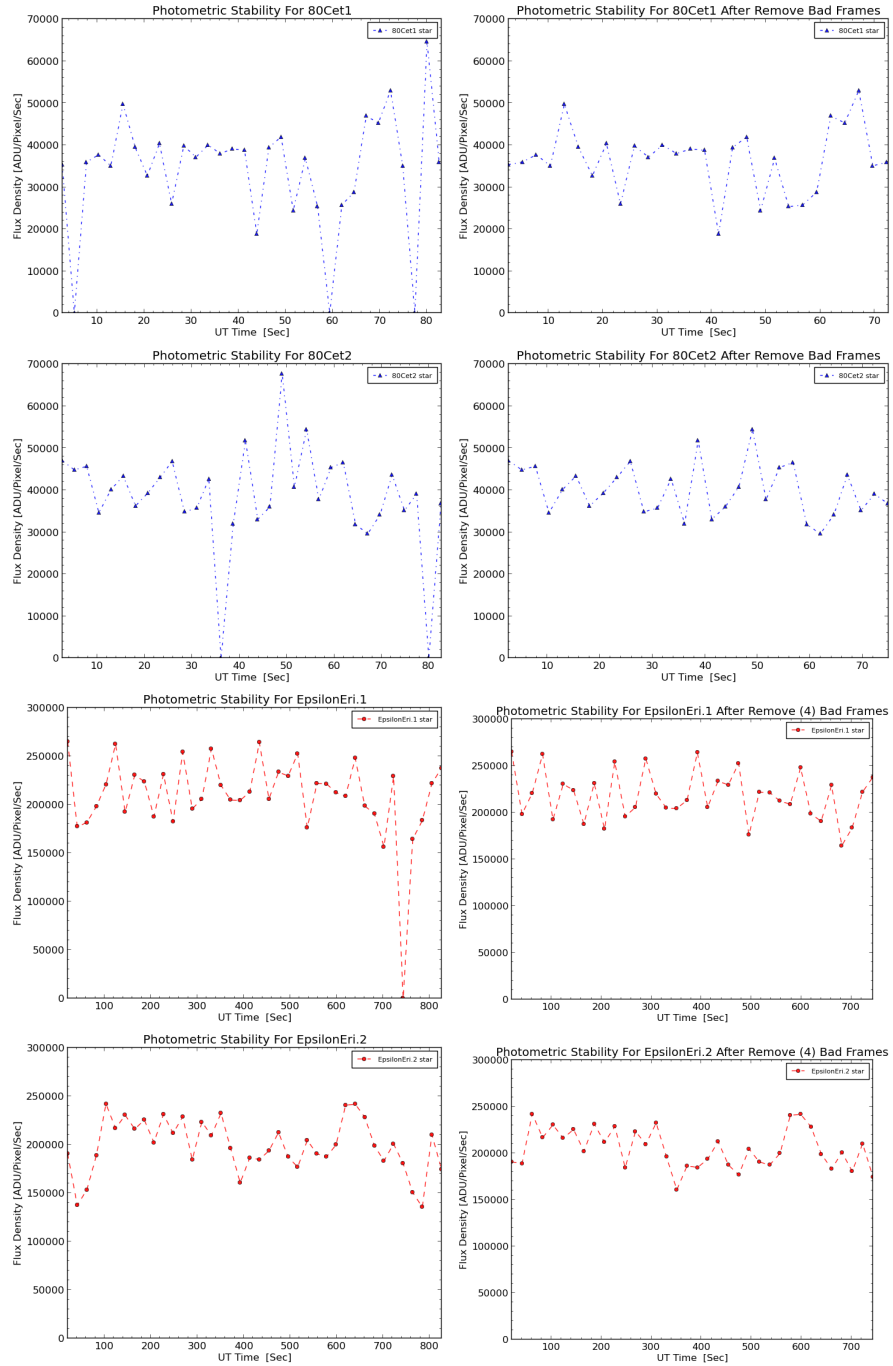## 5.8   Photometry Measurements for Epsilon Eridani

Photometry measurements are carried out using iDealCam (Li *et al.*, 2013). The circular aperture width which have used is 20 pixel for the inner circle of the flux area and 10 pixel for the background area, separated by 10 pixel, where one pixel corresponds to 0.08″. The possible disk emission extent for the science has to be included in the aperture therefore the flux area is selected to be large (1.6″ in radius). For matching, the same aperture value have selected for the two reference stars 80 Cet and Gamma Eridani. The figure below (5.13) shows the flux variation during the observation for both reference stars (80 Cet, Gamma Eridani) and the change of the flux for the science target (Epsilon Eridani).

The first four plots represent the photometry measurements for the reference star 80 Cet. The plots are before and after removing some frames which have zero flux measurements. The blue dotted line represents the photometry measurements for the science target before and after removing bad frames. There are two reference stars have used to calibrate the science star and the final values of the flux calibration in Jy is shown in Figure 5.14.

The relation between the change of air mass during the observation and flux value is very clear in Figure 5.14. The maximum value of the air mass during the observation was 1.55 and it reduces the flux value of both observation of science star Epsilon Eridani and Epsilon Eridani-2 to a minimum value of 2.26 Jy and 2.06 Jy, respectively. The flux measurements of Epsilon Eridani after calibrating them with two calibration stars are much larger than the flux measurements of Epsilon Eridani-1 after being calibrated with the same calibration stars as shown in the left of Figure 5.14.

This comes mainly from the change of the air mass during the observation. The average of the flux value have calculated for Epsilon Eridani-1 and Epsilon Eridani-2 and the final flux value is 2.49 Jy. The uncertainty of the flux is estimated as the standard deviation of the science flux for the average of the two observations of Epsilon Eridani and it is 7%. The flux value is very comparable with prior flux measurements

from Spitzer space telescope which is 2.48 Jy (Backman *et al.*, 2009).
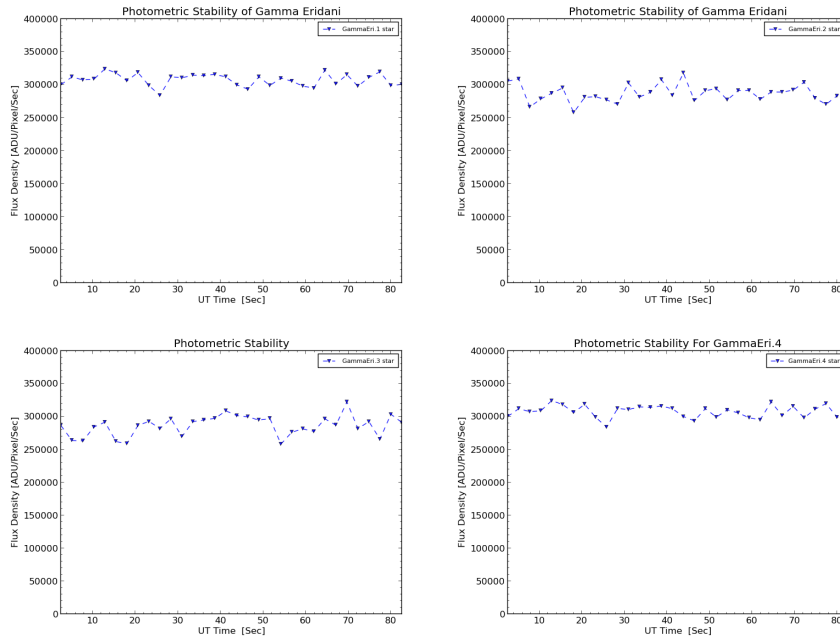
**Figure 5.13:** The figure shows the photometry measurements for both reference stars and the science star. The blue dotted line represents the two reference stars 80 Cet and Gamma Eridani. The red dotted line represents the science star Epsilon Eridani.
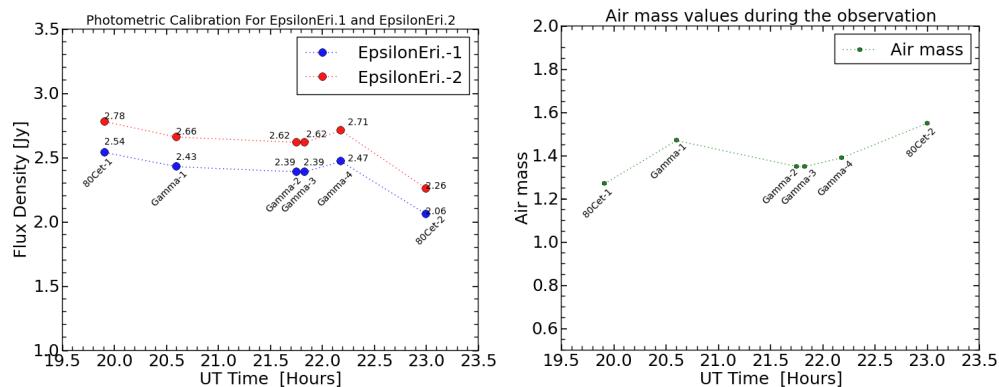


**Figure 5.14:** The left plot shows the final result of the photometry calibration of the two observations of Epsilon Eridani (1 in the red dotted line and 2 in the blue dotted line) using the reference star Gamma Eridani and reference star 80 Cet. The right plot shows the air mass in the green hexagon dotted line changing during four observations for Gamma Eridani and two obervations for 80 Cet.

# 6

# Conclusions and Prospects

## 6.1  Introduction

In his thesis I analyzed observational data of the circumstellar disk around HD 179218 and Epsilon Eridani. Two targets have been observed using one of the biggest telescopes GTC with the diameter of 10 m / CanariCam instrument at MIR wavelength. The MIR imaging for both targets and the spectrum of one target were acquired, analyzed, and compared with the theoretical model.

The measurements of the angular size of two targets are close to the diffraction limit of the GTC telescope. Therefore, different techniques have used for checking the PSF of each savesets carefully and to reduce the data in a very precise way.

In this chapter, I summarized and discussed the results of analyzing observational data in chapters 4 and 5 where the structure, composition, and the dust properties studied for HD 179218 and the origin dust particles in Epsilon Eridani.

## 6.2  Characterization of the Pre-transitional Disk for HD 179218

High angular resolution imaging has been achieved using a ground-based telescope GTC to observe HD 179218 in different three filters PAH1(8.6 $\mu m$), PAH2(11.3 $\mu m$), and Si6(12.5 $\mu m$). This is the first time that HD 179218 has been observed in the PAH filter using GTC telescope. A successful method of observation has been applied by observing two different calibration stars (HD 169414, HD 187642) before and after the science star HD 179218 (target). This technique of observation is better than using the

## 6. CONCLUSIONS AND PROSPECTS

same calibration star before and after the science star, since it adds more accuracy to the photometry calculation, PSF comparison, and spectroscopy calibration. The average of the seeing during the observation is between (0.42 - 0.60) arcsec which helps me to gain a very stable PSF for most of savesets. According to the (Dan Li, 2010) study of the MIR observations from Gemini observatory, using two fitting models (Gaussian and Lorentzian) to fit the PSF of the data, there is no different between Gaussian and Lorentzian profile in the central part of the PSF.

Therefore, I used Lorentzian fit to measure the FWHM of each saveset of two calibration stars and science star. To avoid the misalignment of savesets through the stacking process and also the uncertainty that produced through the moving of the telescope to make a chop procedure, it is advisable to take measurements of each saveset instead of nodsets. Moreover, the integration time for each saveset is 2 seconds for the calibration and science star.

A statistical method have applied to resolve the disk around HD 179218. This method has been used successfully by other researchers to resolve the circumstellar disks Honda *et al.* (2012); Mariñas *et al.* (2011); Moerchen *et al.* (2010). The statistical measurements of the FWHM for the science star and two calibration stars show that there is extended thermal emission around the science star comparing with other two calibrators in the PAH1 and PAH2 filters. While there is no emission around the science star at 12.5 $\mu m$ after comparing it with the second calibrator star, the observation of the first calibrator star was discarded due to the poor optical seeing ($> 1''$).

The uncertainty of the FWHM measurements for a large number of savesets of both calibration and science stars is 3 sigma. The value of the uncertainties is gained after checking all savesets visually and discarding the saveset that has a bad PSF (elongation PSF) or a value of FWHM less than the diffraction limit of the telescope $0.19''$, $0.25''$ and $0.27''$ in the three filters PAH1, PAH2 and Si6, respectively.

The radius of the disk around HD 179218 in the PAH bands is measured between (12 - 14 AU), by assuming the distance of the star d = 290 pc, and it is shown in Table 4.5. The distance of the star is derived from the GAIA archive measurements approximately $3.41 \pm 0.3$ mas, which is estimated to have the average value of 290 pc. This value is used for calculations instead of other distance value d=240 pc used in other literature. This value of the radius is corresponding to the previous measurement by using interferometry technique Fedele *et al.* (2008).

Similar studies have used PAH to detect the emission and measure the size of the disk around Herbig stars. The PAH filter at 8.6 *μm* has been used by Lagage *et al.* (2006) to measure the size of the protoplanetary disk around HD 97048 and characterized the diameter of disk to be 0.26″. The same target HD 97048 observed in the PAH filter at 11.2 *μm* by Maaskant *et al.* (2014) who estimated the diameter of the disk to be 0.64″. If the distance of the star is assumed to be 180 pc the disk radius in the two filters PAH1, PAH2 is 23 AU and 57 AU, respectively.

The process of the re-centering and stacking good savesets to get the final image has been applied in a very precise way to avoid an increase in the FWHM of the final image. This process is achieved by minimizing the differences between the radial brightness profile for each saveset and the center of the initial reference saveset with an accuracy of one-fifth pixel. The results of this operation show that the value of FWHM for the final image tends to be comparable to the value of statistical FWHM in the three filters as shown in Figure 4.3 and in Table 4.6.

Photometry calculations have been done for the HD 179218 by using the iDeal-Cam software. The HD 179218 is calibrated with two references stars (HD 168414, HD 187642) from Cohen photometric standard stars. The results of the photometric calibration for HD 179214 in the three filters are summarized in Table 4.10. The results of the photometric measurements of the system in three filters is matching with flux densities in the previous data by Fedele *et al.* (2008) and Juhász *et al.* (2010).

Additionally, the low-resolution spectrum of the HD 179218 has been reduced using the RedCan pipeline for the CanariCam instrument, and also the GTC spectrum has been scaled to match the spectra of the same source from different space telescopes ISO and Spitzer (Acke and van den Ancker, 2004; Fedele *et al.*, 2008), respectively.

The CanariCam spectrum of the HD 179218 is similar to the shape of the spectrum from the space telescopes ISO and Spitzer, with the detection of different features identified in earlier observations as shown in Figure 4.7. The influence of Earth ozone band between (9.3 - 9.9 *μm*) is very obvious in the CanaraiCam spectrum using ground-based telescope comparing with the spectrum of the same source using two space telescopes ISO and Spitzer. The rescaled spectrum of HD 179218 is also comparable with the photometric measurement values in the two filters 8.6 *μm* and 12.5 *μm*, and less comparable at 11.3 *μm* (green circles) as shown in Figure 4.7.

# 6. CONCLUSIONS AND PROSPECTS

The same successful have followed procedure that has applied by (Honda *et al.*, 2012) to model the pre-transitional disk around HD 169142 in the Q-band. The radiative transfer code (RADMC3D) have used to fit the SED of HD 179218 with the observational SED from Acke and van den Ancker (2004) and to fit the radial profile of the synthetic image in the continuum emission with an unresolved observational profile at 12.5 $\mu m$ filter. The mineralogy of the model is based on the Fedele model which is used to fit the MIR observations from VLTI by assuming an inner disk and outer disk separation with a gap for HD 179218 system (Fedele *et al.*, 2008).

The inner radius of the inner disk is determined to start at 1.1 AU to fit the dust sublimation according to the stellar parameters used to fit the observational SED (Alecian *et al.*, 2013). The outer radius of the inner disk is tested by changing the size of the radius between (3 - 5)AU and the power law of surface density between (-2 , 2) to fit the SED, where I found that there is a little impact by changing the power law and the size of the disk in the NIR region between (2 - 3 $\mu m$) for the SED. While there is no influence on the radial profile of the brightness at 12.5 $\mu m$ and two other filters 8.6, 11.3 $\mu m$.

The inner disk chemical composition is considered to be a mixture of the carbon grains and amorphous silicate with the percentage of the population between (10 - 90 %), respectively. The scale height and the flaring index of the inner disk have no influence on the MIR of the radial profile brightness. The applied mass to fit the inner disk is nearly 0.002 M⊙.

The size of the gap is estimated to be $\sim$ 7 AU with a very low mass in the gap (to support the idea of the planet form) $\sim 2 \times 10^{-11}$ M⊙. The same chemical composition of the dust grains in the inner disk is used also for the gap to fit the SED and the radial profile of the brightness at 12.5 $\mu m$. There is no influence for the power law of the surface density and scale height of the gap on the radial profile of the brightness, similar to the case of the inner disk.

The most of the MIR emission of HD 179218 comes from the outer disk is mentioned by many researchers Dominik *et al.* (2003); Fedele *et al.* (2008); Liu *et al.* (2007). The outer disk is assumed to have 90 % amorphous of silicate and 10% the crystalline enstatite as a chemical composition of the dust grains. I analyzed a varing of the three parameters in the outer disk, which are the power law between (-2, 2), the inner radius size between (8 - 12 AU) and the outer disk size between (30 - 150 AU).

The result of this analysis is summarized in Table 4.21 with the value of the non-reduced Chi-square to fit the SED as the function of three parameters and with also the models of the radial profile of the brightness that are resolved or unresolved at 12.5 $\mu m$. I found the inner radius of the outer disk has a significant influence on the radial profile brightness at 12.5 $\mu m$ and on the SED particularly in the MIR to sub-mm wavelengths.

The small size of the outer disk 30 AU and the positive value of the power law do not fit the SED and the radial profile of the brightness is resolved at 12.5 $\mu m$. Whereas, for the large size of the outer disk such as 150 AU and with the negative value for the power law less emission of the flux in the FIR and sub-millimetre are produced. The best parameters are determined to fit the SED and the radial profile of the brightness in the continuum emission are listed in Table 4.12. Figure 4.22 shows that the model of the spectral energy distribution is fitted very well with the whole observational SED from (Acke and van den Ancker, 2004).

The synthetic images in three wavelengths 8.6, 11.3, and 12.5 $\mu m$ are produced by using the best-fit parameters in Table 4.12. Those images are convolved with the PSF of the calibration image and then are compared with the observational radial profile of the science as shown in Figure 4.25.

The radial profile of science is spatially resolved respect to the two radial profiles of the calibrator stars and two radial profiles of the convolved synthetic image in the PAH filters (8.6, 11.3 $\mu m$). At the contrary, the radial profile of the science in the silicate filter shows no difference with the radial profile of the second calibrator star and radial profile of the convolved synthetic image. Also, the first calibrator star in the silicate filter is discarded from calculations because of the poor seeing. This means there is no detectable continuum emission around HD 179218 by using GTC telescope at 12.5 $\mu m$.

The observation data and the radiative transfer model for HD 179218 suggested that the resolved emission around the star is not naturally thermal but it originates from the closed region to the outer disk surface, Since of the UV of the star is excited the PAH molecules in that area. This emission is responsible for spectral energy features at 8.6 and 11.3 $\mu m$ as shown in Figure 4.7. Moreover, the radiative transfer model and the observation data propose that most of the mass is found in the first 30 AU of the outer disk and the power law of the outer disk is p = -1.5, which does not agree with the model assumed by (Dominik *et al.*, 2003).

# 6. CONCLUSIONS AND PROSPECTS

The same fitting process above was applied for the SED and for the image model with less luminous star than the Alecian model, and the stellar parameters are obtained from Dominik *et al.* (2003). The SED fitting for the less luminous star is represented in Figure 4.24, and the fitting of the raidal profile for the model with observation is shown in Figure 4.25. The implemented parameters to get the SED and the synthetic images are listed in Tables 4.13.

Finally, the origin of the PAH emission around HD 179218 have compared with other two Hebig stars HD 97048 and IRS 48 in the sections 4.10 and 4.11. The first concludes from this comparison that the PAH emission around HD 179218 is resolved in the outer disk surface and this is similar to the case of HD 97048. Then, it found that the size of the PAH emission for HD 97049 is ($\sim$ 40 AU) larger than the size of the emission around HD 179218 ($\sim$ 15 AU). However, HD 179218 is ( d = 290 pc) two times far away from us than HD 97048 (d = 180 pc).

The second concludes is that the charge state of the PAH emission for the HD 179218 is ionized PAH and this comparable to the case IRS 48. Therefore, there are two possible explanations for the ionized PAH emission around HD 179218. The first explanation is that the stellar luminosity of HD 179218 (L = 180 $L_{\odot}$) is significantly larger than that of the other four Herbig stars in the Maaskant *et al.* (2014) study where the stellar luminosity of HD 97048 (L = 40 $L_{\odot}$), HD 169142 (L = 10 $M_{\odot}$), HD 135344 (L = 10 - 15 $M_{\odot}$) and IRS 48 (L = 14 $M_{\odot}$). The central star produces a strong UV-radiation field that is able to ionize the PAH molecules in the large distance from the outer disk. Another explanation could be that a wide-angle wind in HD 179218 is hitting the outer disk surface which led to ionization of the PAH in the outer region of the disk.

# 6.3 Spatially Resolved Imaging of the Debris Disk for Epsilon Eridani

I obtained MIR observations for Epsilon Eridani star on the $6^{th}$ of January 2013 by using GTC telescope / CanariCam instrument in the Q4 filter. The sequence of the observation for Epsilon Eridani is done by observing the calibration star (Gamma Eridani) before and after science star (Epsilon Eridani). The stability and shape of the PSF during the observation are very important quantities in order to characterize the quality of the image. Therefore, I have examined more than 700 savsets to understand the behaviour of the PSF and to characterize the effect of the seeing, humidity, and air mass on the PSF. The iDealCam code has been used to read out and measure the FWHM for each savesets for calibration and science star by using Lorentzian fit.

The bad observation condition is very obvious on the MIR data, where the optical seeing value is ($> 1''$) during the observation which effects the PSF shape. Basically, the calibration star is brighter than the science star, so the influence of the bad seeing has less effect on the PSF of the savesets for calibration star than the PSF of the saveset for the science star.

As a consequence of the bad seeing and the faint science target, the FWHM measurements of the science target show unstable values during the observation therefore more than half of the FWHM values are less than the diffraction limit of the telescope, as shown in Figure 5.2. The FWHM measurements of the calibration star has more stability values during the observation than the one of the science star even with optical seeing values larger than ($1''$).

Different techniques have been applied to examine the data and to gain the best result from these data. The saveset of the calibration stars does not have a value of the FWHM measurement less than the diffraction limit of the telescope comparing with science saveset as shown in Figure 5.2. Therefore, the first step is discarding the saveset that has a value of the FWHM measurements less than the diffraction limit of the telescope $0.45''$ in the Q4 filter. Consequently, the number of the savesets for the science star is reduced from 320 savesets to 99 savesets for Epsilon Eridani-1 and from 320 savesets to 85 savesets for Epsilon Eridani-2, while the total numbers of savesets of the calibration stars for four observations (Gamma Eridani-1,2,3,4) remains 32 savesets.

Consequently, approximately 74% of the savesets for the science have removed from the total data because it has a value of the FWHM less than the diffraction limit of the telescope. I applied another criterion to select a good and bad saveset from 99 and 85 science savesets and 32 calibration savsesets by calculating the mean of the FWHM measurements then chose the saveset which has a value of the FWHM in the range FWHM$_{average}$ $\pm$ 1$\sigma$, 2$\sigma$, and 3$\sigma$ as shown in Figure5.3.

Furthermore, another technique have performed to check the FWHM measurements. This technique is dependant on the measured FWHM for each nodeset instead of the saveset for the science star because the shape of the PSF for each nodeset is better than the saveset as shown in Figure 5.5. The total number of the nodesets for the science is 38 nodsets, there are only two nodeset out of 38 nodesets that have been removed for Epsilon Eridani-1 observations since they have a value of the FWHM less than the diffraction limit of the telescope. Then I used the same procedure which is applied to select a good saveset by selecting the nodsets which has a value of the FWHM in the range FWHM$_{average}$ $\pm$ 1$\sigma$, 2$\sigma$, and 3$\sigma$ for nodesets of the science, shown in Figure 5.6.

The results of selection of a good nodeset for the science and comparing it with a good saveset of the calibration star are listed in Tables 5.7, 5.8 and 5.9. The disk is only resolved in this technique within 1 sigma criterion. The shape of the PSF should be considered to measure the quality of the image. Therefore, I have examined each nodeset visually for the science target and each saveset for the calibration star. The visual selection of good frames adds more accuracy to the result because some of the PSFs have elongated shape which should not be included in measurements. The final result of the FWHM shows that the disk is resolved after applying the same steps used by Moerchen *et al.* (2010).

The influence of the seeing is observed on the Epsilon Eridani-1 and Epsilon Eridani-2 observations where the optical seeing value is > 1.5 arcsec. Due to that, the disk is unresolved for Epsilon Eridani-1 and Epsilon Eridani-2 observations with Gamma-2 and 3 observations, but it is resolved with Gamma-1 and 4 observations. The disk is resolved with 3$\sigma$ uncertainty and the radius of the disk is measured to be 0.3 AU and they are listed in Table 5.12. In spite of the bad optical seeing value during the observation and a faint object, I was able to resolve the disk partially with 3$\sigma$ significance and by using different techniques to examine the PSF. The radius of the disk is smaller than what was expected from modelling of the system (2.6 AU by (Backman

*et al.*, 2009)).

Epsilon Eridani can be a good example to study the disk interaction near the habitable zone of the planet system. The Jovian planet in the habitable zone has been detected at the distance of 3.2 AU Hatzes *et al.* (2000). There are two scenarios for the dust existence in this system. Brogi *et al.* (2009) assumed that the origin of the dust must be an asteroid belt such as a ring of the planetesimals inside the orbit of the planet otherwise the planet would have prevented dust to reach the detected region. Another scenario by Reidemeister *et al.* (2011) claims that the planet does not block the small particles of the dust to spiral inwards due to Poynting-Robertson drag, therefore the dust origin may come from the outer regions of the debris disk. This scenario is the preferable scenario for the origin of the dust particles in a very close region to the star and the result confirms the previous conclusion by using VLT/VISIR observation for the same target in 18.7 $\mu m$.

## 6.4   Prospects

There are many questions to be answersed when studying the protoplanetary disk, debris disk, and planet evolution. In the first project, several puzzles still without clear answers about the PAH emission in the Herbig stars such as: What is the relation between the PAH in the disk and the gap?, what is the influence of other gas molecules or dust particles on the PAHs? Can we find ionized PAH in the outer disk like the case HD 179218 and what is the interaction between PAH and other materials in the disk? and so on.

In the second project, the debris disk around Epsilon Eridani is not completely clear. Is the dust located at the same distance as the planet?, what are the properties of the dust grains close to the habitable zone around the star? and what is the influence of the planet on the disk? How often can debris disk be observed around main-sequence star? and so on. The answer to all these questions in future will allow us to understand the PAH spectral signatures in the protoplanetary disk structure and know more about the origin of the dust particles around Epsilon Eridani.

The new generation of the telescopes, instruments and definitely robust observations would lead us to understand more specifically about the environment of the young stellar objects. Therefore, investigate the structure and chemistry of circumstellar disks is possible with a new generation of ground-based telescopes like Atacama Large Millimeter Array (ALMA), Extremely Large Telescope (ELT), Thirty Meter Telescope (TMT) or space telescopes like James Webb Space Telescope (JWST), Space Infrared Telescope for Cosmology and Astrophysics (SPICA), which offer high sensitivity, high spatial and spectral resolution.

Additionally, the interferometric MIR instruments such as VLTI / Multi Aperture mid-Infrared SpectroScopic Experiment (MATISSE) or the Large Binocular Telescope (LBT) will provide us better angular resolution at similar or better sensitivity, which allows us to observe a large sample of more distant objects. Finally, recent advancements in the radiative transfer and hydrodynamic model codes have made the disk models more powerful in generating the physical and chemical processes.

# References

Absil, O. and Mawet, D. (2010). Formation and evolution of planetary systems: the impact of high-angular resolution optical techniques. *A&A Rev.*, **18**, 317–382. 2

Absil, O., di Folco, E., Mérand, A., and Augereau (2006). Circumstellar material in the Vega inner system revealed by CHARA/FLUOR. *A&A*, **452**, 237–244. 24

Absil, O., Defrère, D., Coudé du Foresto, V., and Di Folco (2013). A near-infrared interferometric survey of debris-disc stars. III. First statistics based on 42 stars observed with CHARA/FLUOR. *A&A*, **555**, A104. 24

Acke, B. and van den Ancker, M. E. (2004). ISO spectroscopy of disks around Herbig Ae/Be stars. *A&A*, **426**, 151–170. 49, 66, 71, 77, 123, 124, 125

Acke, B., Min, M., van den Ancker, M. E., and Bouwman (2009). On the interplay between flaring and shadowing in disks around Herbig Ae/Be stars. *A&A*, **502**, L17–L20. 48

Acke, B., Bouwman, J., Juhász, A., Henning, T., van den Ancker, M. E., Meeus, G., Tielens, A. G. G. M., and Waters, L. B. F. M. (2010). Spitzer's View on Aromatic and Aliphatic Hydrocarbon Emission in Herbig Ae Stars. *ApJ*, **718**, 558–574. 94

Alecian, E., Wade, G. A., Catala, C., Grunhut, J. H., Landstreet, J. D., Böhm, T., Folsom, C. P., and Marsden, S. (2013). A high-resolution spectropolarimetric survey of Herbig Ae/Be stars - II. Rotation. *MNRAS*, **429**, 1027–1038. 70, 71, 82, 124

Allen, E. and Triantaphillidou, S. (2012). *The Manual of Photography and Digital Imaging*. CRC Press. 32, 33

Andre, P., Ward-Thompson, D., and Barsony, M. (1993). Submillimeter continuum observations of Rho Ophiuchi A - The candidate protostar VLA 1623 and prestellar clumps. *ApJ*, **406**, 122–141. 7, 8

Andrews, S. M., Wilner, D. J., Espaillat, C., and Hughes (2011). Resolved Images of Large Cavities in Protoplanetary Transition Disks. *ApJ*, **732**, 42. 67

## REFERENCES

Anglada-Escudé, G., Amado, P. J., Barnes, J., and Berdiñas, Z. M. (2016). A terrestrial planet candidate in a temperate orbit around Proxima Centauri. *Nature*, **536**, 437–440. 1

Armitage, P. J. (2010). *Astrophysics of planet formation*. Cambridge University Press. 12, 26

Aumann, H. H., Beichman, C. A., and Gillett, F. C. (1984). Discovery of a shell around Alpha Lyrae. *ApJ*, **278**, L23–L27. 18, 22, 96

Backman, D. (2004). Debris Disks: An Overview. In L. Caroff, L. J. Moon, D. Backman, and E. Praton, editors, *Debris Disks and the Formation of Planets*, volume 324 of *Astronomical Society of the Pacific Conference Series*, page 9. 18, 19

Backman, D., Marengo, M., Stapelfeldt, K., Su, K., Wilner, D., Dowell, C. D., and Watson, D. (2009). Epsilon Eridani's Planetary Debris Disk: Structure and Dynamics Based on Spitzer and Caltech Submillimeter Observatory Observations. *ApJ*, **690**, 1522–1538. 97, 111, 117, 119, 128

Beichman, C. A., Bryden, G., and Gautier, T. N. (2005). An Excess Due to Small Grains around the Nearby K0 V Star HD 69830: Asteroid or Cometary Debris? *ApJ*, **626**, 1061–1069. 24

Berné, O., Joblin, C., Fuente, A., and Ménard, F. (2009). What can we learn about protoplanetary disks from analysis of mid-infrared carbonaceous dust emission? *A&A*, **495**, 827–835. 14

Bjorkman, J. E. and Wood, K. (2001). Radiative Equilibrium and Temperature Correction in Monte Carlo Radiation Transfer. *ApJ*, **554**, 615–623. 67

Bodenheimer, P. (2011). *Principles of star formation*. Springer Science & Business Media. 6

Bonfanti, A., Ortolani, S., Piotto, G., and Nascimbeni, V. (2015). Revising the ages of planet-hosting stars. *A&A*, **575**, A18. 96

Boss, A. P. (2006). Gas giant protoplanets formed by disk instability in binary star systems. *The Astrophysical Journal*, **641**(2), 1148. 25

Bouwman, J., de Koter, A., Dominik, C., and Waters, L. B. F. M. (2003). The origin of crystalline silicates in the Herbig Be star HD 100546 and in comet Hale-Bopp. *A&A*, **401**, 577–592. 47

Brogi, M., Marzari, F., and Paolicchi, P. (2009). Dynamical stability of the inner belt around Epsilon Eridani. *A&A*, **499**, L13–L16. 129

Brown, J. M., Blake, G. A., Qi, C., and Dullemond (2009). Evidence for Dust Clearing Through Resolved Submillimeter Imaging. *ApJ*, **704**, 496–502. 47

Calvet, N., D'Alessio, P., Hartmann, L., Wilner, D., Walsh, A., and Sitko, M. (2002). Evidence for a Developing Gap in a 10 Myr Old Protoplanetary Disk. *ApJ*, **568**, 1008–1016. 19, 48

CanariCam (2014). Canaricam-webpage. http://www.gtc.iac.es/instruments/canaricam/canaricam.php. 27, 29, 30, 35, 36, 38, 39, 40, 43

Carmona, A., Pinte, C., Thi, W. F., and Benisty, M. (2014). Constraining the structure of the transition disk HD 135344B (SAO 206462) by simultaneous modeling of multiwavelength gas and dust observations. *A&A*, **567**, A51. 70

Carpenter, J. M., Bouwman, J., Mamajek, E. E., Meyer, M. R., and Hillenbrand (2009). Formation and Evolution of Planetary Systems: Properties of Debris Dust Around Solar-Type Stars. *ApJS*, **181**, 197–226. 21

Carroll, B. and Ostlie, D. (2007). *An Introduction to Modern Astrophysics*. Pearson Addison-Wesley. 4, 5, 6

Charles M. Telesco, D. C., French, J., and Ftaclas, C. (2009). *Astronomers User Manual.* 27, 34, 35, 37, 38, 41, 45

Chavez-Dagostino, M., Bertone, E., Cruz-Saenz de Miera, F., and Marshall (2016). Early science with the Large Millimetre Telescope: Deep LMT/AzTEC millimetre observations of $\epsilon$ Eridani and its surroundings. *MNRAS*, **462**, 2285–2294. 97

Chini, R., Hoffmeister, V., Kimeswenger, S., Nielbock, M., Nürnberger, D., Schmidtobreick, L., and Sterzik, M. (2004). The formation of a massive protostar through the disk accretion of gas. *Nature*, **429**, 155–157. 10

Dan Li, Charles M. Telesco, F. V. (2010). Characterization of the mid-ir image quality at gemini south. 122

Di Folco, E., Thévenin, F., Kervella, P., Domiciano de Souza, A., Coudé du Foresto, V., Ségransan, D., and Morel, P. (2004). VLTI near-IR interferometric observations of Vega-like stars. Radius and age of $\alpha$ PsA, $\beta$ Leo, $\beta$ Pic, $\epsilon$ Eri and $\tau$ Cet. *A&A*, **426**, 601–617. 96

Dominik, C., Dullemond, C. P., Waters, L. B. F. M., and Walch, S. (2003). Understanding the spectra of isolated Herbig stars in the frame of a passive

disk model. *A&A*, **398**, 607–619. 70, 71, 77, 87, 124, 125, 126

Doucet, C., Lagage, P., and Pantin, E. (2006). High resolution Mid-Infrared Imaging of Dust Disks Structures around Herbig Ae Stars with VISIR. pages 25–30. 15, 48, 92, 93

Duchêne, G. and Kraus, A. (2013). Stellar Multiplicity. *ARA&A*, **51**, 269–310. 12

Dullemond, C. P. (2012). RADMC-3D: A multi-purpose radiative transfer tool. Astrophysics Source Code Library. 67

Dullemond, C. P. and Dominik, C. (2004a). Flaring vs. self-shadowed disks: The SEDs of Herbig Ae/Be stars. *A&A*, **417**, 159–168. 14, 49

Dullemond, C. P. and Dominik, C. (2004b). The effect of dust settling on the appearance of protoplanetary disks. *A&A*, **421**, 1075–1086. 67, 69

Dullemond, C. P., Dominik, C., and Natta, A. (2001). Passive Irradiated Circumstellar Disks with an Inner Hole. *ApJ*, **560**, 957–969. 12

Dutrey, A., Lecavelier Des Etangs, A., and Augereau, J.-C. (2004). *The observation of circumstellar disks: dust and gas components*, pages 81–95. 10, 17

Eales, S. (2009). *Planets and Planetary Systems*. 26

Eiroa, C., Marshall, J. P., Mora, A., Montesinos, B., and Absil (2013). DUst around NEarby Stars. The survey observational results. *A&A*, **555**, A11. 22, 23

Ertel, S., Absil, O., Defrère, D., Le Bouquin, J.-B., Augereau, J.-C., Marion, L., Blind, N., Bonsor, A., Bryden, G., Lebreton, J., and Milli, J. (2014). A near-infrared interferometric survey of debris-disk stars. IV. An unbiased sample of 92 southern stars observed in H band with VLTI/PIONIER. *A&A*, **570**, A128. 24

Espaillat, C., Muzerolle, J., Najita, J., Andrews, S., Zhu, Z., Calvet, N., Kraus, S., Hashimoto, J., Kraus, A., and D'Alessio, P. (2014). An Observational Perspective of Transitional Disks. *Protostars and Planets VI*, pages 497–520. 48

Fedele, D., van den Ancker, M. E., Acke, B., van der Plas, G., van Boekel, R., and Wittkowski, M. (2008). The structure of the protoplanetary disk surrounding three young intermediate mass stars. II. Spatially resolved dust and gas distribution. *A&A*, **491**, 809–820. 47, 50, 51, 66, 68, 71, 72, 73, 122, 123, 124

Forbrich, J., Lada, C. J., Muench, A. A., and Teixeira, P. S. (2008). New M Dwarf Debris Disk Candidates in NGC 2547. *ApJ*, **687**, 1107–1116. 22

Fukagawa, M., Tamura, M., Itoh, Y., Kudo, T., Imaeda, Y., Oasa, Y., Hayashi, S. S., and Hayashi, M. (2006). Near-Infrared Images of Protoplanetary Disk Surrounding HD 142527. *ApJ*, **636**, L153–L156. 47

Fukagawa, M., Tamura, M., Itoh, Y., Oasa, Y., and Kudo (2010). Subaru Near-Infrared Imaging of Herbig Ae Stars. *PASJ*, **62**, 347–. 48, 51

Furlan, E., Hartmann, L., Calvet, N., D'Alessio, P., and Franco-Hernández (2006). A Survey and Analysis of Spitzer Infrared Spectrograph Spectra of T Tauri Stars in Taurus. *ApJS*, **165**, 568–605. 48

Gaia, W. (2016). Gaia-archive. https://gea.esac.esa.int/archive/. 56, 71

García-Lorenzo, B., Eff-Darwich, A., Castro-Almazán, J., Pinilla-Alonso, N., Muñoz-Tuñón, C., and Rodríguez-Espinosa, J. M. (2010). Infrared astronomical characteristics of the Roque de los Muchachos Observatory: precipitable water vapour statistics. *MNRAS*, **405**, 2683–2696. 29

Gautier III, T. N., Rieke, G., Stansberry, J., Bryden, G. C., Stapelfeldt, K. R., Werner, M. W., Beichman, C. A., Chen, C., Su, K., Trilling, D., *et al.* (2007). Far-infrared properties of m dwarfs. *The Astrophysical Journal*, **667**(1), 527. 22

Geers, V. C., van Dishoeck, E. F., Visser, R., Pontoppidan, K. M., Augereau, J.-C., Habart, E., and Lagrange, A. M. (2007). Spatially extended polycyclic aromatic hydrocarbons in circumstellar disks around T Tauri and Herbig Ae stars. *A&A*, **476**, 279–289. 15, 47

Gemini, W. (2016). Gemini observing conditions type @ONLINE. https://www.gemini.edu/sciops/instruments/midir-resources/midir-observing/observing-conditions. 28, 29, 34, 43, 46

Gonzlez-Martn, O., Rodrguez-Espinosa, J. M., and Daz-Santos, T. (2013). Dust in active galactic nuclei. *A&A*, **553**, A35. 66

Grady, C. A., Woodgate, B. E., Bowers, C. W., and Gull, T. R. (2005). Coronagraphic Imaging of Pre-Main-Sequence Stars with the Hubble Space Telescope Space Telescope Imaging Spectrograph. I. The Herbig Ae Stars. *ApJ*, **630**, 958–975. 15

## REFERENCES

Gräfe, C., Wolf, S., Roccatagliata, V., Sauter, J., and Ertel, S. (2011). Mid-infrared observations of the transitional disks around DH Tauri, DM Tauri, and GM Aurigae. *A&A*, **533**, A89. 48

Greaves, J., Holland, W., and Moriarty-Schieven, G. (1998). A dust ring around epsilon eridani: Analog to the young solar system. *Astrophysical Journal*, **506**(2), L133–L137. 97

Greaves, J. S., Sibthorpe, B., Acke, B., Pantin, E. E., and Vandenbussche (2014). Extreme Conditions in a Close Analog to the Young Solar System: Herschel Observations of epsilon Eridani. *ApJ*, **791**, L11. 97

Habart, E., Verstraete, L., Boulanger, F., Pineau des Forêts, G., Le Peintre, F., and Bernard, J. P. (2001). Photoelectric effect on dust grains across the L1721 cloud in the rho Ophiuchi molecular complex. *A&A*, **373**, 702–713. 14

Hatzes, A. P., Cochran, W. D., McArthur, B., and Baliunas, S. L. (2000). Evidence for a Long-Period Planet Orbiting $\epsilon$ Eridani. *ApJ*, **544**, L145–L148. 2, 97, 129

Hayashi, C., Nakazawa, K., and Nakagawa, Y. (1985). Formation of the solar system. In D. C. Black and M. S. Matthews, editors, *Protostars and Planets II*, pages 1100–1153. 17

Heng, K. and Malik, M. (2013). Debris discs around m stars: non-existence versus non-detection. *Monthly Notices of the Royal Astronomical Society*, **432**(3), 2562–2572. 22

Honda, M., Inoue, A. K., Okamoto, Y. K., Kataza, H., Fukagawa, M., Yamashita, T., and Fujiyoshi, T. (2010). Pre-transitional Disk Nature of the AB Aur Disk. *ApJ*, **718**, L199–L203. 47

Honda, M., Maaskant, K., Okamoto, Y. K., Kataza, H., Fukagawa, M., Waters, L. B. F. M., and Dominik, C. (2012). Mid-infrared Imaging of the Transitional Disk of HD 169142: Measuring the Size of the Gap. *ApJ*, **752**, 143. 47, 122, 124

Honda, M., Maaskant, K., Okamoto, Y. K., Kataza, H., Yamashita, T., Miyata, T., Sako, S., and Fujiyoshi, T. (2015). High-resolution 25 M Imaging of the Disks around Herbig Ae/Be Stars. *ApJ*, **804**, 143. 50, 51

Iglesias, C. A. A. (2014). Canaricam-at-the-gtc. http://riastronomia.es/Descargas/ArchivoHemeroteca/TallersobrecienciaenelinfrarrojomedioyCanariCam_CarlosAlvarez_RIA2013. 28

Isella, A., Carpenter, J. M., and Sargent, A. I. (2009). Structure and Evolution of Pre-main-sequence Circumstellar Disks. *ApJ*, **701**, 260–282. 48

Jeffrey A. Julian, J. P. F. (2014). Canaricam-desgin. http://www.astro.ufl. edu/CanariCam/Mechanical/ CanariCam_CDR_Mechanical.pdf. 37

Juhász, A., Bouwman, J., Henning, T., Acke, B., van den Ancker, M. E., Meeus, G., Dominik, C., Min, M., Tielens, A. G. G. M., and Waters, L. B. F. M. (2010). Dust Evolution in Protoplanetary Disks Around Herbig Ae/Be Starsthe Spitzer View. *ApJ*, **721**, 431–455. 70, 75, 91, 94, 123

Kraus, S., Hofmann, K.-H., Menten, K. M., Schertl, D., Weigelt, G., Wyrowski, F., Meilland, A., Perraut, K., Petrov, R., Robbe-Dubois, S., Schilke, P., and Testi, L. (2010). A hot compact dust disk around a massive young stellar object. *Nature*, **466**, 339–342. 10

Laboratory, T. A. . A. (2016-8-24). http://www.astrochemistry.org. http://www.astrochemistry. org/pahdb/theoretical/1.32/ help/pressreleases/iris. 15

Lada, C. J. (1987). Star formation - From OB associations to protostars. In M. Peimbert and J. Jugaku, editors, *Star Forming Regions*, volume 115 of *IAU Symposium*, pages 1–17. 7, 8

Lagage, P.-O., Doucet, C., Pantin, E., Habart, E., Duchêne, G., Ménard, F., Pinte, C., Charnoz, S., and Pel, J.-W. (2006). Anatomy of a Flaring Proto-Planetary Disk Around a Young Intermediate-Mass Star. *Science*, **314**, 621–623. 15, 48, 93, 123

Lagrange, A.-M., Backman, D. E., and Artymowicz, P. (2000). Planetary Material around Main-Sequence Stars. *Protostars and Planets IV*, page 639. 17

Lagrange, A.-M., Gratadour, D., Chauvin, G., Fusco, T., Ehrenreich, D., Mouillet, D., and Rousset (2009). A probable giant planet imaged in the $\beta$ Pictoris disk. VLT/NaCo deep L'-band imaging. *A&A*, **493**, L21–L25. 96

LeBlanc, F. (2011). *An Introduction to Stellar Astrophysics*. Wiley. 47

Leinert, C., van Boekel, R., Waters, L. B. F. M., Chesneau, O., Malbet, F., Köhler, R., and Jaffe, W. (2004). Mid-infrared sizes of circumstellar disks around Herbig Ae/Be stars measured with MIDI on the VLTI. *A&A*, **423**, 537–548. 49, 51

# REFERENCES

Lestrade, J.-F., Wyatt, M. C., Bertoldi, F., Dent, W. R. F., and Menten, K. M. (2006). Search for cold debris disks around M-dwarfs. *A&A*, **460**, 733–741. 22

Li, D. (2014). iDealCam: Interactive Data Reduction and Analysis for CanariCam. Astrophysics Source Code Library. 45, 52

Li, D., Telesco, C. M., and Varosi, F. (2010). Characterization of the mid-IR image quality at Gemini South. In *Observatory Operations: Strategies, Processes, and Systems III*, volume 7737 of *Proc. SPIE*, page 77372F. 99, 108

Li, D., López Rodríguez, E., Pantin, E., Varosi, F., Telesco, C. M., and Packham, C. (2013). IdealCam: An IDL GUI Package for CanariCam Data Reduction and Analysis. 45, 64, 118

Liu, M. C., Matthews, B. C., Williams, J. P., and Kalas, P. G. (2004). A Submillimeter Search of Nearby Young Stars for Cold Dust: Discovery of Debris Disks around Two Low-Mass Stars. *ApJ*, **608**, 526–532. 22

Liu, W. M., Hinz, P. M., Meyer, M. R., and Mamajek, E. E. (2007). Observations of Herbig Ae Disks with Nulling Interferometry. *ApJ*, **658**, 1164–1172. 51, 124

Lord, S. D. (1992). A new software tool for computing Earth's atmospheric transmission of near- and far-infrared radiation. Technical report. 27, 29

Low, F. J., Smith, P. S., Werner, M., Chen, C., Krause, V., Jura, M., and Hines, D. C. (2005). Exploring terrestrial planet formation in the tw hydrae association. *The Astrophysical Journal*, **631**(2), 1170. 22

Maaskant, K. M., Honda, M., Waters, L. B. F. M., Tielens, A. G. G. M., and Dominik, C. (2013). Identifying gaps in flaring Herbig Ae/Be disks using spatially resolved mid-infrared imaging. Are all group I disks transitional? *A&A*, **555**, A64. 14, 15, 93

Maaskant, K. M., Min, M., Waters, L. B. F. M., and Tielens, A. G. G. M. (2014). Polycyclic aromatic hydrocarbon ionization as a tracer of gas flows through protoplanetary disk gaps. *A&A*, **563**, A78. 16, 48, 93, 94, 123, 126

Madhusudhan, N., Crouzet, N., McCullough, P. R., Deming, D., and Hedges, C. (2014). $H_2O$ Abundances in the Atmospheres of Three Hot Jupiters. *ApJ*, **791**, L9. 1

Mariñas, N., Telesco, C. M., Fisher,

R. S., and Packham, C. (2011). High-resolution Mid-infrared Imaging of the Circumstellar Disks of Herbig Ae/Be Stars. *ApJ*, **737**, 57. 48, 50, 51, 56, 122

Marois, C., Macintosh, B., Barman, T., Zuckerman, B., Song, I., Patience, J., Lafrenière, D., and Doyon, R. (2008). Direct Imaging of Multiple Planets Orbiting the Star HR 8799. *Science*, **322**, 1348. 96

Mason, J. (2008). *Exoplanets: detection, formation, properties, habitability*. Springer Science & Business Media. 12

Mathis, J. S. (1990). Interstellar dust and extinction. *ARA&A*, **28**, 37–70. 71

Mathis, J. S., Rumpl, W., and Nordsieck, K. H. (1977). The size distribution of interstellar grains. *ApJ*, **217**, 425–433. 69

Matter, A., Labadie, L., Augereau, J. C., and Kluska, J. (2016). Inner disk clearing around the Herbig Ae star HD 139614: Evidence for a planet-induced gap? *A&A*, **586**, A11. 47, 67, 70, 77

Matthews, B. C., Kalas, P. G., and Wyatt, M. C. (2007). Mass and temperature of the twa 7 debris disk. *The Astrophysical Journal*, **663**(2), 1103. 22

Matthews, B. C., Krivov, A. V., Wyatt, M. C., Bryden, G., and Eiroa, C. (2014). Observations, Modeling, and Theory of Debris Disks. *Protostars and Planets VI*, pages 521–544. 17, 22, 23

Mayor, M. and Queloz, D. (1995). A Jupiter-mass companion to a solar-type star. *Nature*, **378**, 355–359. 1

McCabe, C., Ghez, A. M., Prato, L., Duchêne, G., Fisher, R. S., and Telesco, C. (2006). Investigating Disk Evolution: A High Spatial Resolution Mid-Infrared Survey of T Tauri Stars. *ApJ*, **636**, 932–951. 12

Meeus, G., Waters, L. B. F. M., Bouwman, J., van den Ancker, M. E., Waelkens, C., and Malfait, K. (2001). ISO spectroscopy of circumstellar dust in 14 Herbig Ae/Be systems: Towards an understanding of dust processing. *A&A*, **365**, 476–490. 13, 49, 77, 94

Meeus, G., Bouwman, J., Dominik, C., Waters, L. B. F. M., and de Koter, A. (2002). The absence of the 10 mu m silicate feature in the isolated Herbig Ae star HD 100453. *A&A*, **392**, 1039–1046. 70

Mennesson, B., Millan-Gabet, R., and Serabyn, E. (2014). Constraining the Exozodiacal Luminosity Function

of Main-sequence Stars: Complete Results from the Keck Nuller Mid-infrared Surveys. *ApJ*, **797**, 119. 23

Menu, J., van Boekel, R., Henning, T., Leinert, C., Waelkens, C., and Waters, L. (2015). The structure of disks around intermediate-mass young stars from mid-infrared interferometry-evidence for a population of group ii disks with gaps. *Astronomy & Astrophysics*, **581**, A107. 14

Meyer, M. R., Carpenter, J. M., Mamajek, E. E., Hillenbrand, L. A., Hollenbach, D., and Moro-Martin, A. (2008). Evolution of mid-infrared excess around sun-like stars: Constraints on models of terrestrial planet formation. *The Astrophysical Journal Letters*, **673**(2), L181. 22

Moerchen, M. M., Telesco, C. M., Packham, C., and Kehoe, T. J. J. (2007). Mid-Infrared Resolution of a 3 AU Radius Debris Disk around $\zeta$ Leporis. *ApJ*, **655**, L109–L112. 55, 96

Moerchen, M. M., Telesco, C. M., and Packham, C. (2010). High Spatial Resolution Imaging of Thermal Emission from Debris Disks. *ApJ*, **723**, 1418–1435. 56, 96, 110, 111, 122, 128

Monnier, J. D., Berger, J.-P., Millan-Gabet, R., Traub, W. A., Schloerb, F. P., Pedretti, E., and Benisty, M. (2006). Few Skewed Disks Found in First Closure-Phase Survey of Herbig Ae/Be Stars. *ApJ*, **647**, 444–463. 50

Moran, S. M., Kuchner, M. J., and Holman, M. J. (2004). The Dynamical Influence of a Planet at Semimajor Axis 3.4 AU on the Dust around $\epsilon$ Eridani. *ApJ*, **612**, 1163–1170. 97

Natta, A., Prusti, T., Neri, R., Wooden, D., Grinin, V. P., and Mannings, V. (2001). A reconsideration of disk properties in Herbig Ae stars. *A&A*, **371**, 186–197. 12

Nilsson, R., Liseau, R., Brandeker, A., Olofsson, G., and Pilbratt (2010). Kuiper belts around nearby stars. *A&A*, **518**, A40. 23

Packham, C., Telesco, C. M., Hough, J. H., and Ftaclas, C. (2005). CanariCam: The Multi-Mode Mid-IR Instrument for the GTC. In A. M. Hidalgo-Gámez, J. J. González, J. M. Rodríguez Espinosa, and S. Torres-Peimbert, editors, *Revista Mexicana de Astronomia y Astrofisica Conference Series*, volume 24 of *Revista Mexicana de Astronomia y Astrofisica Conference Series*, pages 7–12. 36, 42

Peeters, E., Hony, S., Van Kerckhoven, C., Tielens, A. G. G. M., Allamandola, L. J., Hudgins, D. M., and

Bauschlicher, C. W. (2002). The rich 6 to 9 vec mu m spectrum of interstellar PAHs. *A&A*, **390**, 1089–1113. 93

Petrou, M. and Petrou, C. (2010). *Image processing: the fundamentals*. John Wiley & Sons. 32

Piétu, V., Dutrey, A., and Kahane, C. (2003). A Keplerian disk around the Herbig Ae star HD 34282. *A&A*, **398**, 565–569. 12

Pilbratt, G. L., Riedinger, J. R., Passvogel, T., and Crone (2010). Herschel Space Observatory. An ESA facility for far-infrared and submillimetre astronomy. *A&A*, **518**, L1. 96

Pinte, C., Harries, T. J., Min, M., Watson, A. M., and Dullemond, C. P. (2009). Benchmark problems for continuum radiative transfer. High optical depths, anisotropic scattering, and polarisation. *A&A*, **498**, 967–980. 67

Plavchan, P., Jura, M., and Lipscy, S. J. (2005). Where Are the M Dwarf Disks Older Than 10 Million Years? *ApJ*, **631**, 1161–1169. 22

Pollack, J. B., Hubickyj, O., Bodenheimer, P., Lissauer, J. J., Podolak, M., and Greenzweig, Y. (1996). Formation of the Giant Planets by Concurrent Accretion of Solids and Gas. *Icarus*, **124**, 62–85. 17, 25

Rauer, H. (2013). The PLATO 2.0 mission. *European Planetary Science Congress 2013, held 8-13 September in London, UK.*, **8**, EPSC2013–707. 1

Raymond, S. N., Armitage, P. J., and Moro-Martín, A. (2012). Debris disks as signposts of terrestrial planet formation. II. Dependence of exoplanet architectures on giant planet and disk properties. *A&A*, **541**, A11. 95

Reidemeister, M., Krivov, A. V., Stark, C. C., Augereau, J.-C., Löhne, T., and Müller, S. (2011). Warm dust around $\epsilon$ Eridani. In A. Sozzetti, M. G. Lattanzi, and A. P. Boss, editors, *The Astrophysics of Planetary Systems: Formation, Structure, and Dynamical Evolution*, volume 276 of *IAU Symposium*, pages 455–456. 97, 129

Rhee, J. H., Song, I., Zuckerman, B., and McElwain, M. (2007). Characterization of dusty debris disks: The iras and hipparcos catalogs. *The Astrophysical Journal*, **660**(2), 1556. 21, 22

Riaz, B., Lodieu, N., and Gizis, J. E. (2009). Brown Dwarf Disks at Ages of 5-10 Myr. *ApJ*, **705**, 1173–1182. 10

Rieke, G. H., Su, K. Y. L., Stansberry, J. A., and Trilling (2005). Decay of Planetary Debris Disks. *ApJ*, **620**, 1010–1026. 17, 21

# REFERENCES

Robson, I., Holland, W. S., and Friberg, P. (2017). Celebrating 30 years of science from the james clerk maxwell telescope. *Royal Society Open Science*, **4**(9). 20

Saha, S. K. (2010). *Aperture synthesis: methods and applications to optical astronomy*. Springer Science & Business Media. 31, 34

Schroeder, D. (2000). *Astronomical Optics*. Electronics & Electrical. Academic Press. 31, 32

Seeds, M. and Backman, D. (2011). *Horizons: Exploring the Universe*. Cengage Learning. 3

Seok, J. Y. and Li, A. (2017). Polycyclic Aromatic Hydrocarbons in Protoplanetary Disks around Herbig Ae/Be and T Tauri Stars. *ApJ*, **835**, 291. 94

Smith, B. A. and Terrile, R. J. (1984). A circumstellar disk around Beta Pictoris. *Science*, **226**, 1421–1424. 19

Stahler, S. W. and Palla, F. (2008). *The formation of stars*. John Wiley & Sons. 4, 8, 47

Su, K. Y. L., Rieke, G. H., Misselt, K. A., and Stansberry, J. A. (2005). The Vega Debris Disk: A Surprise from Spitzer. *ApJ*, **628**, 487–500. 21

Su, K. Y. L., Rieke, G. H., Stansberry, J. A., and Bryden, G. (2006). Debris Disk Evolution around A Stars. *ApJ*, **653**, 675–689. 23

Testi, L., Birnstiel, T., Ricci, L., and Andrews (2014). Dust Evolution in Protoplanetary Disks. *Protostars and Planets VI*, pages 339–361. 11

The, P. S., de Winter, D., and Perez, M. R. (1994). A new catalogue of members and candidate members of the Herbig Ae/Be (HAEBE) stellar group. *A&AS*, **104**, 315–339. 49

Thebault, P. and Haghighipour, N. (2014). Planet formation in Binaries. *ArXiv e-prints*. 12

Thureau, N. D., Greaves, J. S., Matthews, B. C., Kennedy, G., Phillips, N., Booth, M., and Duchêne, G. (2014). An unbiased study of debris discs around A-type stars with Herschel. *MNRAS*, **445**, 2558–2573. 23

Visser, R., Geers, V. C., Dullemond, C. P., Augereau, J.-C., Pontoppidan, K. M., and van Dishoeck, E. F. (2007). PAH chemistry and IR emission from circumstellar disks. *A&A*, **466**, 229–241. 14

Waelkens, C., Bogaert, E., and Waters, L. B. F. M. (1994). The spectral evolution of Herbig Ae/Be stars. In P. S.

The, M. R. Perez, and E. P. J. van den Heuvel, editors, *The Nature and Evolutionary Status of Herbig Ae/Be Stars*, volume 62 of *Astronomical Society of the Pacific Conference Series*, page 405. 13

Ward-Thompson, D. and Whitworth, A. P. (2011). *An introduction to star formation*. Cambridge University Press. 7

Weingartner, J. C. and Draine, B. T. (2001). Dust Grain-Size Distributions and Extinction in the Milky Way, Large Magellanic Cloud, and Small Magellanic Cloud. *ApJ*, **548**, 296–309. 14

Williams, J. P. and Cieza, L. A. (2011). Protoplanetary Disks and Their Evolution. *ARA&A*, **49**, 67–117. 9, 12, 70, 83

Wright, J. T. and Gaudi, B. S. (2013). *Exoplanet Detection Methods*, page 489. 1

Wyatt, M. C. (2008). Evolution of Debris Disks. *ARA&A*, **46**, 339–383. 20, 21

Wyatt, M. C., Greaves, J. S., Dent, W. R. F., and Coulson, I. M. (2005). Submillimeter Images of a Dusty Kuiper Belt around $\eta$ Corvi. *ApJ*, **620**, 492–500. 23

Wyatt, M. C., Clarke, C. J., and Greaves, J. S. (2007). Origin of the metallicity dependence of exoplanet host stars in the protoplanetary disc mass distribution. *MNRAS*, **380**, 1737–1743. 95

Wyatt, M. C., Kennedy, G., Sibthorpe, B., Moro-Martín, A., Lestrade, J.-F., Ivison, R. J., Matthews, B., Udry, S., and Greaves (2012). Herschel imaging of 61 Vir: implications for the prevalence of debris in low-mass planetary systems. *MNRAS*, **424**, 1206–1223. 96

Youdin, A. N. and Kenyon, S. J. (2013). *From Disks to Planets*, page 1. 25, 26

Zapatero Osorio, M. R., Caballero, J. A., Béjar, V. J. S., Rebolo, R., Barrado Y Navascués, D., Bihain, G., Eislöffel, J., Martín, E. L., Bailer-Jones, C. A. L., Mundt, R., Forveille, T., and Bouy, H. (2007). Discs of planetary-mass objects in $\sigma$ Orionis. *A&A*, **472**, L9–L12. 10

# Acknowledgements

.

# Erklärung zur Dissertation

Ich versichere, dass die von mir vorgelegte Dissertation selbstständig angefertigt, die benutzten Quellen und Hilfsmittel vollständig angegeben und Stellen der Arbeit-einschließlich Tabellen, Karten und Abbildungen -, die anderen Werken im Wortlaut oder dem Sinn nach entnommen sind, in jedem Einzelfall als Entlehung kenntlich gemacht habe; dass diese Dissertation noch keiner anderen Fakultät oder Universität zur Prüfung vorgelegen hat; dass sie - abgesehen von unten angegebenen Teilpublikationen - noch nicht veröffentlicht worden ist sowie, dass ich eine solche Veröffentlichung vor Abschluss des Promotionsverfahrens nicht vornehmen werde.
Die Bestimmungen dieser Promotionsordnung sind mir bekannt. Die von mir vorgelegte Dissertation ist von **Prof. Dr. Lucas Labadie** betreut worden.

Anas Salman Taha

I. Physikalisches Institut

Universität zu Köln

Zülpicher Straße 77

50937 Köln

+49-017672484190

maotahni@ph1.uni-koeln.de

# Teilpublikationen

# Lebenslauf

## Ausbildung

| | |
|---|---|
| Name, Vorname: | AL-Maothani, Anas Salman Taha |
| Anschrift: | Luxemburger-Str. 333 |
| | 50939 Cologne. Germany |
| Telefon: | +49-017672484190 |
| Email: | maotahni@ph1.uni-koeln.de |
| Geburtsort: | Irakische |
| Geburtsdatum: | 21 Dez. 1977 |

## Ausbildung

Seit Nov 2013　Promotionstudent
I Physikalisches Institut der Universitaet zu Koeln
Koeln, Deutschland

1999-2003　Magisters Abschluss in Astronomie (Celestial Mechanic) mit 78,57%
Universität Bagdad, Akademie für Naturwisschenschaften,
Abteilung für Astronomie
Bagdad, Irak

1995-1999　Abschluss in Physik mit 67,38%
Universität AL-Mustansiriya, Akademie für Naturwisschenschaften,
Abteilung für physik
Bagdad, Irak

## Berufliche Laufbahn

2002　2013　Dozententätigkeit in der Universität Bagdad, Akademie fur Naturwisschenschaften, Abteilung fur Astronomie, Bagdad, Irak

**Köln, 2017**